Time-Resolved Studies and Nanostructure Formation in Sb_2Te_3 Films Using Femtosecond Lasers

by

Yuwei Li

A dissertation submitted in partial fulfillment
of the requirements for the degree of
Doctor of Philosophy
(Physics)
in the University of Michigan
2014

Doctoral Committee:

Professor Roy Clarke, Chair
Professor Rachel S. Goldman
Professor Çagliyan Kurdak
Associate Professor Kevin P. Pipe
Professor Ctirad Uher

To my family:

My parents, Xiaoxia and Zhongduo

My husband, Andy

ACKNOWLEDGEMENTS

I am very grateful to my advisor, Prof. Roy Clarke, for his guidance and encouragement in the past five years. I have grown tremendously as a scientist thanks to his countless pieces of invaluable advice on research, writing, and teaching. He really sets an example to me for what an excellent physicist and mentor should be like.

I am thankful to Prof. Uher for providing the beautiful Sb_2Te_3 thin film samples that have made my dissertation work possible. Our discussions and collaborations over the years have been highly enjoyable. Prof. Kurdak has offered a lot of support to me both in science and in life, ever since my early years in Michigan. I am truly grateful for his encouragement to me and his sincere devotion to the success of graduate students in general. Prof. Pipe graciously provided his lasers and lab facilities to me, which has led to some of the most interesting nanotrack results in this work. Also, Prof. Goldman and I have been carrying out some exciting collaborations.

I would like to thank Dr. Vladimir Stoica for introducing the laser techniques to me and having fruitful and intriguing discussions on my research projects. He was always ready to lend a hand to me and other students with his experimental expertise and physical insights. Lynn Endicott, Dr. Wei Liu and Dr. Guoyu Wang grew the high-quality thin film samples for my experiments. Dr. Kai Sun in EMAL assisted me with the operation of TEM and STEM and Dr. Haiping Sun in EMAL has been an enormous help to me with the general use of the microscopes during the past few years. Lei Shao, Dr. Huarui Sun and Dr. Gunho Kim from Prof. Pipe's group as well as Dr. Yen-Hsiang Lin and Jenna Walrath from Prof. Goldman's group have been working with me on collaborative projects, which have been pleasant and memorable experiences. Furthermore, my sincere gratitude goes to the financial and community support from the Center for Solar and Thermal Energy Conversion, an Energy Frontier Research Center funded by the U.S. Department of Energy, Office of Science.

I wish to express my appreciation to all the other friends who have accompanied me during my graduate study and shared the joy and frustration as fellow students and colleagues: Yongsoo Yang, Abe Oraiqat, Naji Husseini, and Reneé Harton from the Clarke group; Jessica Ames, Andrew Schwarzkopf, Lynn Endicott, and Navid Dianati, with whom I have been good friends since my first year in Michigan; Dennis Allen and Ramon Torres-Isea, who have brought me many hilarious moments during our regular coffee hour in the otherwise sleepy afternoons; Christina Zigulis from the Physics Department and Cynthia McNabb from the Applied Physics Program, who have provided substantial support and assistance as administration staff members. Additionally, there are many other people with whom the interactions have been brief but delightful.

Finally, I am extremely fortunate to have Andy as my life companion. His love and wit have turned my years in graduate school into a joyful journey, and his support and encouragement have helped me get through some of the most stressful moments in my research. I am also indebted to my parents for their continuous and unconditional love and support; I would have never achieved this much without them.

TABLE OF CONTENTS

CHAPTERS

LIST OF FIGURES

Figure

LIST OF TABLES

Table

ABSTRACT

Antimony telluride (Sb_2Te_3) is an important material with a wide range of applications in thermoelectrics, data storage devices and topological insulator research. Our work on femtosecond laser studies of Sb_2Te_3 films has significance for insights into femtosecond laser interaction with Sb_2Te_3 above the damage threshold, as well as providing a new pathway for novel fabrication of highly-ordered nanostructured Sb_2Te_3. These new developments are made possible by careful control of the laser scanning conditions, opening the way to future nanoscale studies and materials applications.

The pump-probe scheme for the time-resolved studies employed a novel asynchronous optical sampling (ASOPS) technique, which has distinctive advantages over the traditional mechanical-delay scheme including superior stability of beam alignment during scans, faster data acquisition rates, and the ability to monitor a much wider range of dynamics up to ten nanoseconds. With ASOPS, it is shown that a sequence of connected processes can be studied in Sb_2Te_3 films, from coherent optical phonons and acoustic echoes at picosecond timescale, through thermal transport at nanosecond timescale. In particular, the coherent phonons were used, for the first time, to monitor the element segregation in Sb_2Te_3 films under high-fluence pump laser irradiation conditions. These results are important for the ultrafast spectroscopy research community: they highlight the need for careful interpretation of coherent phonon spectra in tellurides, which are susceptible to fs laser damage.

Femtosecond laser irradiation of Sb_2Te_3 above ~6 mJ/cm^2 was also found to produce highly-ordered nanotracks with a periodicity an order of magnitude below the laser wavelength. A variety of characterization techniques identified these nanotracks as single crystalline Sb_2Te_3 nanowires separated by polycrystalline phases including a large amount of the insulating Sb_2O_3. Laser irradiation in different gas environments revealed the sensitivity of the Sb_2Te_3 surface morphology to the surrounding gas species, especially O_2, highlighting the critical role of the

ambient environment interactions with Sb_2Te_3 for nanostructure formation in the thin films. These results provide valuable experimental input for the future analysis of the generation mechanism of these nanostructures. Additionally, the results open up new opportunities for fabrication of in-plane Sb_2Te_3 nanowires for planar applications.

Chapter 1

Introduction

Since their first successful operation in 1960, lasers have seen an extensive range of applications in almost every part of modern society, due to their superior spatial and temporal coherence compared to other light sources. While the original continuous wave (cw) operation continued to advance with a larger variety of active media and a wider range of applications, the development of the pulsed operation of lasers in the 1980s has opened up completely new and rich research regimes that have proved to be extremely useful. Capable of being focused to a spot size of microns with all the energy of a pulse compressed to as low as a few femtoseconds, pulsed lasers have shown their ability to detect ultrafast dynamics in materials with time resolutions comparable to their pulse widths and to efficiently modify a great selection of materials with extreme precision. These new capabilities of pulses lasers, otherwise difficult to achieve with traditional detectors, or tools for material removal, have placed pulsed lasers in a unique and critical position in both research and industrial applications.

Ultrafast pulsed laser spectroscopy is one of the most popular research applications. Here, pump-probe measurements utilizing ultrafast laser beams have enabled temporal resolution limited in theory only by the laser pulse duration. In this technique, a strong pump laser beam strikes the sample and initiates an ultrafast process. This process may start with the electron redistribution among energy levels due to the absorption of the photon energy, and then proceed through a variety of dynamic processes following the relaxation of the excited electrons, such as the excitations of optical and acoustic phonons and a lattice temperature rise. These dynamics change the optical properties of the materials such as reflectivity or transmittance, which are monitored by a weak probe laser beam. An ultrafast probe beam is usually used for capturing dynamics on the time scale of femtoseconds (fs) or picoseconds (ps). In this configuration, the arrival of the probe at the sample is delayed with respect to the pump excitation. By sending out a train of pump and probe pulses and controlling the delay of the probe pulse relative to each pump pulse, sample property changes as a function of time, and thus the ultrafast dynamics, can be obtained. Characteristics of these dynamics contain vital information about the sample. For example, coherent phonon frequency connects to the molecular composition, while its relaxation time can be related to the crystalline quality of the sample. The laser pump-probe technique used in this dissertation work mainly concerns the coherent phonon excitation for phase identification, acoustic strain propagation for film thickness estimation, and heat transport for thermal diffusivity measurements. Relevant theories and experimental techniques will be discussed in detail in Chapter 2.

While material interactions with weak pulsed lasers have provided a nondestructive way to gain insights into materials properties, interactions with a strong laser above a characteristic threshold may introduce temporary or permanent modifications in the materials. For cw lasers, the materials are altered mostly through the melting process from the temperature increase. Pulsed laser interactions, on the other hand, include a richer variety of processes due to the high concentration of photon energy deposited within an extremely short time. For semiconductors, a sudden excitation of a large concentration of electrons into the conduction band may drastically weaken the bonds in the lattice, and cause the so-called non-thermal melting, where the lattice loses its ordering on a time scale of fs, considerably before the lattice temperature is significantly raised to near the melting threshold [1.1, 1.2]. One manifestation of this process is phonon softening in the laser pump-probe experiments, where the coherent phonon frequency down-shifts as the pump laser power is increased and the bonds in the molecules weaken as a result [1.3]. Similar bond-softening following high-intensity laser excitations has also been detected with time-resolved X-ray diffraction studies [1.4].

In addition to material changes on an ultrafast time scale that may or may not be reversible, lasers can also cause permanent modifications on longer time scales. A temperature rise from prolonged laser irradiation can lead to phase segregation, evaporation or sublimation of the segregated elements. This is especially evident in the technologically important chalcogenides, whose relatively low thermal conductivity speeds up the temperature increase and subsequent structural changes. For example, tellurides have been known to exhibit segregation in laser Raman studies, where additional Raman peaks corresponding to tellurium appear after irradiation by the cw laser [1.5, 1.6]. While such an effect is less of an issue for pulsed lasers, those with high repetition rates can be of great concern for materials with low thermal conductivities. In this case, the heat generated from the previous pulse is not able to dissipate completely in the material before the next pulse arrives. As a result, the residual heat builds up quickly, and the material may lose its structural integrity through thermal processes or a combination of thermal and ultrafast processes. However, while the ultrafast spectroscopy community has shown an increasing interest in the chalcogenide compounds [1.7, 1.8], few have investigated the possible modification effects from pulsed lasers with high repetition rates. Chapter 3 of this dissertation aimed to address the necessity of careful interpretation of data from the pump-probe experiments of chalcogenide compounds, by demonstrating tellurium segregation in Sb_2Te_3 as an example.

Although optical measurements involving lasers may bring about damage concerns, the ability of lasers to modify or even remove materials have been utilized in areas such as cutting, surface patterning [1.9], and pulsed laser deposition [1.10]. In particular, lasers have proved handy in micro-processing materials that are challenging for mechanical cutting or chemical etching [1.11, 1.12]. One interesting phenomenon observed in laser processing of solid materials is the appearance of periodic ripple-like structures near the laser damage threshold of the material. First demonstrated in 1965 on a series of semiconductors with a ruby laser [1.13], these ripples have fascinated researchers in terms of their formation mechanisms, the resulting material modifications on the macro and micro-scales, and potential applications. Among the ripples induced by a large variety of lasers, the ones induced by ultrafast lasers have been particularly interesting [1.14-1.17]. With their periodicity many times below the irradiation laser wavelength, these deep sub-wavelength ripples are formed via a complex mechanism still not well understood. It may involve an interplay of nonlinear processes depending on the specific material irradiated [1.14-1.17]. Chapter 4 of this dissertation is concerned with the formation of these deep sub-wavelength ripples on Sb_2Te_3 thin films after irradiation by femtosecond lasers. Our work in this chapter shows the ability of the femtosecond laser to not only tune the surface morphologies of nanostructures on Sb_2Te_3, but also to create modulations of crystal structures and chemical compositions on the nanoscale. The investigation of ultrafast laser-induced nanostructures, through a variety of microscopic techniques, provides insights into the possible processes involved in their formation in Sb_2Te_3, and offers avenues for possible applications of these nanostructures in a variety of technology fields.

This dissertation focuses on one particular material: Sb_2Te_3. With unique applications in the fields of thermoelectrics [1.18, 1.19], phase-change materials [1.20, 1.21], and more recently, topological insulators [1.22], Sb_2Te_3 has been attracting considerable attention from researchers for several decades. Sb_2Te_3 has a rhombohedral crystal structure, with two Sb ions and three Te ions per unit cell. However, like other V-VI compounds such as Bi_2Te_3 and Bi_2Se_3, Sb_2Te_3 can be viewed in a more symmetric representation in terms of a hexagonal supercell (Figure 1-1). In this representation, the c-axis of the supercell is along the same direction as the principal symmetry axis of the rhombohedral cell. The supercell consists of three quintuple layers along the c-axis separated by the weak van der Waals bonds. Therefore, like any other layered materials with van der Waals gaps, it is very easy to peel off layers from Sb_2Te_3. Each quintuple layer consists of five layers of alternating Sb and Te hexagonal planes. Within the quintuple layers, the bonds between neighboring layer is strongly covalent. Sb_2Te_3 is usually populated with intrinsic defects, which lowers its Fermi level well into the valence band and thus makes an undoped Sb_2Te_3 naturally p-type [1.18]. The Sb_2Te_3 thin film samples in this dissertation were grown with their surface in the c-plane by the MBE method in Prof. Uher's lab, aligned with the [0001] direction of the Al_2O_3 substrate.

Single crystal Sb_2Te_3 is regarded as one of the best bulk thermoelectric materials for room-temperature applications. With a reasonable Seebeck coefficient around 90 μV/K and a low thermal conductivity of 1.6 W/mK along the c-axis, the thermoelectric conversion efficiency of Sb_2Te_3 is among the highest in the bulk single crystal materials at room temperature [1.18]. If Sb_2Te_3 is alloyed with Bi_2Te_3 to form the BiSbTe alloy, both n-type and p-type thermoelectric materials can be produced with twice the figure of merit as that of Sb_2Te_3 alone. To date, BiSbTe alloy is still being widely used in room-temperature thermoelectric devices, such as small-scale power generators and coolers.

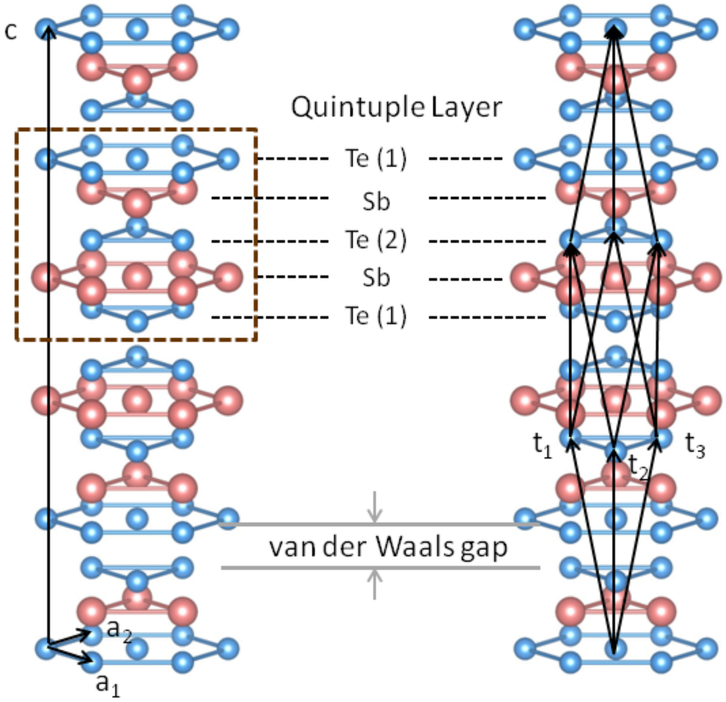

Figure 1-1. The crystal structure of Sb_2Te_3. The basis vectors for the hexagonal representation (a_1, a_2, c), and for the rhombohedral representation (t_1, t_2, t_3), are displayed in the left and right illustrations, respectively. c = 30.4 Å, $a_1 = a_2 = 4.25$ Å, and $t_1 = t_2 = t_3 = 10.4$ Å. The brown dashed box highlights one quintuple layer.

Additionally, Sb_2Te_3 displays reversible phase change properties upon heating or laser irradiation [1.23]. In this process, the material becomes amorphous when heated above its melting point and then cooled rapidly, and re-crystallizes as the temperature is kept above its crystallization temperature and below its melting temperature for a short time. Between these two states, both the laser reflectivity and electric conductivity of the material differ greatly. This unique property has enabled applications such as rewritable CDs and DVDs as stable memory storage devices. Similar to its thermoelectric application, Sb_2Te_3 can be combined with GeTe to form the pseudo-binary material $Ge_2Sb_2Te_5$ with optimal phase change properties and fast time response [1.21].

More recently, Sb_2Te_3 has been shown to be a strong candidate for topological insulators, which exhibit insulator-like properties within the bulk, and metal-like properties on the surface [1.22]. This difference in the electronic properties of the surface and the bulk raises intriguing prospects for fundamental and applied studies in Sb_2Te_3 and other potential candidates for topological insulator systems.

The main goal of my dissertation is to obtain a better understanding of the laser interaction with the technologically and scientifically important material Sb_2Te_3. This is achieved in two series of experiments: 1. Detection of the phase decomposition and segregation induced by the femtosecond lasers; 2. Investigation of the highly-ordered nanostructures formed by the irradiation of the femtosecond lasers. My dissertation is arranged as follows:

Chapter 2 introduces the laser pump-probe techniques employed in the experimental work. It starts with a description of the Asynchronous Optical Sampling (ASOPS) laser system used in the pump-probe experiments, and moves on to the theories and experimental detection techniques of coherent optical phonons, acoustic strains, and thermal transport.

Chapter 3 discusses the detection of phase modifications to the Sb_2Te_3 thin films induced by the pump laser in the pump-probe experiments. Complementary measurements from coherent optical phonon spectroscopy with femtosecond lasers and micro-Raman spectroscopy with a cw laser were performed to confirm the changes to the original Sb_2Te_3 phase.

Chapter 4 presents the femtosecond laser's ability to induce well-controlled periodic nanostructure on Sb_2Te_3 thin films. Multiple characterization techniques were employed to understand the dependence of the nanostructure morphologies on the irradiation parameters and to reveal the modification to the crystal structure and composition of the original film. Preliminary measurements on the ordered nanostructures were also presented.

Chapter 5 concludes the dissertation and suggests potential directions for further studies of ultrafast laser interactions with Sb_2Te_3 and other chalcogenide compounds.

References

[1.1] J. A. Van Vechten, R. Tsu, and F. W. Saris, "Nonthermal pulsed laser annealing of Si; plasma annealing", *Phys. Lett.* **74A**, 422 (1979)

[1.2] K. Sokolowski-Tinten, J. Bialkowski, and D. von der Linde, "Ultrafast laser-induced order-disorder transitions in semiconductors", *Phys. Rev. B* **51**, 14186 (1995)

[1.3] S. Hunsche, K. Wienecke, T. Dekorsy, and H. Kurz, "Impulsive softening of coherent phonons in tellurium", *Phys. Rev. Lett.* **75**, 1815 (1995)

[1.4] D. M. Fritz *et al.*, "Ultrafast bond softening in bismuth: mapping a solid's interatomic potential with X-rays", *Science* **315**, 633 (2007)

[1.5] L. Krusin-Elbaum, C. Cabral, Jr., K. N. Chen, M. Copel, D. W. Abraham, K. B. Reuter, S. M. Rossnagel, J. Bruley, V. R. Deline, "Evidence for segregation of Te in $Ge_2Sb_2Te_5$ films: effects on the "phase-change" stress", *Appl. Phys. Lett.* **90**, 141902 (2007)

[1.6] E. M. Larramendi, G. Berth, V. Wiedemeier, K-P Hüsch, A. Zrenner, U. Woggon, E. Tschumak, K. Lischka, and D. Schikora, "Intensity enhancement of Te Raman modes by laser damage in ZnTe epilayers", *Semicond. Sci. Technol.* **25**, 075003 (2010)

[1.7] M. Först, T. Dekorsy, C. Trappe, M. Laurenzis, and H. Kurz, "Phase change in $Ge_2Sb_2Te_5$ films investigated by coherent phonon spectroscopy", *Appl. Phys. Lett.* **77**, 1964 (2000)

[1.8] A. Q. Wu, X. Xu, and R. Venkatasubramanian, "Ultrafast dynamics of photoexcited coherent phonon in Bi_2Te_3 thin films", *Appl. Phys. Lett.* **92**, 01108 (2008)

[1.9] M. Deubel, G. von Freymann, M. Wegener, S. Pereira, K. Busch, and C. M. Soukoulis, "Direct laser writing of three-dimensional photonic-crystal templates for telecommunications", *Nature Mater.* **3**, 444 (2004)

[1.10] R. Eason, ed. *Pulsed laser deposition of thin films*. John Wiley & Sons, Inc. (2007)

[1.11] S. Preuss and M. Stuke, "Subpicosecond ultraviolet laser ablation of diamond: Nonlinear properties at 248 nm and time-resolved characterization of ablation dynamics", *Appl. Phys. Lett.* **67**, 338 (1995)

[1.12] G. Dumitru, V. Romano, H. P. Weber, M. Sentis, and W. Marine, "Femtosecond ablation of ultrahard materials", *Appl. Phys. A* **74**, 729 (2002)

[1.13] M. Birnbaum, "Semiconductor surface damage produced by ruby lasers", *J. Appl. Phys.* **36**, 3688 (1965)

[1.14] A. Borowiec and H. K. Haugen, "Subwavelength ripple formation on the surfaces of compound semiconductors irradiated with femtosecond laser pulses", *Appl. Phys. Lett.* **82**, 4462 (2003)

[1.15] Y. Shimotsuma, P. G. Kazansky, J. Qiu, and K. Hirao, "Self-organized nanogratings in glass irradiated by ultrashort light pulses", *Phys. Rev. Lett.* **91**, 247405 (2003)

[1.16] R. Buividas, L. Rosa, R. Šliupas, T. Kudrius, G. Šlekys, V. Datsyuk, and S. Juodkazis, "Mechanism of fine ripple formation on surfaces of (semi)transparent materials via a half-wavelength cavity feedback", *Nanotechnology* **22**, 055304 (2011)

[1.17] V. R. Bhardwaj, E. Simova, P. P. Rajeev, C. Hnatovsky, R. S. Taylor, D. M. Rayner, and P. B. Corkum, "Optically produced arrays of planar nanostructures inside fused silica", *Phys. Rev. Lett*. **96**, 057404 (2006)

[1.18] D. M. Rowe, ed. *Thermoelectrics Handbook*. CRC Press (2006)

[1.19] R. Venkatasubramanian, E. Siivola, T. Colpitts, and B. O'Quinn, "Thin-film thermoelectric devices with high room-temperature figures of merit", *Nature* **413**, 597 (2001)

[1.20] S. R. Ovshinsky, "Reversible electrical switching phenomena in disordered structures", *Phys. Rev. Lett.* **21**, 1450 (1968)

[1.21] M. Wuttig and N. Yamada, "Phase-change materials for rewriteable data storage", *Nature Mat.* **6**, 824 (2007)

[1.22] H. Zhang, C. Liu, X. Qi, X. Dai, Z. Fang, and S. Zhang, "Topological insulators in Bi_2Se_3, Bi_2Te_3, and Sb_2Te_3 with a single Dirac cone on the surface", *Nature Phys*. **5**, 438 (2009)

[1.23] S. Jujimori, S. Yagi, H. Yamazaki, and N. Funakoshi, "Crystallization process of SbTe alloy films for optical storage", *J. Appl. Phys.* **64**, 1000 (1988)

Chapter 2

Laser Pump-Probe Techniques

This chapter concerns the various pump-probe techniques employed in the dissertation to investigate the material dynamics using femtosecond lasers. The ability to probe over a wide range of time scales is made possible by the novel configuration of asynchronous optical sampling (ASOPS), a type of laser pump-probe setup that creates time delay via the slight repetition rate difference between the pump and the probe pulse trains. The first section (2.1) of this chapter will describe the working mechanism of ASOPS and the specific ASOPS system used in the time-resolved measurements in the dissertation.

The remaining sections (2.2-2.4) of this chapter will discuss the three types of dynamics studied using the ASOPS system. Section 2.2 talks about the optical phonons excited by ultrafast laser pulses in transparent and opaque materials. These THz vibrations are commonly seen in pump-probe experiments on Raman-active materials in the first few picoseconds following the pump excitation. Section 2.2 reviews the theories related to the coherent optical phonons. The experimental details and results on the specific sample of interest, Sb_2Te_3, will be left to Chapter 3, which explores laser-induced phase segregation with the help of optical phonons in Sb_2Te_3. Section 2.3 discusses the acoustic strains excited by ultrafast lasers. These strains usually present themselves as echoes of GHz oscillations in the thin film settings, with the spacing between neighboring echoes related to the speed of sound and the thickness of the film. This provides a convenient way for estimation of sample thickness in the studies of Sb_2Te_3 thin films. Both the related theory and the experimental results in Sb_2Te_3 thin films will be discussed in this section. Section 2.4 reviews the transient thermoreflectance technique. This includes probing the ultrafast carrier dynamics in the first few hundreds of femtoseconds, as well as the slow thermal transport dynamics on the nanosecond time scale. All of these dynamics mentioned above will show up in a mixed fashion in the time-resolved data of the pump-probe experiments. Separating and understanding the different excitations and time scales is crucial to the ultrafast studies of Sb_2Te_3 in this dissertation. This task is helped enormously by the ASOPS technique.

2.1 Asynchronous Optical Sampling

The laser pump-probe experiments in this dissertation employ a specific technique: asynchronous optical sampling (ASOPS). First demonstrated in the 1980s [2.1], ASOPS started to gain popularity in the most recent decade with the development of the more stable femtosecond lasers [2.2, 2.3]. ASOPS differs from the traditional pump-probe setup in its approach to control the time delay between the pump and the probe beams. For the traditional setup, the pump and the probe are usually derived from a single mode-locked laser beam via a beam-splitter. The relative time delay between the two beams is achieved by directing one of them, usually the probe, to a retro-reflector on a mechanical delay line and varying the extra distance the probe has to travel relative to the pump. However, the biggest inherent drawback of this conventional method is the beam alignment instability as the retro-reflector is moving along the delay line. This can pose a serious issue when studies of slower dynamics are desired. To create a delay time of 10 ns, for example, it requires a delay line of 1.5 meters long, making it virtually impossible to maintain beam alignment over the course of a complete scan. In addition, its scan rate is limited by the movement of the retro-reflector.

ASOPS, on the other hand, is able to overcome the above disadvantages by creating the time delay via a slight fixed difference in the repetition rates (Δf) of two fs lasers phase-locked together. If the repetition rates of the two lasers are f_1 and f_2, and $\Delta f \ll f_1$ and f_2, the time delay between each pair of pump and probe pulses will increase as multiples of $\Delta f / f_1 f_2 \approx \Delta f / f^2$ (see Figure 2-1). The ASOPS approach involves no moving parts and thus eliminates the instability problem inherent in the delay line method. The maximum time delay of the scan is $1/f$, and slow dynamics can be easily studied with lower-repetition-rate ASOPS systems (e.g., 10 ns for our 100 MHz lasers). The time resolution of ASOPS is $\Delta f/(fB)$, where B is the detector bandwidth [2.3]. In practice, the lower limit of Δf is determined by the pulse widths and the temporal jitter of the pulses. The amount of time it takes for one scan is $1/\Delta f$. Therefore, while a small Δf may increase the time resolution, it also slows down the data acquisition process.

Depending on the kind of dynamics one wishes to study, different choices of Δf are desirable. As an example, for a typical Δf of 1 kHz, the time resolution is 100 fs, and it takes 1 ms to complete one scan.

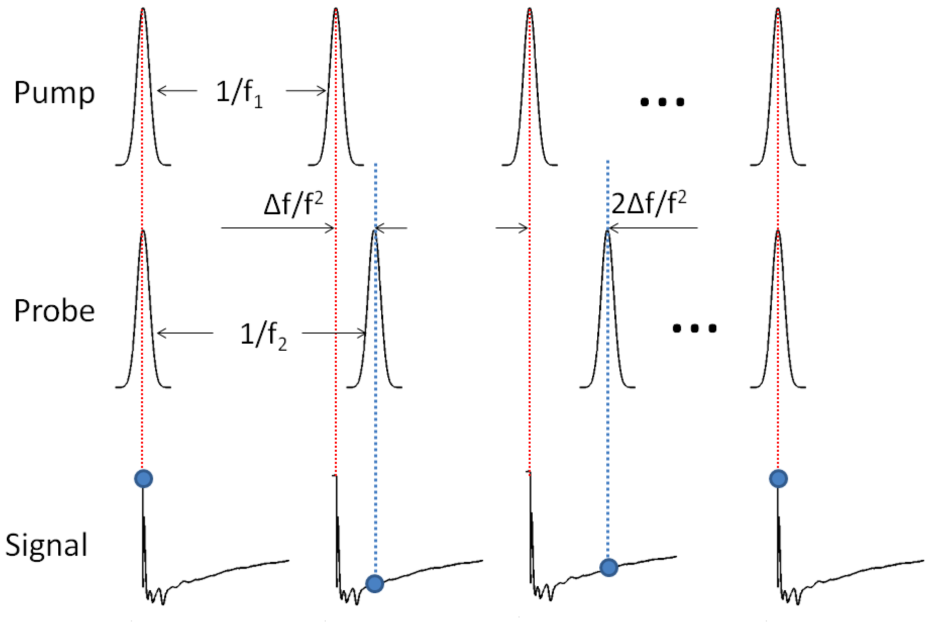

Figure 2-1. Schematic of the working principle of ASOPS

The ASOPS system used in the experiments was co-developed by Menlo Systems GmbH and the Clarke research group. Dr. Stoica from Clarke's group, in particular, has contributed greatly to the design and setup of the laser system for the pump-probe measurements [2.4]. The system consists of a pair of fiber lasers, each driven by a passively mode-locked fiber ring laser with erbium as the active medium. Each laser generates a train of pulses with a central wavelength of 1560 nm, a repetition rate of around 100 MHz and a FWHM of about 150 fs. One laser (the slave laser) is phase-locked to the other laser (the master laser) to synchronize the two repetition rates. The repetition rate difference between the two lasers is generated by shifting the 10th harmonic of the slave laser's repetition rate by an amount that is 10 times the desired repetition rate difference, while keeping the master laser's repetition rate unchanged. The repetition rate difference is maintained via a feedback loop and piezo motors [2.5].

The 1560 nm beam generated by the slave laser is sent to the second harmonic generation(SHG) module. Inside the module, the beam goes through a periodically poled lithium niobate (PPLN) crystal and frequency-doubled to 780 nm. The PPLN crystal's temperature is maintained at around 145^{o}C by an oven to minimize the photorefractive effect. The beam coming out of the PPLN crystal goes through a dichroic mirror and separates into a 780 nm beam and a 1560 nm beam, emerging from port 1 and port 2 of the SHG module correspondingly [2.4].

The location of the time zero reference for the pump-probe experiments is established through an external triggering system. Eight percent of the beam from the master laser and the 1560 nm beam from port 2 of the SHG module are collected and focused by a parabolic mirror onto a BBO crystal. When the pulses from each beam overlap in time, the sum-frequency generated (SFG) beam (780 nm) out of the BBO crystal will be detected by a Si photodetector sensitive to wavelengths 320 nm-1000 nm, and triggered as the time zero. Note that while the 8% of the pump beam is not strong enough to produce detectable second harmonics, the 1560 nm beam from the slave laser may produce second harmonics that interferes with the sum-frequency beam. Therefore, the trigger level needs to be carefully placed above the second harmonic level from the slave laser, and below the sum-frequency level. Additionally, the orientations of the parabolic mirror, the BBO crystal and the Si photodetector need to be fine-tuned to ensure that the sum-frequency signal received by the detector is maximized and much greater than the second harmonic signal.

For the pump-probe experiments in this dissertation work, the 1560 nm beam from the master laser acts as the pump beam, while the 780 nm beam from the slave laser acts as the probe beam. The pump beam is collimated and expanded by a pair of lenses, while the probe beam from the port 1 of the SHG module is collimated, and filtered spatially to ensure a nice Gaussian shape. The two beams are combined by a dichroic mirror, travel collinearly and are focused by a parabolic mirror onto the sample. The incidence can be normal or oblique. The reflected probe beam is collected by a lens and directed to the "Input +" port of a balanced detector. Meanwhile, 5% of the probe beam before the dichroic mirror is directed to the "Input -" port of the same balanced detector. The subtracted signal from the two ports is sent to the data acquisition board on a computer. A half-wave plate followed by a polarizer is used to control the intensity of the pump (Fig. 2-2).

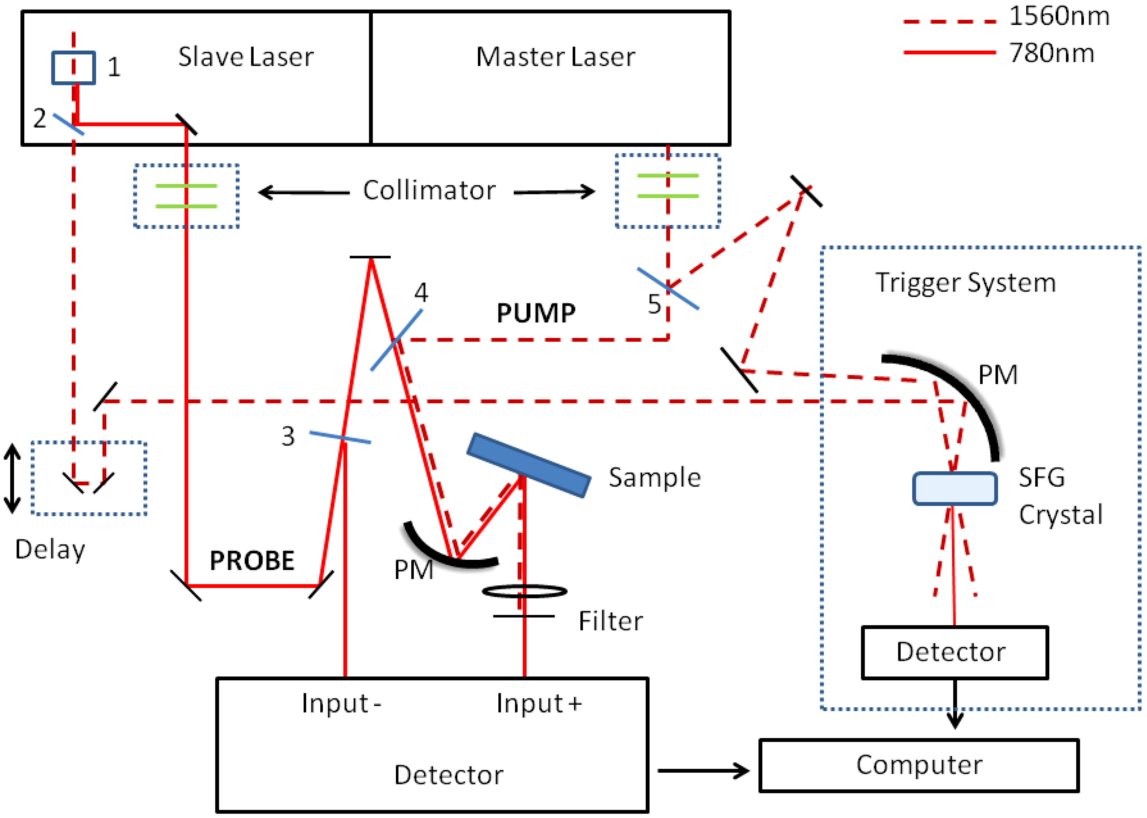

Figure 2-2. Schematic of the ASOPS system used in this dissertation work. The master laser and the slave laser are phase-locked by an electronic system. 1 is the PPLN crystal for the generation of the 780 nm beam. 2 and 4 are dichroic mirrors. 3 and 5 are beam splitters. PM stands for parabolic mirror. The collimators each consist of a pair of lenses for beam size adjustment and beam collimation.

2.2 Coherent Optical Phonons

Femtosecond laser irradiation of a material with Raman-active modes is known to generate THz coherent oscillations coinciding in frequency with its corresponding optical phonon modes. This phenomenon was initially recognized as a form of Raman scattering stimulated by the intense ultrafast laser pulse. Raman scattering is an inelastic process where a small portion (~10^{-6}) of the incident photons are scattered by the optical phonons and shifted in frequency by an amount corresponding to the energy absorbed or released by the phonons. In stimulated Raman scattering, the generated optical phonon field reinforces the Stokes light field at the expense of the incident light field, which in turn results in an even more excited phonon field.

Early experiments on stimulated Raman scattering involved either an intense laser above a certain threshold [2.6], or two pulsed lasers with a fixed frequency difference equal to that of the excited phonon [2.7]. In 1985, Yan and coworkers suggested the possibility of exciting these coherent optical phonons in a Raman-active material by a *single* ultrafast laser *without* the limitation of the intensity threshold, provided that the laser pulse is sufficiently short compared to the period of the phonon oscillations [2.8]. This conclusion was derived from their proposed "Impulsive Stimulated Raman Scattering" (ISRS) theory [2.8, 2.9], widely accepted later as the basis for the femtosecond-laser generation of coherent optical phonons in transparent materials.

In the ISRS theory, Yan *et al* modeled the phonon field Q as a harmonic oscillator driven by an impulsive force $F(t)$ [2.8]:

$$\frac{\partial^2 Q}{\partial t^2} + \gamma \frac{\partial Q}{\partial t} + \Omega^2 Q = F(t) = \frac{1}{2}\frac{\partial \chi}{\partial Q} E^2(t) \tag{2.1}$$

where Ω is the oscillator frequency, γ is the damping and E is the electric field of the laser pulse. χ is the electrical susceptibility and is related to the polarizability α by $\chi = N\alpha$, where N is the number of ions. Here, the laser pulse serves as the impulsive source that drives the oscillation. The quantity $\partial\chi/\partial Q$ can be expressed in tensor form $\chi^R_{kl} \approx \partial\chi_{kl}/\partial Q$ and is the Raman tensor. From here, the force term can be rewritten as $\sum_{kl} \chi^R_{kl} E_k E_l/2$.

Now we assume an excitation laser pulse with a Gaussian shape, propagating along the z direction inside a piece of material. The electric field of the laser is of the form:

$$E(z,t) = E_0 e^{-(t-zn/c)^2/2\tau^2} \cos\left[\omega(t - zn/c)\right] \tag{2.2}$$

where E_o is the field amplitude, τ is the pulse duration, and ω is the field frequency. It can be shown using Green's function method that the solution to Eqn. (2.1) is [2.8, 2.10]:

$$Q = \frac{\pi^{1/2}\tau}{4\Omega} e^{-\frac{\Omega^2\tau^2}{4}} |E_0|^2 \Big(\sum_{kl} \frac{\partial\chi_{kl}}{\partial Q} cos(\alpha_k) cos(\alpha_l)\Big) e^{-\gamma(t-zn/c)} sin[\Omega(t - zn/c)] \tag{2.3}$$

where $cos(\alpha_{k,l}) = E_{k,l}/E_0$. From Eqn. (2.3) we see that as a result of the impulsive laser excitation, a phonon field propagating in the same direction as the laser is generated. A small $\Omega^2\tau^2$ ensures that the term $e^{-\Omega^2\tau^2/4}$ remains large for a significant phonon field amplitude. This leads to the ISRS's requirement that the laser pulse duration is short compared to one phonon oscillation cycle. This requirement can also be understood from the perspective of the frequency domain: the bandwidth of the ultrashort laser pulse needs to be wide enough to satisfy energy conservation with respect to the generated phonon frequency.

The presence of the optical phonons changes the complex refractive index of the material, which in turn modifies the reflectivity and transmittance of the probe laser that arrives at a later time. The modified wave equation of the probe's electric field e_k is:

$$\nabla^2 e_k = \frac{1}{c^2} \times \frac{\partial^2}{\partial t^2}(n^2 e_k + 4\pi \sum_l \frac{\partial \chi_{kl}}{\partial Q} Q(z,t) e_l) \tag{2.4}$$

Solving this equation gives e_k, and from that, the relative reflectivity change of the probe can be shown to be [2.10]:

$$\Delta R/R \approx -\frac{4\sigma}{\Omega(n-1)(n+1)} e^{-\gamma\delta/2} sin(\Omega\delta) \tag{2.5}$$

where δ is the time delay of the probe to the pump, and:

$$\sigma = \frac{\pi^{3/2}\tau}{2n} |E_0|^2 e^{-\frac{\Omega^2\tau^2}{2}} \sum_{kl,mp} (\frac{\partial \chi_{mp}}{\partial Q} cos(\alpha_m) cos(\alpha_p)) \times (\frac{\partial \chi_{kl}}{\partial Q} cos(\alpha_k) cos(\alpha_l)) \tag{2.6}$$

Therefore, the detected phonon oscillations by the probe will be an exponentially decaying sine function in delayed-time.

The above calculations assume that the pump pulse is far away from electronic resonance, and therefore electronic excitation can be safely ignored. The application of ISRS to opaque materials, on the other hand, requires a much more complicated treatment. Interestingly, in the early pump-probe experiments of coherent optical phonons in opaque materials, the oscillations are predominantly of A_1 symmetry, even for materials whose A_1 and E modes are of comparable strength in the Raman scattering experiments [2.11]. Since ISRS theory is based on Raman scattering, all Raman modes should be present if the excitation is of the ISRS nature. The difficulty encountered by the ISRS theory to explain the selective excitation of A_1 modes led to the proposal of a different phonon generation mechanism by Zeiger *et al* in opaque materials: displacive excitation of coherent phonons (DECP) [2.11, 2.12].

Unlike the ISRS theory, which assumes that laser pump pulse drives the ions out of their equilibrium position, the DECP theory assumes that the pump pulse gets absorbed by the opaque material and alters the temperature distribution and band distribution of the electrons. The excitation of the electrons introduces an A_1 displacement of the equilibrium position of the ions that preserves the symmetry of the unit cell during the displacement, and set the ions oscillating around the new quasi-equilibrium position. Other Raman modes lower the symmetry of the unit cell, and thus are not the favorable displacement upon electronic excitation. This explains the predominant observation of A_1 modes in ultrafast coherent optical phonon excitations in opaque materials. In DECP, it is the equilibrium coordinates that get shifted by the electronic excitations, and the "pushing force" that starts the oscillation is governed by the excitation and relaxation of the electrons. The equation of motion for the ion coordinates $Q(t)$ is [2.12]:

$$\frac{\partial^2 Q(t)}{\partial t^2} + \omega_0^2[Q(t) - Q_0(t)] + 2\gamma\frac{\partial Q(t)}{\partial z} = 0 \tag{2.7}$$

where $Q_0(t)$ is the new quasi-equilibrium position. Its dynamics follows that of the electrons and can be approximated by a step exponential decay: $Q_0(t) \propto e^{-\beta t}u(t)$, where $u(t)$ is the Heaviside step function, and β is the electronic relaxation rate. With the solution $Q(t)$ to Eqn. (2.7), the relative reflectivity change due to the phonon oscillation was shown to be [2.12]:

$$\frac{\Delta R}{R} \propto \frac{\omega_0^2}{\omega_0^2 + \beta^2 - 2\gamma\beta}[e^{-\beta t} - e^{-\gamma t}(cos(\Omega t) - \frac{\beta'}{\Omega}sin(\Omega t))] \tag{2.8}$$

where $\Omega = \sqrt{\omega_0^2 - \gamma^2}$, and $\beta' = \beta - \gamma$. For β and $\gamma \ll \omega_0$, $\Delta R/R$ resembles a decaying negative cosine function, with oscillation frequency corresponding to the A_{1g} phonon mode. The cosine function is shifted in phase by an amount determined by β'/Ω. Early pump-probe experiments in Bi, Te, and Sb found excellent agreement with the DECP predictions [2.11, 2.12].

As later experiments revealed that E_g modes can indeed be excited and detected in opaque materials using the pump-probe configurations, theoretical efforts have been made to unify the two models within the Raman scattering framework [2.13, 2.14]. In 2002, Stevens and coworkers proposed the two-tensor model, where the DECP theory is included as a special case of ISRS [2.15]. Working with the density matrix formulism, the two-tensor model started by writing the perturbation to the Hamiltonian of the system as:

$$H_{int} = -\hat{\Xi}\hat{\mathrm{Q}} - \hat{\Delta}\cdot\mathbf{E} \tag{2.9}$$

where $-\hat{\Xi}\hat{Q}$ is the electron-phonon interaction and $\hat{\Delta}\cdot\mathbf{E}$ is the electron-photon interaction. $\hat{\Xi}$ is the deformation potential caused by the presence of phonon field $\hat{Q}$, and $\hat{\Delta}$ is the dipole moment.

The first and the second-order corrections to the density matrix can be calculated according to [2.16]:

$$\rho_{nm}^{(1)}(t) = \int_{-\infty}^{t} \frac{-i}{\hbar}[H_{int}, \rho^{(0)}]_{nm} e^{(i\omega_{nm}+\gamma_{nm})(t'-t)dt'} \tag{2.10}$$

$$\rho_{nm}^{(2)}(t) = \int_{-\infty}^{t} \frac{-i}{\hbar}[H_{int}, \rho^{(1)}]_{nm} e^{(i\omega_{nm}+\gamma_{nm})(t'-t)dt'} \tag{2.11}$$

where $\rho_{nm}^{(0)} = 0$ for $n \neq m$ is the ground state density matrix. From here, the change in polarization $\mathbf{P}^R$ due to the phonon and the driving force $F(t)$ that initiates the phonon oscillations can be shown to be [2.15]:

$$\mathbf{P}^R(t) = \frac{1}{Nv_c}\langle\Delta\rangle^R = \frac{1}{Nv_c}\mathrm{tr}\big(\rho^{(2)}\Delta\big) \tag{2.12}$$

$$\mathrm{P}_k^R(t) = \frac{1}{2\pi}\sum_{l}\int_{-\infty}^{+\infty}\int_{-\infty}^{+\infty} e^{-i(\omega-\Omega)t}\chi_{kl}^R(\omega,\omega-\Omega)E_l(\omega)Q^*(\Omega)d\omega d\Omega \tag{2.13}$$

and

$$\begin{aligned} F(t) &\equiv \langle\hat{\Xi}\rangle = \mathrm{tr}(\rho^{(2)}\hat{\Xi}) \\ &= \frac{Nv_c}{4\pi}\sum_{kl}\int_{-\infty}^{+\infty}\int_{-\infty}^{+\infty} e^{-i\Omega t}E_l(\omega)\pi_{kl}^R(\omega,\omega-\Omega)E_k^*(\omega-\Omega)d\omega d\Omega \end{aligned} \tag{2.14}$$

where N is the number of cells and v_c is the cell volume. π^R and $\chi^R$are the two Raman tensors responsible for the generation and detection of coherent optical phonons in the pump-probe configuration. In the original ISRS theory, these two Raman tensors are assumed to be the same in Eqns. (2.3) and (2.4). However, a few approximations to π^R and χ^R (considering only one term with two resonant denominators, $\Xi_{nm} = \Xi_0 = \text{const}$, negligible dissipation, two-band process, Ω/ω«1) revealed that they are drastically different in their imaginary parts [2.15]:

$$\pi^R \approx \frac{\Xi_0}{4\pi\hbar}[\frac{d\mathrm{Re}(\varepsilon)}{d\omega} + 2i\frac{\mathrm{Im}(\varepsilon)}{\Omega}] \tag{2.15}$$

$$\chi^R \approx \frac{\Xi_0}{4\pi\hbar}[\frac{d\mathrm{Re}(\varepsilon)}{d\omega} + i\frac{d\mathrm{Im}(\varepsilon)}{d\omega}] \tag{2.16}$$

where ε is the dielectric constant. In transparent materials, the real part of the tensors dominates, and so $\pi^R = \chi^R$. Therefore, the same Raman tensor can be used in both generation and detection of phonons. When the laser pump pulse is near electronic resonance with the materials, however, the imaginary parts of the tensors dominates, and the two tensors can differ significantly. For example, at around 2 eV in Sb, $\mathrm{Im}(\varepsilon)/\Omega$ and $d\mathrm{Im}(\varepsilon)/d\omega$ differ by two orders of magnitude [2.15].

To see how the real and imaginary parts of π^R contribute to the driving force, a Fourier transform can be performed on $F(t)$ to obtain:

$$\begin{aligned}\tilde{F}(\Omega) &\propto \int_{-\infty}^{+\infty} dte^{i\Omega t} \int_{-\infty}^{+\infty}\int_{-\infty}^{+\infty} d\omega d\Omega' e^{i\Omega' t} E(\omega)\pi^R(\omega, \omega - \Omega')E^*(\omega - \Omega') \\ &\propto \int_{-\infty}^{+\infty} d\omega E(\omega)\pi^R(\omega, \omega - \Omega)E^*(\omega - \Omega) \\ &\approx [\frac{d\mathrm{Re}(\varepsilon)}{d\omega} + 2i\frac{\mathrm{Im}(\varepsilon)}{\Omega}]\int_{-\infty}^{+\infty} dte^{i\Omega t}|E(t)|^2\end{aligned} \tag{2.17}$$

For transparent materials, $d\mathrm{Re}(\varepsilon)/d\omega$ dominates, and the corresponding driving force $F(t)$ has the form:

$$\begin{aligned}F(t) &\propto \int_{-\infty}^{+\infty} d\Omega e^{-i\Omega t}\frac{d\mathrm{Re}(\varepsilon)}{d\omega}\int_{-\infty}^{+\infty} dt' e^{i\Omega t'}|E(t')|^2 \\ &\propto |E(t)|^2\end{aligned} \tag{2.18}$$

The driving force follows the temporal shape of the pump laser pulse, a characteristic of impulsive excitation of the phonons. For opaque materials, $2i\ (\mathrm{Im}(\varepsilon))/\Omega$ dominates, and $F(t)$ takes the form:

$$F(t) \propto \int_{-\infty}^{+\infty} d\Omega e^{-i\Omega t} \frac{2\mathrm{Im}(\varepsilon)}{-i\Omega} \int_{-\infty}^{+\infty} dt' e^{i\Omega t'} |E(t')|^2$$
$$\propto \int_{-\infty}^{t} |E(t')|^2 dt' \qquad (2.19)$$

The driving force in this case has an error-function-like temporal profile for a Gaussian-shape laser pulse, indicative of displacive excitation. The transiently stimulated Raman scattering mechanism is thus extended from transparent materials to opaque materials, where both the virtual (transparent) and the real (opaque) electronic excitations are incorporated into the complex Raman tensor π^R.

2.3 Acoustic Strain Propagation

The acoustic pulses observed during laser pump-probe experiments have been especially useful for investigating film properties such as thickness or defects as a non-destructive probing technique [2.17, 2.18]. The configuration of these measurements usually involves shining the pump on the surface of an absorbent thin film on a substrate, and monitoring the probe reflectivity change of the film. The related theory was first proposed by Thomsen and coworkers and attributed to the propagation of acoustic strains inside the film which are formed from the pulsed laser-induced thermal expansion [2.19]. Thomsen started by considering a temperature rise near the film surface following a pump excitation:

$$\Delta T(z) = (1 - R) \frac{Q}{A\zeta C} e^{-z/\zeta} \qquad (2.20)$$

where R is the optical reflectivity, Q is the energy deposited by the pump pulse, A is the illuminated area on the film, ζ is the penetration depth of the pump into the film, C is the specific heat per unit volume, and z is in the direction perpendicular to the film surface.

Note that two assumptions are made here: 1. The film thickness d is much larger than ζ. 2. A is much larger than d or ζ, so that the process can be approximated by a 1D model. As a result of the second assumption, the stress, σ, only varies along the z direction, and therefore the only non-zero component of the strain tensor η is η_{zz}. Following the temperature rise, the stress is related to the strain by [2.19]:

$$\sigma_{zz}(z,t) = 3\frac{1-\nu}{1+\nu}B\eta_{zz}(z,t) - 3B\beta\Delta T(z) = \rho v_s^2\eta_{zz}(z,t) - 3B\beta\Delta T(z) \qquad (2.21)$$

where ν is the Poisson ratio, B is the bulk modulus, β is the linear expansion coefficient, ρ is the density, and v_s is the longitudinal sound velocity. The elastic wave equation is:

$$\rho\frac{\partial^2 u_z(z,t)}{\partial t^2} = \frac{\partial \sigma_{zz}(z,t)}{\partial z} \qquad (2.22)$$

Here, u_z is the displacement in the z direction, and satisfies:

$$\eta_{zz}(z,t) = \frac{\partial u_z(z,t)}{\partial z} \qquad (2.23)$$

The boundary condition is zero stress at the film surface: $\sigma_{zz}(0,t) = 0$. This gives $\eta_{zz}(0,t) = 3B\beta(1-R)Q/A\zeta C\rho v_s^2$. The initial condition is $\eta_{zz}(z,0) = 0$ and $\partial\eta_{zz}/\partial t\,\big|_{t=0} = 0$. Eqns. (2.21) - (2.23) can be combined and rewritten as:

$$\frac{\partial^2\eta_{zz}(z,t)}{\partial t^2} = v_s^2\frac{\partial^2\eta_{zz}(z,t)}{\partial z^2} - v_s^2\eta_{zz}(0,t)\frac{e^{-z/\zeta}}{\zeta^2} \qquad (2.24)$$

The solution to Eqn. (2.24) gives strain [2.19]:

$$\eta_{zz}(z,t) = \eta_{zz}(0,t)e^{-z/\zeta} - \frac{1}{2}\eta_{zz}(0,t)[e^{-(z+v_st)/\zeta} + e^{-|z-v_st|/\zeta}sgn(z-v_st)] \qquad (2.25)$$

And the corresponding stress can be found by substituting (2.25) in (2.21):

$$\sigma_{zz}(z,t) = -\frac{\rho v_s^2}{2}\eta_{zz}(0,t)[e^{-(z+v_st)/\zeta} + e^{-|z-v_st|/\zeta}sgn(z-v_st)] \qquad (2.26)$$

Eqn. (2.25) shows that the strain is represented by a superposition of an exponential decay near the film surface and a bipolar pulse of 2ζ in width that propagates at v_s away from the film surface after time zero. The exponential decay corresponds to the first term in (2.25) and is constant in time. The bipolar pulse comes from the second term in (2.25) and is composed of two waves traveling in opposite directions. As an example, the strain at different times inside the film is plotted in Figure 2-3.

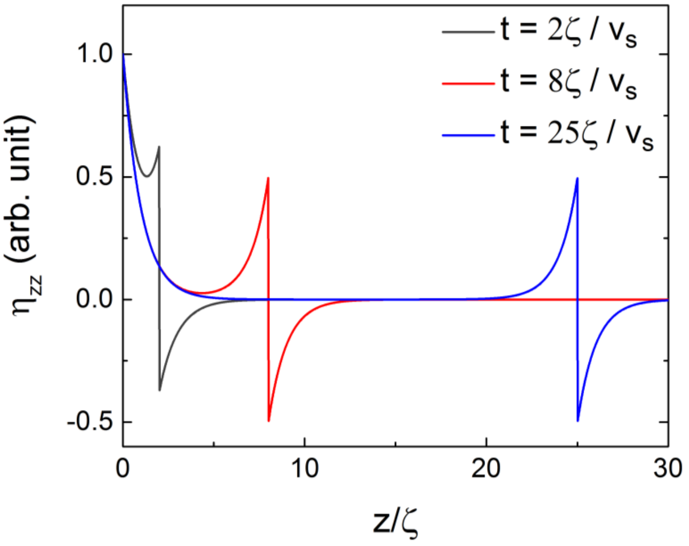

Figure 2-3. Strain pulse propagation at different times.

In practice, the pump pulse has a finite duration, and the instantaneous excitation in (2.20) is a good approximation only when $v_s\tau \ll \zeta$, where τ is the pump pulse duration. This condition is satisfied for all cases in this dissertation.

So far, the thermal diffusion from the initial exponential decay profile has been ignored for simplification. The effect of thermal diffusion is to broaden the generation of the strain pulses due to thermal excitation both in time and in space, and consequently alter the shape of the strain pulse. Such an effect is negligible only when the strain pulse has already left the heated region near the surface long before the temperature profile changes significantly due to the thermal diffusion, i.e. $D \ll v_s\zeta$. For the commonly-used metal transducers such as Al, D is usually comparable to $v_s\zeta$, and the pulse shape will be modified by the thermal diffusion.

As the strain pulse changes the complex refractive index of the film near the surface, the reflectivity of the probe changes accordingly. When there is no strain pulse in the film, the reflection coefficient of the probe pulse is:

$$r_0 = \frac{1 - n - ik}{1 + n + ik} \tag{2.27}$$

where n and k are the real and imaginary parts of the refractive index, and are related to the dielectric constant ε in the film by $\varepsilon = (n + ik)^2$. However, the presence of the strain pulses modifies the dielectric constant in time and space, and leads to a change in the reflection coefficient. The reflectivity of the probe ΔR can thus be calculated by solving the modified Helmholtz equation of the probe's electric field:

$$\frac{\partial^2 E}{\partial z^2} = -\frac{\omega^2}{c^2}[\varepsilon + \Delta\varepsilon(z,t)]E \tag{2.28}$$

where $\Delta\varepsilon(z,t)$ is the change in the film's dielectric constant due to the strains:

$$\Delta\varepsilon(z,t) = 2(n + ik)\left(\frac{\partial n}{\partial \eta_{zz}} + i\frac{\partial k}{\partial \eta_{zz}}\right)\eta_{zz}(z,t) \tag{2.29}$$

Thomsen *et al.* approached the problem by first considering a δ-function perturbation at z = z': $\Delta\varepsilon = F\delta(z - z')$, and then generalized to an arbitrary perturbation $\Delta\varepsilon(z', t)$. The new reflection coefficient with the presence of strain is found to be [2.19]:

$$r(t) = r_0 + \frac{ik_0^2}{2k} t_0 \widetilde{t_0} \int_0^\infty dz'^{e^{2ikz'}} \Delta\varepsilon(z', t) \tag{2.30}$$

From this, the reflectivity change can be expressed as a summation of the weighted strain strength at each point along the z-direction:

$$\Delta R(t) = \int_0^\infty f(z)\eta_{zz}(z,t)dz \tag{2.31}$$

The weight coefficient $f(z)$, an exponentially decaying sinusoidal function in space, is called the "sensitivity function" by Thomsen *et al.*, and tells how the strain at a particular location z contributes to the total reflectivity change:

$$f(z) = f_0[\frac{\partial n}{\partial \eta_{zz}} sin(\frac{4\pi nz}{\lambda} - \phi) + \frac{\partial \kappa}{\partial \eta_{zz}} cos(\frac{4\pi nz}{\lambda} - \phi)]e^{-z/\zeta} \tag{2.32}$$

$$f_0 = \frac{8\omega[n^2(n^2 + \kappa^2 - 1)^2 + \kappa^2(n^2 + \kappa^2 + 1)^2]^{1/2}}{c[[(n + 1)^2 + \kappa^2]^2} \tag{2.33}$$

$$\tan\phi = \frac{\kappa(n^2 + \kappa^2 + 1)}{n(n^2 + \kappa^2 - 1)} \tag{2.34}$$

While roughly following the bipolar profile of the strain, the shape of the reflectivity change also depends on the ratio of the piezo-optic couplings $\partial n/\partial \eta_{zz}$ to $\partial \kappa/\partial \eta_{zz}$, which can be estimated from fitting the experiment plots. Figure 2-4 shows an example of an acoustic strain pulse generated and detected on an Al film on Sb_2Te_3.

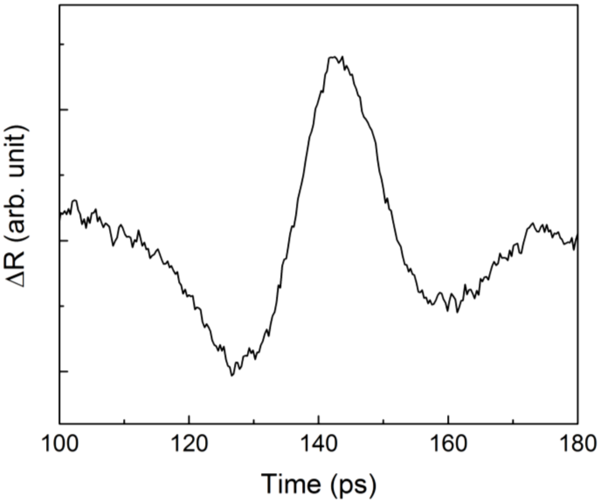

Figure 2-4. Acoustic strain pulse detected on an Al film with a pump-probe configuration. The slowly-varying thermal background is subtracted from the original plot.

The calculations so far have considered only the case of a semi-infinite film, where the strain pulse propagates away from the surface indefinitely. In the case of a thin film on a substrate, however, the strain pulse encounters the film/substrate interface, and part of the pulse will be reflected back towards the film surface, with the reflection coefficient r_{FS} determined by the acoustic impedances of the film Z_f and the substrate Z_s:

$$r_{FS} = \frac{Z_s - Z_f}{Z_s + Z_f} \tag{2.35}$$

As a result of the partial reflection and partial transmission at the film/substrate and the film/air interfaces, a series of bipolar pulses (echoes) similar to Figure 2-4 with successive amplitude damping can be observed in the pump-probe experiments. The temporal distance τ between two adjacent pulses corresponds to the amount of time it takes for the pulse to complete one round-trip across the film: $\tau = 2d/v_s$, where d is the film thickness. This allows for evaluation of the film thickness if the speed of sound is known, or vice versa.

For a quick estimation or confirmation of the thicknesses of the Sb_2Te_3 films grown by MBE, direct pump excitation on the film without any metal transducer layer was often performed for convenience. For Sb_2Te_3, $D/v_s\zeta$ ≈0.06 [2.20-2.22], and echo shape broadening from thermal diffusion is minimal. However, strain can also be generated by photo-excited carriers before the carriers reach thermal equilibrium with the lattice. It has already been demonstrated in metals that the time scale for the electron-electron scattering may extend into the ps regime [2.23]. During this "non-thermal regime" where the carriers are settling for thermal equilibrium among themselves with the lattice still cold, the contribution of hot carriers to the strain generation is nontrivial and the strain pulses can be greatly influenced by the carrier diffusion [2.24]. This is especially evident in Sb_2Te_3 thin films of less than 150 nm thickness, as the photo-excited carriers quickly diffuse to the film/substrate interface before losing significant energy to the lattice. There, the carriers generate an additional set of acoustic echoes that is half way between the usual set of echoes generated near the surface of the film (film/air interface). Figure 2-5 shows an example of the detected acoustic echoes on a 100 nm Sb_2Te_3 thin film on a sapphire substrate. Starting at around 50 ps, a series of six echoes can be seen. The first, third and fifth echoes correspond to the strain excited near the Sb_2Te_3/sapphire interface, while the second, fourth and sixth echoes correspond to the strain excited at the Sb_2Te_3/air interface. The polarities of the neighboring echoes (e.g. 1st and 2nd) remain the same while those of adjacent echoes in either series (e.g. 1st and 3rd) have opposite signs, due to $Z_{Al_2O_3} > Z_{Sb_2Te_3} > Z_{air}$.

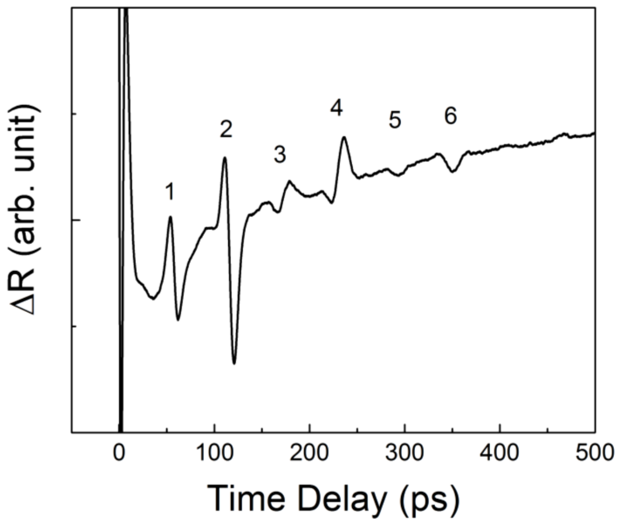

Figure 2-5. Two sets of acoustic echoes detected on a 100 nm Sb_2Te_3 film on a sapphire substrate. $\Delta f = 1kHz$ was used for the ASOPS detection, resulting in a time step of 0.1 ps in the figure.

2.4 Transient Thermoreflectance

In addition to the coherent lattice vibrations, changes in the electron and lattice temperatures by the pump pulse can also result in modulations of the probe's reflectivity and transmittance. Early works in Cu and Au have revealed nonequilibrium electron heating and cooling with the help of fs-laser pump-probe setups [2.25-2.28]. In these experiments, the pump laser pulse excites a large amount of electrons that quickly reach thermal equilibrium among themselves via electron-electron scattering within hundreds of fs. The much smaller heat capacity of the electron system compared to that of the lattice enables the electron temperature to rise rapidly to a level significantly higher than that of the lattice. This drastic increase in electron temperature is manifest as a sharp peak in the ΔR of the probe pulse immediately following the pump excitation, due to the transient thermomodulation of the complex dielectric constant of the material [2.25-2.27]. The electrons subsequently relax their energy to the lattice via electron-phonon scattering. This process is shown as a slower decay of the initial sharp peak over a few picoseconds.

The nonequilibrium dynamics of the electron and lattice systems right after pulsed laser excitation can be approximated by the Two-Temperature Model [2.29, 2.30], which assumes that the electrons and the lattice can each be characterized by their respective temperatures T_e and T_l. The model is represented by two coupled equations [2.29, 2.30]:

$$C_e \frac{\partial T_e}{\partial t} = \kappa_e \nabla^2 T_e - g(T_e - T_l) + Q(z,t) \tag{2.36}$$

$$C_l \frac{\partial T_l}{\partial t} = g(T_e - T_l) \tag{2.37}$$

where Q is the source term accounting for the laser excitation with the form exp $(-\alpha z - t^2/\tau^2)$. $C_e = \gamma T_e$ and C_l are the heat capacities of the electrons and the lattice. κ_e is the electron thermal conductivity. g, the electron-phonon coupling factor, is assumed constant, and its value can be obtained by fitting the data from the pump-probe experiments [2.31]. Figure 2-6 demonstrates an example of simulated electron and lattice dynamics in Au immediately after pulsed laser excitation. Equations (2.36) and (2.37) were used, with boundary conditions of $\partial T_{e,l}/\partial z\big|_{z=0,d} = 0$ and initial conditions of $T_{e,l}\big|_{t=0} = 300$ K, where d is the bottom of the Au film. The parameters for Au were taken from [2.30].

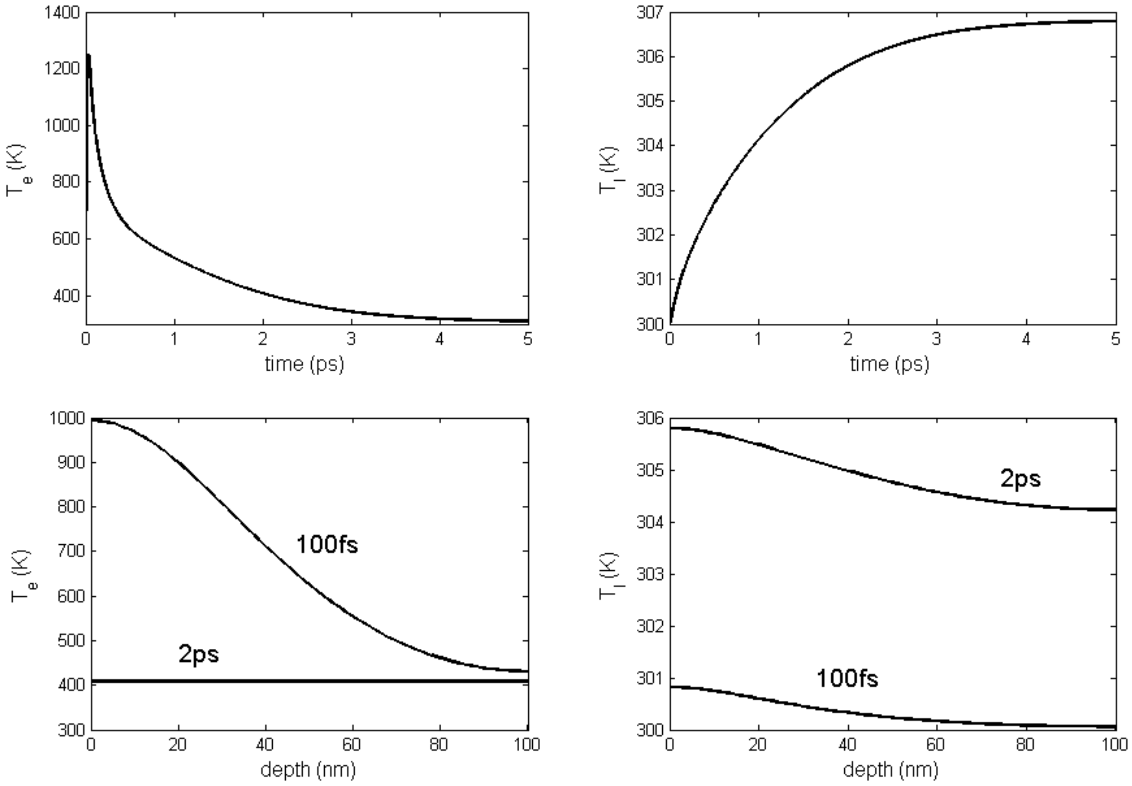

Figure 2-6. Simulated electron (left) and lattice (right) dynamics in Au following fs laser excitation, according to Eqn. (2.36) and (2.37). The upper two graphs illustrate T_e and T_l near the surface vs. time. The lower two graphs show T_e and T_l as a function of depth into the Au film at 100 fs and 2 ps after the excitation.

As the electrons cool down after a few picoseconds, the lattice temperature near the surface continues to rise. The lattice temperature homogeneity along the depth of the film will be reached on the longer time scales of picoseconds to nanoseconds, as the heat near the surface slowly diffuses into the film. This slower dynamics of thermal transport by the lattice can be monitored with the Transient Thermoreflectance method, first demonstrated by Paddock and Easley [2.32]. Based on the pump-probe technique used for monitoring the ultrafast dynamics of the electron heating and cooling, Paddock and Easley measured the probe reflectivity change on Ni for over 140 ps after excitation. The thermal diffusivity of Ni was obtained by fitting the slowly-decaying temperature background with the one-dimensional heat diffusion equation:

$$C\frac{\partial T(z,t)}{\partial t}=\kappa\frac{\partial^2 T(z,t)}{\partial z^2}+Q(z,t) \tag{2.38}$$

where C is the specific heat per unit volume, and κ is the thermal conductivity. The source term Q is the laser excitation, again in the form of exp $(-\alpha z-t^2/\tau^2)$.

In the case of a thin film on a substrate, the film-substrate interface presents a thermal boundary resistance R_K as the heat travels across the interface. Such a film-substrate geometry is commonly seen in thermal transport measurements where a thin layer of metal is deposited on a piece of substrate whose thermal diffusivity is to be measured. In this configuration, the metal film acts as a transducer that absorbs the pump laser energy and creates a slightly raised temperature compared to the substrate within tens of picoseconds. The heat flows through the interface as governed by the definition of thermal boundary resistance, and continues to flow across the substrate according to the heat diffusion equation. This whole process can be approximated by the following equations [2.33-2.35]:

$$\kappa_m\frac{\partial^2 T_m(z,t)}{\partial z^2}=C_m\frac{\partial T_m(z,t)}{\partial t}-Q(z,t) \tag{2.39}$$

$$\kappa_s\frac{\partial^2 T_s(z,t)}{\partial z^2}=C_s\frac{\partial T_s(z,t)}{\partial t} \tag{2.40}$$

$$\kappa_m\frac{\partial T_m(z,t)}{\partial z}\bigg|_{z=d}=\kappa_s\frac{\partial T_s(z,t)}{\partial z}\bigg|_{z=d} \tag{2.41}$$

$$\kappa_s\frac{\partial T_s(z,t)}{\partial z}\bigg|_{z=d}=-\frac{T_m(d,t)-T_s(d,t)}{R_K} \tag{2.42}$$

where κ_s is the thermal conductivity of the substrate, T_s and T_m are the temperatures of the substrate and the metal film, C_s and C_m are the specific heat per unit volume of the substrate and the film, and d is the metal film thickness. Eqns. (2.39) and (2.40) describe the heat flow inside the metal film and the substrate. Eqn. (2.42) follows the thermal boundary resistance definition. Like Eqn. (2.38), this equation set ignores the ultrafast electron dynamics in the metal and uses instead the parabolic one-step heating model for the metal lattice temperature, a good approximation for slow dynamics studies. Fitting this model to the experimental data over the long time scale of heat diffusion inside the substrate can yield values of κ_s and R_K.

The use of metal transducer in thermal transport measurements is especially useful for thin film samples on substrates. In the case of Sb_2Te_3 thin films on sapphire substrates, the much larger diffusivity of the photoexcited carriers compared to the thermal diffusivity makes thermal transport measurements challenging without a transducer. Direct excitation of an Sb_2Te_3 thin film with the pump laser may generate photoexcited carriers that quickly homogenize the temperature across the whole film. The presence of a transducer ensures that the excitation on the surface of the Sb_2Te_3 film is of a thermal nature. Figure 2-7 shows the result of a thermoreflectance measurement of a 70 nm Sb_2Te_3 film on sapphire with a 120 nm Al transducer at the film surface. The initial sharp increase in ΔR corresponds to the rapid cooling of the metal lattice as the heat flows across the Al/Sb_2Te_3 boundary. The slow decay over the next few nanoseconds corresponds to the much slower heat transfer process across the Sb_2Te_3 film.

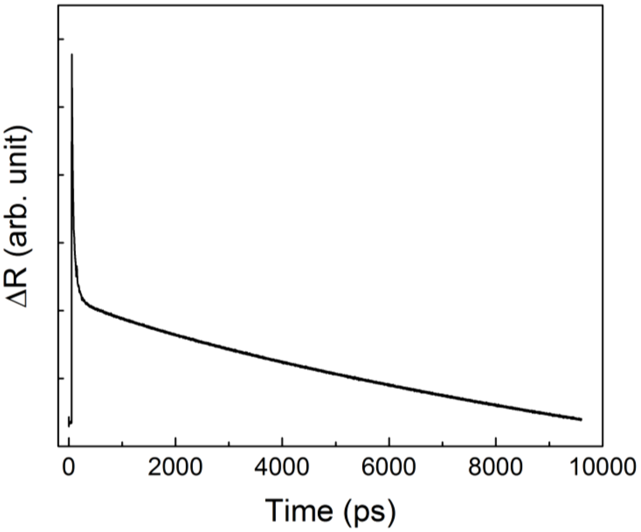

Figure 2-7. Transient thermoreflectance on a 70 nm Sb_2Te_3 film on sapphire with a 120 nm Al transducer.

Due to the small thermal conductivity of Sb_2Te_3, the thermal decay over 10 ns is represented by an almost linear behavior. This makes it challenging to accurately extract the thermal conductivity value of Sb_2Te_3 by data fitting from only 10 ns -- the maximum time delay achievable with our 100 MHz-repetition-rate ASOPS system. Additionally, if the transducer is deposited on rough Sb_2Te_3 surfaces such as those treated with laser irradiation in Chapter 4, the strong acoustic phonons greatly distort the thermoreflectance plot, making it almost impossible to obtain meaningful interpretations with the time-resolved data. These experimental difficulties can be circumvented by employing the front-pump/back-probe configuration, where the pump laser excites the metal transducer and the probe laser monitors the reflectivity change at the film/substrate interface (Figure 2-8) [2.36]. In this case, a double-side-polished sapphire substrate, transparent to the 780 nm beam, is used to minimize the absorption and scattering of the probe inside the substrate.

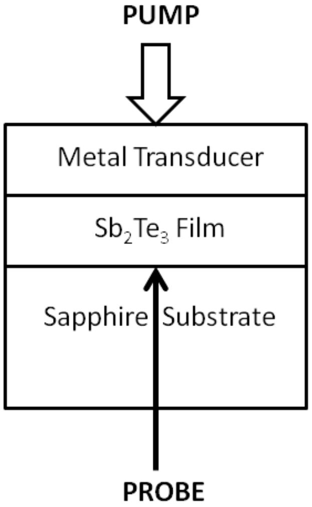

Figure 2-8. Schematic of the front-pump/back-probe configuration.

In this thermoreflectance setup, the pump and the probe travels collinearly until the probe is reflected by the dichroic mirror while the pump goes through it. The pump is focused by a parabolic mirror onto the surface of the metal film on the sample, with a focal spot size of ~10 μm in diameter. The probe is expanded by a pair of lenses and then focused by a microscope objective onto the film/substrate interface, with a spot size of ~ 6 μm in diameter. Forty-five percent of the probe before entering the objective is collected by a beam splitter as a reference signal for the "- input" port of the balanced detector. Forty-five percent of the probe beam reflected off the film/substrate interface also gets reflected by the beam splitter and sent to the "+

input" port of the detector. The path lengths travelled by the pump and the probe were adjusted carefully so that the two pulses overlap at t = 0 (Figure 2-9).

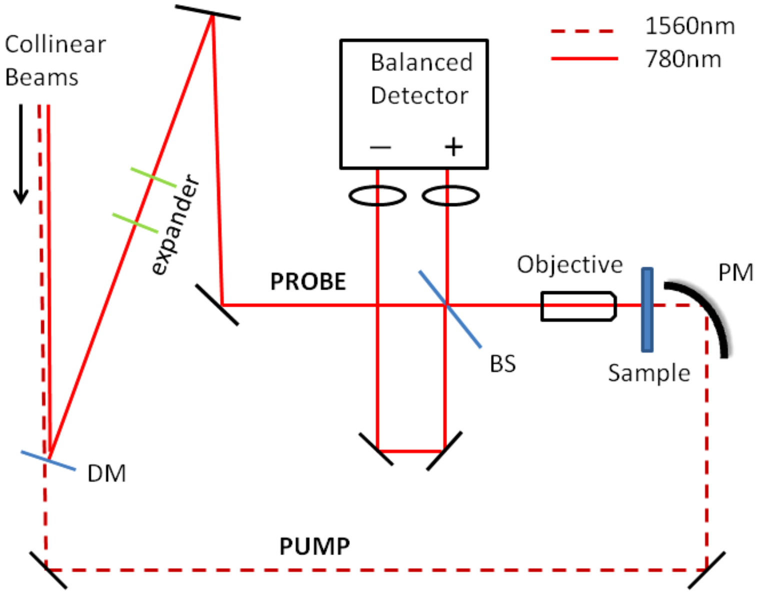

Figure 2-9. Schematic of the front-pump/back-probe transient thermoreflectance setup. DM is a dichroic mirror, BS is the beam splitter and PM is a parabolic mirror.

Figure 2-10 shows an example of a thermoreflectance curve obtained on a 100 nm-Ni/30 nm-Al/80 nm-Sb_2Te_3/sapphire sample. The large-amplitude oscillations in the first few hundreds of picoseconds are the acoustic strain pulses excited at the Al/Sb_2Te_3 interface and detected at the Sb_2Te_3/sapphire interface. Starting at around 1.5 ns, the heat deposited by the transducer arrives at the Sb_2Te_3/sapphire interface, and the temperature increase at this interface is represented by a positive slope over the range of a few nanoseconds. As the heat flows from the Al/Sb_2Te_3 interface to the Sb_2Te_3/sapphire interface, the temperature gradient inside the film continues to decrease. The thermal peak at around 4.5 ns corresponds to the time when the cooling process through the substrate starts to dominate the temperature change at the Sb_2Te_3/sapphire interface. This results in a monotonic decrease of the interface temperature, represented by a decay in the reflectivity change. The fast oscillations at around 4.5 ns correspond to the acoustic strain pulse generated at the Al/Sb_2Te_3 interface by a previous pump pulse, reflected at the back of the substrate, and detected at the Sb_2Te_3/substrate interface. Its location in time depends on the substrate thickness.

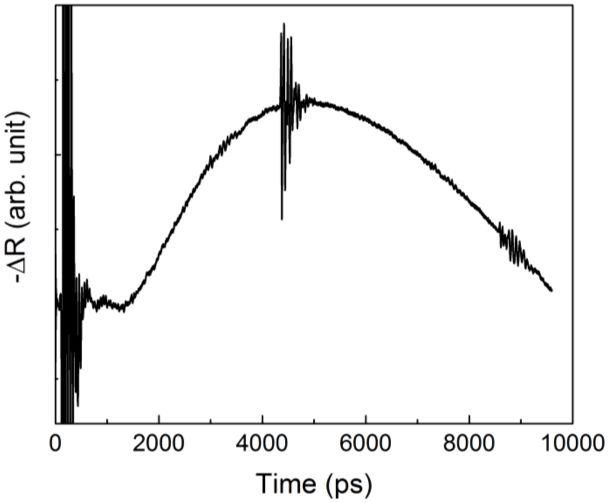

Figure 2-10. Transient thermoreflectance curve with the front-pump/back-probe configuration.

Instead of fitting the curve with Eqns. (2.39) - (2.42), the thermal transport property of the film can be acquired by measuring the temporal position of the thermal peak in Fig. 2-10. This is similar to the Laser Flash Method, where a laser pulse heats one side of the sample, and the temperature change of the other side of the sample is monitored [2.37]. This method is most convenient for bulk samples with millimeter-range thickness, while the pump-probe thermoreflectance technique can investigate thin film samples down to hundred-nanometer-range thickness, depending on the penetration depth of the probe in the sample. In both cases, the thermal diffusivity D of the sample to be measured is related to the half-rise time of the positive slope $t_{1/2}$. For the Laser Flash Method, the relationship is:

$$D = 1.37L^2/\pi^2 t_{1/2} \tag{2.43}$$

where L is the film thickness. Given the same film thickness and the same cooling condition through the back side of the film sample, earlier arrival of the thermal peak signals a larger thermal diffusivity. In addition, the half-rise time of the peak also scales with the square of the film thickness. Figure 2-11 and 2-13 show the thermoreflectance measurements done on a wedge-geometry Sb_2Te_3 thin film with a thickness step-variation from 36 nm to 144 nm. The acoustic strain pulses in the first 500 ps (Fig. 2-11) were used to determine the film thickness according to the acoustic echo round-trip calculation discussed in the previous section. An example of the linear relationship between the temporal position of the "dip" in the first echo and the corresponding film thickness is shown in Figure 2-12, with the slope (≈ 2.8 km/s) corresponding to the sound velocity in Sb_2Te_3.

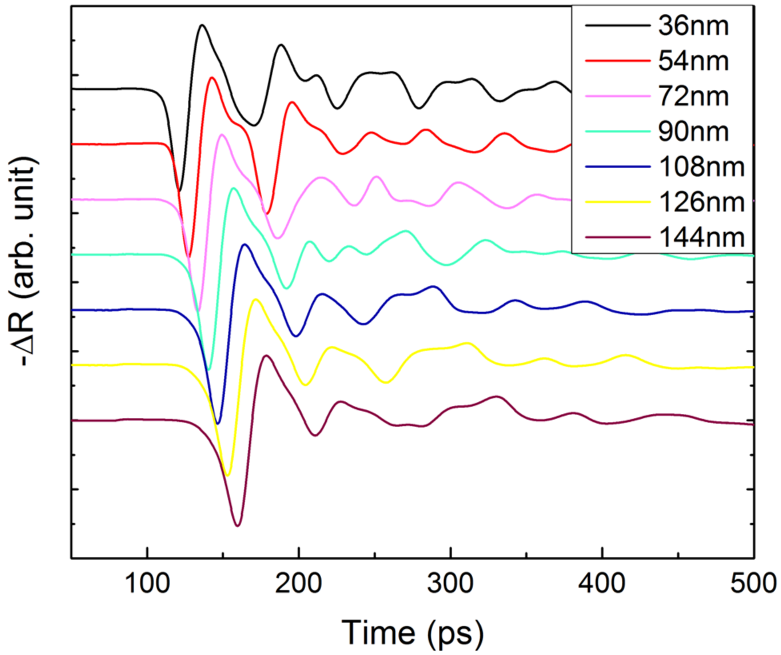

Figure 2-11. The acoustic echoes in the first 500 ps of the front-pump/back-probe thermoreflectance on a wedge Sb_2Te_3 film.

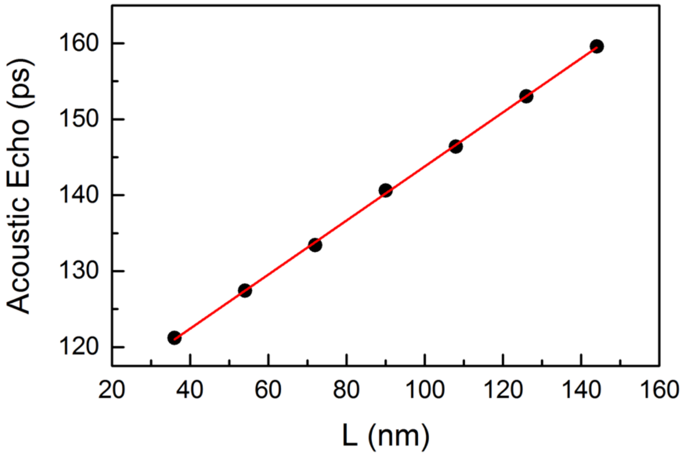

Figure 2-12. The temporal position of the "dip" (at ~ 150 ps in Fig. 2-11) in the first acoustic echo vs. the film thickness *L*. The red line is a linear fit to the data (black dots).

Figure 2-13 shows the thermoreflectance curve over 10 ns. An evident observation is the decrease in the thermal peak amplitude as the film thickness increases. This is not surprising, since the temperature rise at the film/substrate interface is expected to be lower if the same amount of laser energy is distributed in a thicker film, assuming a constant heat capacity. The general trend of the thermal peak position is consistent with Eqn. (2.43), with early arrival times corresponding to thinner films. The half-rise time $t_{1/2}$ is plotted against the square of the film thickness L^2 in Figure 2-14 to test the applicability of Eqn. (2.43) in the Sb_2Te_3 thin film case. For film thicknesses between 72 nm and 144 nm, a linear relationship could be observed, consistent with the prediction of Eqn. (2.43). The slope value extracted from the best-fit line, combined with Eqn. (2.43), yields a thermal diffusivity of 1.2×10^{-6} m^2/s along the c-axis of Sb_2Te_3, agreeing well with the literature value [2.20]. The non-zero intercept in Fig. 2-14 possibly results from the presence of the transducer, whose slow temperature decrease considerably delays the arrival of the thermal peak. For a thickness below 72 nm, however, noticeable deviations from the linear relationship could be observed. This could be due to the large penetration depth of the probe laser (~ 60 nm at $\lambda = 780$ nm) in Sb_2Te_3 relative to the film thickness. As a result, the signals from within the film and even the transducer/film interface contribute substantially to the overall signal detected by the probe, and the thick-sample approximation in Eqn. (2.43) no longer holds. A reasonable data fitting in this case would require taking into account the probe spatial profile inside the film. Nevertheless, Eqn. (2.43) with an incorporated offset remains a good approximation for films much thicker than 60 nm.

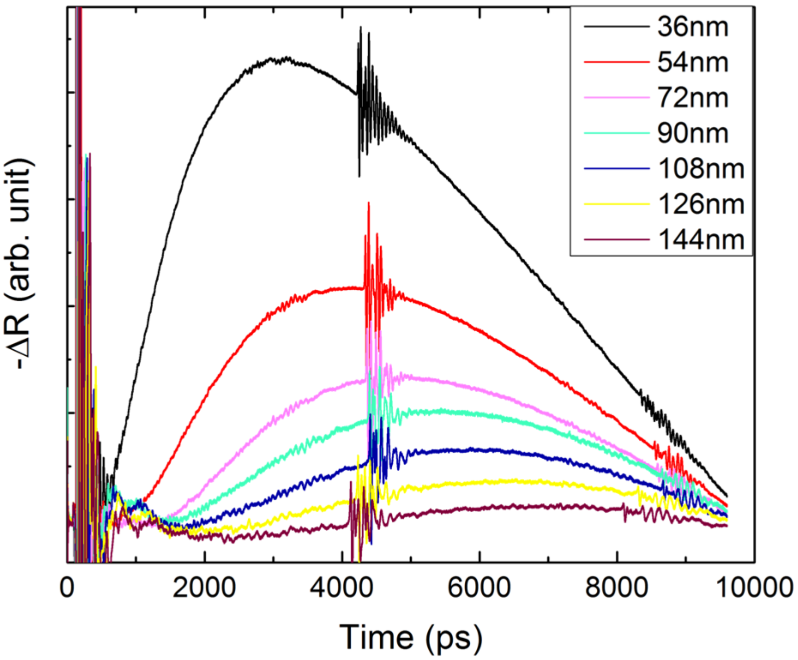

Figure 2-13. Transient thermoreflectance with the front-pump/back-probe configuration over 10 ns on an Sb_2Te_3 film with a thickness variation.

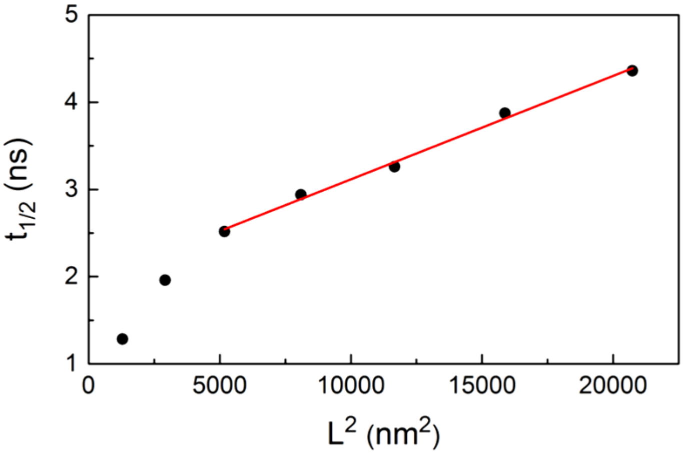

Figure 2-14. The half-rise time $t_{1/2}$ measured from Fig. 2-13 versus the film thickness squared L^2 for the seven thicknesses from 36 nm to 144 nm.

Leakage of hot carriers from the transducer into the film can greatly distort the thermoreflectance curve and even overwhelm the relatively weak thermal peak. This requires the transducer material to have a strong carrier-phonon coupling and a reasonable thickness for leakage suppression. In addition, a good acoustic impedance matching between the transducer and the film ensures a small thermal boundary resistance and higher heat transfer efficiency. Finally, excellent adherence of the transducer to the film is required for a good-quality interface. While no single metal ranks best in all three categories for Sb_2Te_3 films, several metals, including Al, Ni, and Ti, are good candidates that meet the criteria well.

Figure 2-15 illustrates the effect of carrier leakage on the thermoreflectance curve. Two kinds of metal transducers were used: 120 nm-Ni/Sb_2Te_3 (blue curve) and 75 nm-Al/15 nm-Ti/Sb_2Te_3 (red curve). The curve that corresponds to the more severe carrier leaking, shown with the larger peak amplitude near 100 ps, complicates the thermal transport signal with carrier relaxation processes.

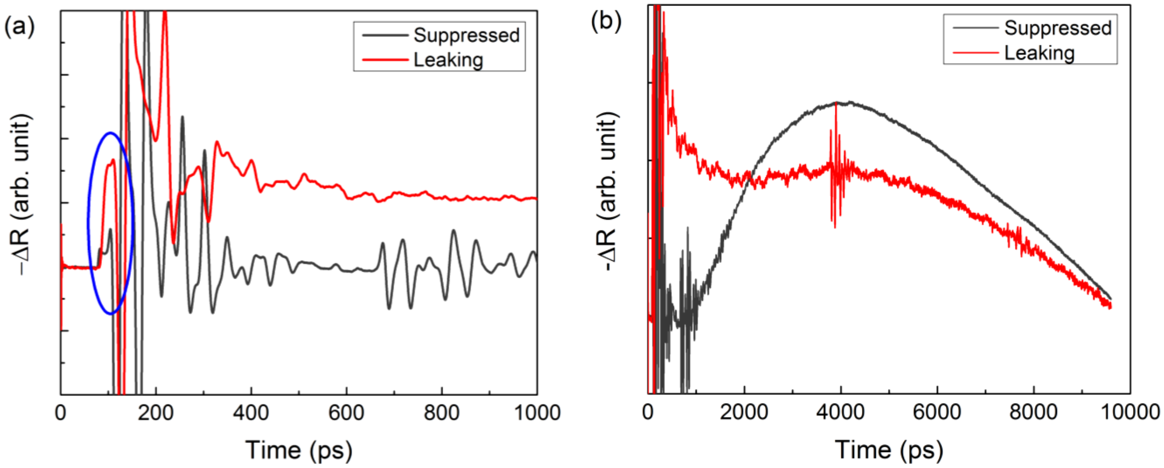

Figure 2-15. Effect of carrier-leakage on the thermoreflectance curve. (a) and (b) have the same curves on different time scales. The carrier-suppressed curve has a clean thermal peak, while the carrier-leaking curve is greatly distorted by the carrier relaxation. The circled region in (a) indicates the arrival of hot carriers from the interface.

References

[2.1] P. A. Elzinga, F. E. Lytle, Y. Jian, G. B. King, and N. M. Laurendeau, "Pump/probe spectroscopy by asynchronous optical sampling", *Appl. Spectroscopy* **41**, 2 (1987)

[2.2] T. Dekorsy, F. Hudert, R. Cerna, H. Schäfer, C. Janke, a. Bartels, K. Köhler, S. Braun, M. Wiemer, and S. Mantl, "Coherent acoustic phonons in nanostructures investigated by asynchronous optical sampling", *Proc. of SPIE* **6393**, 63930H (2006)

[2.3] A. Bartels, R. Cerna, C. Kistner, A. Thoma, F. Hudert, C. Janke, and T. Dekorsy, "Ultrafast time-domain spectroscopy based on high-speed asynchronous optical sampling", *Rev. Sci. Instrum*. **78**, 035107 (2007)

[2.4] V. A. Stoica, Y. Sheu, D. A. Reis, and R. Clarke, "Wideband detection of transient solid-state dynamics using ultrafast fiber lasers and asynchronous optical sampling", *Opt. Express* **16**, 2322 (2008)

[2.5] Menlo Systems GmbH Operation Manual

[2.6] G. Eckhardt, R. W. Hellwarth, F. J. McClung, S. E. Schwarz, D. Weiner, and E. J. Woodbury, "Stimulated Raman scattering from organic liquids", *Phys. Rev. Lett.* **9**, 455 (1962)

[2.7] R. F. Begley, A. B. Harvey, and R. L. Byer, "Coherent anti-Stokes Raman spectroscopy", *Appl. Phys. Lett.* **25**, 387 (1974)

[2.8] Y. Yan, E. B. Gamble Jr., and K. A. Nelson, "Impulsive stimulated scattering: General importance in femtosecond laser pulse interactions with matter, and spectroscopic applications", *J. Chem. Phys.* **83**, 5391 (1985)

[2.9] Y. Yan and K. A. Nelson, "Impulsive stimulated light scattering. I. General theory", *J. Chem. Phys.* **87**, 6240 (1987)

[2.10] R. Merlin, "Generating coherent THz phonons with light pulses", *Solid State Commun*. **102**, 207 (1997)

[2.11] T. K. Cheng, J. Vidal, H. J. Zeiger, G. Dresselhaus, M. S. Dresselhaus, and E. P. Ippen, "Mechanism for displacive excitation of coherent phonons in Sb, Bi, Te, and Ti_2O_3", *Appl. Phys. Lett*. **59**, 1923 (1991)

[2.12] H. J. Zeiger, J. Vidal, T. K. Cheng, E. P. Ippen, G. Dresselhaus, and M. S. Dresselhaus, "Theory for displacive excitation of coherent phonons", *Phys. Rev. B* **45**, 768 (1992)

[2.13] G. A. Garrett, T. F. Albrecht, J. F. Whitaker, and R. Merlin, "Coherent THz phonons driven by light pulses and the Sb problem: What is the mechanism?", *Phys. Rev. Lett*. **77**, 3661 (1996)

[2.14] T. Dekorsy, H. Auer, C. Waschke, H. J. Bakker, H. G. Roskos, and H. Kurz, "Emission of submillimeter electromagnetic waves by coherent phonons", *Phys. Rev. Lett.* **74**, 738 (1996)

[2.15] T. E. Stevens, J. Kuhl, and R. Merlin, "Coherent phonon generation and the two stimulated Raman tensors", *Phys. Rev. B* **65**, 144304 (2002)

[2.16] R. W. Boyd, *Nonlinear Optics.* Academic Press, third edition (2008)

[2.17] O. B. Wright, "Thickness and sound velocity measurement in thin transparent films with laser picosecond acoustics", *J. Appl. Phys*. **71**, 1617 (1992)

[2.18] G. Tas, R. J. Stoner, H. J. Maris, G. W. Rubloff, G. S. Oehrlein, and J. M. Halbout, "Noninvasive picosecond ultrasonic detection of ultrathin interfacial layers: CF_x at the Al/Si interface", *Appl. Phys. Lett*. **61** 1787 (1992)

[2.19] C. Thomsen, H. T. Grahn, H. J. Maris, and J. Tauc, "Surface generation and detection of phonons by picosecond light pulses", *Phys. Rev. B* **34**, 4129 (1986)

[2.20] D. M. Rowe, ed. *Thermoelectrics Handbook*. CRC Press (2006)

[2.21] J. S. Dyck, W. Chen, C. Uher, Č. Drašar, and P. Lošt'ák, "Heat transport in $Sb_{2-x}V_xTe_3$ single crystals", *Phys. Rev. B* **66**, 125206 (2002)

[2.22] W. Richter, A. Krost, U. Nowak, and E. Anastassakis, "Anisotropy and dispersion of coupled plasmon-LO-phonon modes in Sb_2Te_3", *Z. Phys. B - Condensed Matter* **49**, 191 (1982)

[2.23] R. H. M. Groeneveld, R. Sprik, and A. Lagendijk, "Femtosecond spectroscopy of electron-electron and electron-phonon energy relaxation in Ag and Au", *Phys. Rev. B* **51**, 11433 (1995)

[2.24] G. Tas and H. J. Maris, "Electron diffusion in metals studied by picosecond ultrasonics", *Phys. Rev. B* **49** 15046 (1994)

[2.25] G. L. Eesley, "Observation of nonequilibrium electron heating in copper", *Phys. Rev. Lett.* **51**, 2140 (1983)

[2.26] R. W. Schoenlein, W. Z. Lin, J. G. Fujimoto, and G. L. Eesley, "Femtosecond studies of nonequilibrium electronic processes in metals", *Phys. Rev. Lett.* **58**, 1680 (1987)

[2.27] S. D. Brorson, J. G. Fujimoto, and E. P. Ippen, "Femtosecond electronic heat-transport dynamics in thin gold films", *Phys. Rev. Lett.* **59**, 1962 (1987)

[2.28] H. E. Elsayed-Ali, T. B. Norris, M. A. Pessot, and G. A. Mourou, "Time-resolved observation of electron-phonon relaxation in copper", *Phys. Rev. Lett*. **58**, 1212 (1987)

[2.29] S. I. Anisimov, B. L. Kapeliovich, and T. L. Perel'man, "Electron emission from metal surfaces exposed to ultrashort laser pulses", *Sov. Phys. -JETP* **39**, 375 (1974)

[2.30] T. Q. Qiu, C. L. Tien, "Heat transfer mechanisms during short-pulse laser heating of metals", *J. Heat Transfer* **115** 835 (1993)

[2.31] S. D. Brorson, A. Kazeroonian, J. S. Moodera, D. W. Face, T. K. Cheng, E. P. Ippen, M. S. Dresselhaus, and G. Dresselhaus, "Femtosecond room-temperature measurement of the electron-phonon coupling constant λ in metallic superconductors", *Phys. Rev. Lett.* **64**, 2172 (1990)

[2.32] C. A. Paddock and G. L. Eesley, "Transient thermoreflectance from thin metal films", *J. Appl. Phys.* **60**, 285 (1986)

[2.33] R. J. Stoner and H. J. Maris, "Kapitza conductance and heat flow between solids at temperatures from 50 to 300K", *Phys. Rev. B* **48**, 16373 (1993)

[2.34] G. A. Antonelli, B. Perrin, B. C. Daly, and D. G. Cahill, "Characterization of mechanical and thermal properties using ultrafast optical metrology", *MRS Bulletin* **31**, 607 (2006)

[2.35] R. I. Hickson, S. I. Barry, G. N. Mercer, and H. S. Sidhu, "Finite difference schemes for multilayer diffusion", *Math. Comput. Model.* **54**, 210 (2011)

[2.36] V. A. Stoica, Ph.D. Dissertation, University of Michigan (2010)

[2.37] W. J. Parker, R. J. Jenkins, C. P. Butler, and G. L. Abbott, "Flash method of determining thermal diffusivity, heat capacity, and thermal conductivity*", J. Appl. Phys.* **32**, 1679 (1961)

Chapter 3

Coherent Optical Phonon Spectroscopy Studies of Femtosecond-Laser Modified Sb_2Te_3 Films

Previously we have introduced fs laser pump-probe techniques used to monitor material dynamics over a wide range of time scales. Among them, coherent optical phonon spectroscopy has been proven extremely helpful in real-time material characterization and was commonly applied to the studies of the technologically important Te-based chacolgenides. These include the popular phase-change material $Ge_2Te_2Sb_5$ (GST) for optical recording, as well as the binary compounds Sb_2Te_3 and Bi_2Te_3 for thermoelectric applications and topological insulators [3.1-3.8]. For example, coherent optical phonon spectra were used to identify the three phases of GST as it underwent temperature variations or laser treatments [3.1-3.3]. The vacancies in the GeTe/Sb_2Te_3 superlattice have been investigated with the help of the dephasing dynamics of the optical phonons [3.4]. Similar studies have also been performed to examine the second harmonics of coherent phonons on Bi_2Te_3 [3.5] and the amorphous-to-crystalline transition of Sb_2Te_3 films [3.6]. In addition, coherent phonons have been employed to evaluate the interface phonon scattering in Bi_2Te_3/Sb_2Te_3 superlattices [3.7] and the thermal properties of GST [3.8]. In these studies, the assignment of the observed coherent optical phonon peaks can be challenging, due to the difficulties with the detections of the asymmetric coherent optical phonon modes in the isotropic reflectivity measurements as discussed in Chapter 2.

The work in this chapter employs complementary techniques of isotropic and anisotropic transient reflectivity measurements and cw Raman spectroscopy. The measurements are performed on Sb_2Te_3 thin films and a coherent phonon peak is observed to appear around 3.6-3.7 THz that appears after fs laser irradiation [3.9]. The experimental results indicate a Te phase segregation from Sb_2Te_3 due to exposure to the fs laser above a certain fluence threshold, drawing attention to the need for careful interpretation of the results obtained from coherent phonon spectroscopy in Te-based materials. Section 3.1 will discuss results from the isotropic and anisotropic transient reflectivity experiments on coherent phonons in Sb_2Te_3 thin films. These complementary experiments cover the symmetric and asymmetric Raman modes of Sb_2Te_3, and clarify that the new phonon peak appears after laser irradiation, corresponding to a new Te phase other than Sb_2Te_3. Section 3.2 will present additional evidence from cw Raman spectroscopy on fs laser-irradiated Sb_2Te_3 to assist in the assignment of the new phonon peak. Finally, section 3.3 will show results on the irradiation laser fluence dependence of the amplitudes of the two phonon modes. The main results from this chapter were published in [3.9].

3.1 Experiments on Coherent Optical Phonons

As was briefly discussed in Chapter 1, Sb_2Te_3 is composed of quintets of alternating Sb and Te layers. The quintets are separated by van der Waals gaps while the layers within each quintet are connected by covalent bonds. When considering the optical phonon normal modes, the atoms inside each quintet can be approximated by a linear-chain model [3.10], composed of Sb and Te along the c-axis in the following order: Te^1 - Sb - Te^2 - Sb - Te^1.

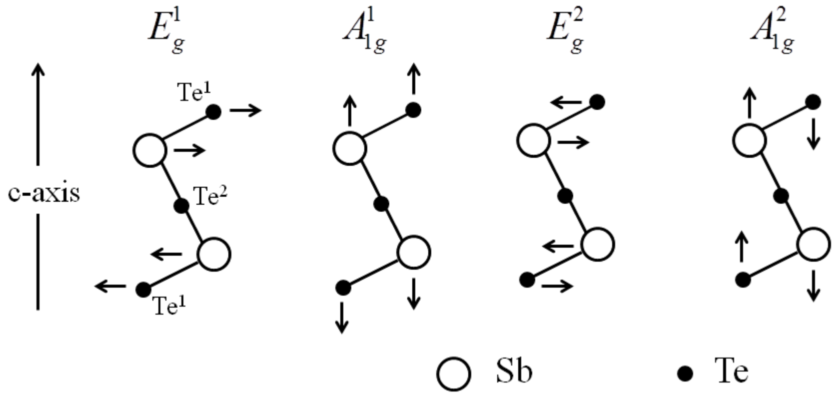

Figure 3-1. The Raman-active modes for Sb_2Te_3. The large open circles represent the Sb atoms, while the small solid circles correspond to the two species of Te atoms: Te^2 at the center and Te^1 at the two ends. Since Sb_2Te_3 is centrosymmetric, the Raman-active modes and the infrared-active modes are mutually exclusive.

This arrangement gives four Raman-active modes for Sb_2Te_3: two A_{1g} modes (singlets) and two E_g modes (doubly degenerate) [3.10, 3.11]. The A_{1g} modes have oscillations along the c-axis that preserve the overall symmetry of the cell, while the E_g modes (shear modes) have oscillations perpendicular to the c-axis. Their Raman tensors are represented by Eqns. (3.1) and (3.2) [3.10, 3.11]. $E_g(x)$ and $E_g(y)$ are the two degenerate modes perpendicular to the c- axis (z-direction). The tensor elements a, b, c, and d for the four Raman-active modes can be calculated from density functional theory [3.11]. Among these four modes, two of them fall into the detection range of coherent phonon experiments in this dissertation: A_{1g} at ~2.1 THz, and E_g at ~ 3.6 THz [3.10]. Since the pump photon energy (~0.8 eV) is much larger than the bandgap of Sb_2Te_3 (~0.3 eV) [3.12, 3.13], the A_{1g} mode will dominate the observed coherent phonon spectrum. However, as we will see later in this section, Eqns. (3.1) and (3.2) suggest that by analyzing the reflected probe's polarization, the strong A_{1g} mode can be suppressed to bring out the weak E_g mode.

$$A_{1g} = \begin{bmatrix} a & 0 & 0 \\ 0 & a & 0 \\ 0 & 0 & b \end{bmatrix} \tag{3.1}$$

$$E_g(x) = \begin{bmatrix} c & 0 & 0 \\ 0 & -c & d \\ 0 & d & 0 \end{bmatrix} \qquad E_g(y) = \begin{bmatrix} 0 & -c & -d \\ -c & 0 & 0 \\ -d & 0 & 0 \end{bmatrix} \tag{3.2}$$

The sample used for the measurements was an epitaxial Sb_2Te_3 thin film of 100 nm grown by the Uher research group using molecular beam epitaxy (MBE) [3.9]. The film was on a sapphire (Al_2O_3) substrate with both their c-axes (film and substrate) perpendicular to the surface. Reflection high energy electron diffraction (RHEED) and X-ray diffraction (XRD) were used to confirm the high single-crystalline quality of the film.

The ASOPS pump-probe setup used for coherent phonon spectroscopy was described in Chapter 2. The master laser serves as the pump ($\lambda = 1560$ nm), and the frequency-doubled slave laser serves as the probe ($\lambda = 780$ nm). The pump fluence was controlled by a half-wave plate followed by a polarizer, and could be increased up to 6.72 mJ/cm^2, while the probe fluence was fixed at ~0.2 mJ/cm^2.

The focal spot sizes of the pump and probe beams were measured using the knife-edge method, where a razor blade sweeps across the focused beam spot perpendicular to the beam propagation direction and the unblocked beam power is measured by a photodetector as a function of the blade position [3.14]. This method takes advantage of the Gaussian profile of the laser beam cross-section: $I(x,y) = I_0 \exp\left(-\beta_x^2(x-x_0)^2 - \beta_y^2(y-y_0)^2\right)$, where (x_0, y_0) is the position of the beam center. In this case the unblocked beam power received by the detector is the integral of the Gaussian profile from $-\infty$ to the blade position x_b [3.14]:

$$R(x_b) = I_0(\pi/\beta_y^2)^{1/2} \int_{-\infty}^{x_b} \exp\left(-\beta_x^2(x-x_0)^2\right) dx \tag{3.3}$$

for a blade sweeping in the x-direction. The integral results in a shifted negative error function, and fitting can be performed on the experimental data to obtain β_x. Based on Eqn. (3.3), a shorthand formula can be used to quickly calculate the 1/e beam waist radius [3.14]:

$$\beta^{-1} \approx 0.552(x_{10} - x_{90}) \tag{3.4}$$

where x_{10} and x_{90} are the blade positions that correspond to 10% and 90% of the total beam power being unblocked by the blade. Using Eqn. (3.4), the pump and the probe's focused beam diameters after the parabolic focusing mirror are 3.2 μm and 1.6 μm, respectively.

To obtain the coherent phonon spectra, Δf of the two lasers was kept around 200 Hz to optimize the time resolution while maintaining a reasonably fast data acquisition rate. The bandwidth of the detector (Thorlabs PDB 145A) is up to 15 MHz. Taking into account the pulse widths and the jitter of the pump and the probe, the temporal resolution is 200 fs. A CCD camera was used to monitor the laser spot on the sample. Once the sample was roughly in place, its position was fine-tuned to maximize the initial peak of the electronic excitation. This ensured that the sample surface overlapped with the focal position of the parabolic mirror.

The sample was exposed to a range of pump-laser fluences for different intervals so that the effect of laser irradiation on the coherent optical phonon spectra of Sb_2Te_3 could be studied. The spectra before and after pump laser irradiation were taken with a low pump-pulse fluence of 0.34 mJ/cm^2. Preliminary measurements have shown that such a fluence did not cause any change in the phonon spectrum in 2 minutes, a typical time to complete one measurement. Each set of measurements (before and after irradiation) was taken on a fresh spot on the sample.

Figure 3-2 shows an example of coherent optical phonon spectra before and after the pump laser irradiation with a fluence of 4.26 mJ/cm^2. The rapid oscillation of the coherent phonon dynamics was superimposed on a background of carrier excitation and lattice heating. After the slowly-varying background was subtracted, fast Fourier transform analysis (FFT) was performed on the fast oscillations to obtain the coherent optical phonon spectra. The exact peak locations were acquired by Lorenzian fitting to the spectra data.

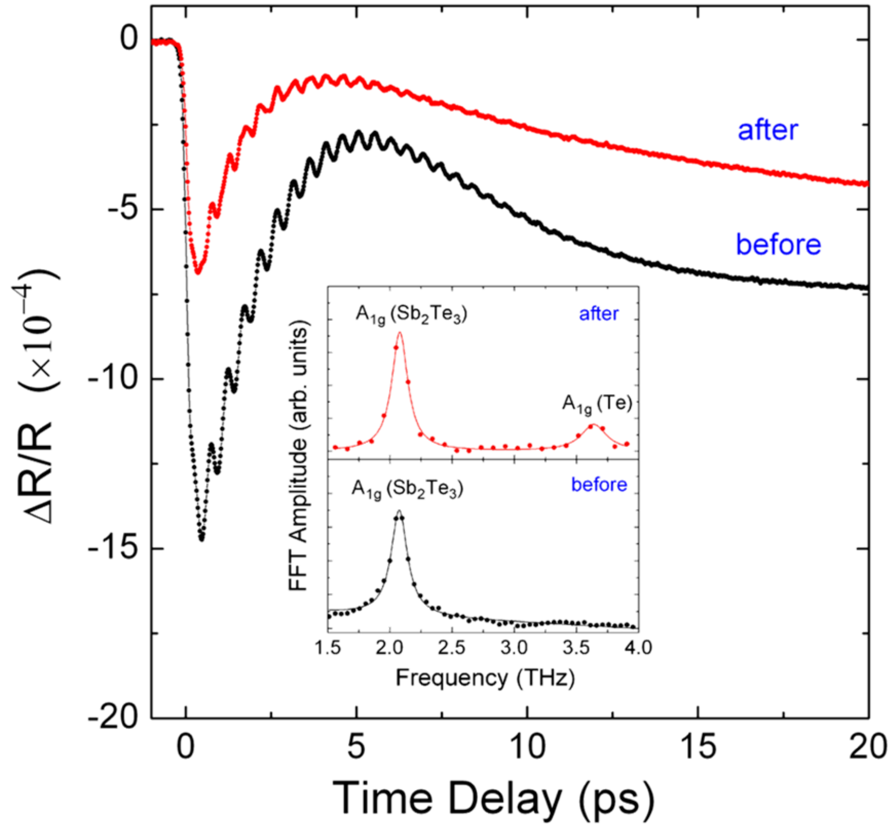

Figure 3-2. Time-resolved reflectivity change on an Sb_2Te_3 thin film before and after irradiation by the pump laser with a fluence of 4.26 mJ/cm^2. The inset shows the coherent optical phonon spectra after FFT was performed on the rapidly-oscillating coherent phonon dynamics in the time-resolved trace. The lines in the inset are the Lorenzian fits to the FFT data (dots) to determine peak locations. Note that a new peak around 3.64 THz appeared after the pump laser irradiance, which we assigned to the A_{1g} mode of Te.

In both curves (before and after), a peak at 2.07 THz appeared, which we attributed to the A_{1g} mode of Sb_2Te_3 by comparison with cw Raman spectroscopy [3.10]. Interestingly, the new peak around 3.64 THz showed up only after the high-fluence pump laser irradiation, which, as noted above, we assigned to the A_{1g} mode of Te [3.15]. It is also worth noting that coherent phonon peaks near 3.64 THz have been observed before in several studies of Te-based chalcogenides. For instance, a weak coherent phonon peak at 3.68 THz was reported in Bi_2Te_3 and attributed to the second harmonic of the A_{1g} mode of Bi_2Te_3 at 1.84 THz [3.5]. This clearly does not apply to our case of Sb_2Te_3 at 2.07 THz. Another study on Sb_2Te_3 observed a coherent phonon peak at 3.6 THz, which the authors attributed to the E_g mode of Sb_2Te_3 [3.1]. To address this possibility, we performed anisotropic reflectivity measurements [3.16-3.19] on the irradiated and non-irradiated Sb_2Te_3 samples to compare the E_g mode of Sb_2Te_3 and the new peak.

In the anisotropic reflectivity configuration, the incident probe was at a 45^o relative to the optical plane, and the reflected probe signal from the sample was split by a polarizing beamsplitter into two orthogonal components: ΔR_p in the optical plane of the setup and ΔR_s perpendicular to the optical plane. These two components were then sent to the two input ports of a balanced detector, and the difference $\Delta R_p - \Delta R_s$ was measured as a function of time delay. Since the c-axis is perpendicular to the film surface, the probe polarization is in the x-y plane perpendicular to the c-axis. The isotropic A_{1g} excitation yields the same ΔR_p and ΔR_s in the x-y plane. Therefore, the reflected probe difference is zero for the A_{1g} mode. The anisotropic E_g excitation, however, contributes to ΔR_p and ΔR_s differently [3.16-3.19]. Thus, the weak E_g mode can be detected with the suppression of the strong A_{1g} mode by analyzing the reflected probe's polarization.

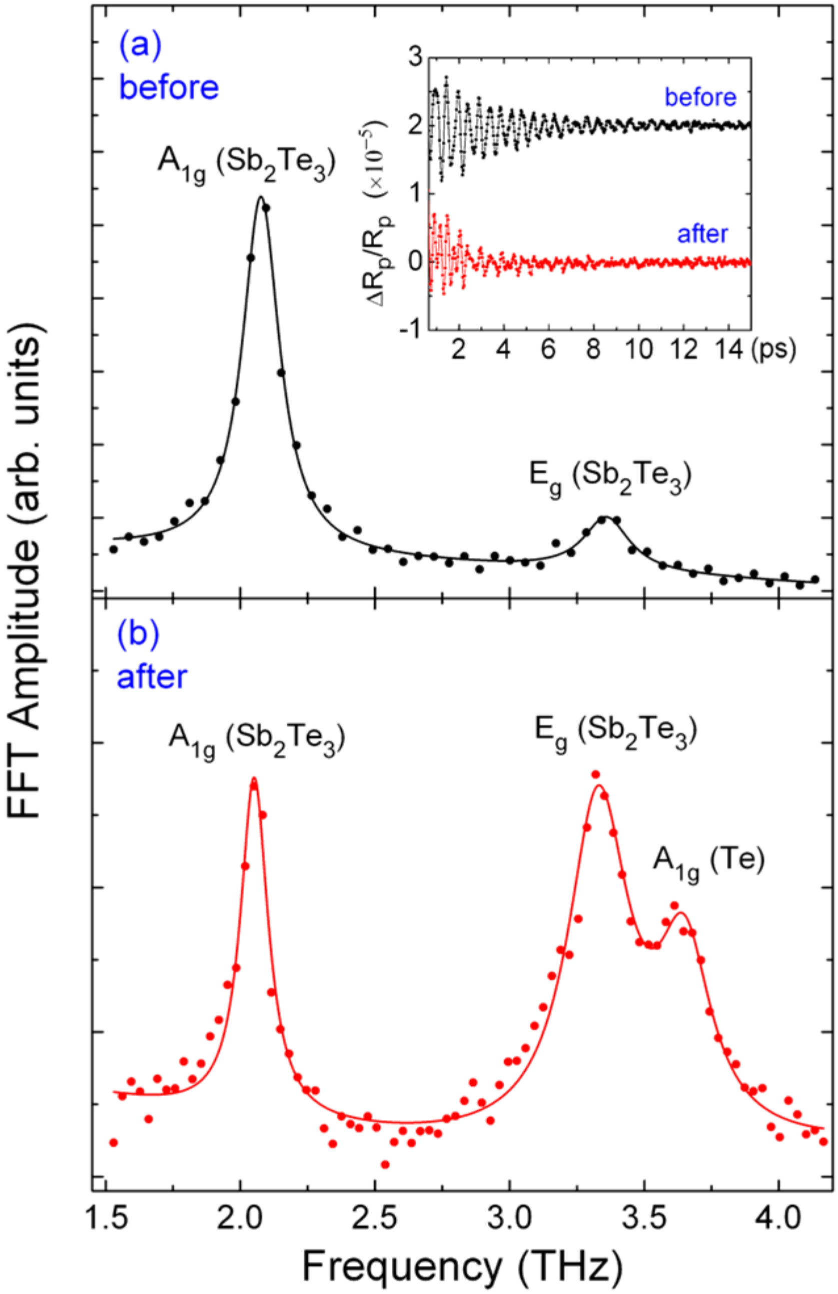

Figure 3-3. FFT of the anisotropic reflectivity measurement results on the Sb_2Te_3 thin film (a) before and (b) after the pump laser irradiation with a fluence of 5.6 mJ/cm^2 for 1 second. Again, Lorenzian fitting (lines) to the data (dots) was performed to locate the peak positions. The relatively weak E_g mode at 3.36 THz showed up with the suppression of the A_{1g} mode. The new peak at 3.64 THz is therefore clearly distinguishable from the E_g mode of Sb_2Te_3. The change of the relative amplitudes of A_{1g} and E_g modes compared to before irradiation may be attributed to the change of the film's surface roughness after irradiation. The inset shows the time-resolved anisotropic reflectivity curves from which the FFT spectra were computed.

Figure 3-3 shows the anisotropic reflectivity result on the Sb_2Te_3 film before and after irradiation by a pump laser fluence of 5.6 mJ/cm^2 for 1 second. Before the irradiation, two peaks at 2.07 THz and 3.36 THz are observed, consistent with the A_{1g} mode and E_g mode of Sb_2Te_3 [3.10]. After the irradiation, on the other hand, a third peak at 3.64 THz is clearly visible and distinguishable from the E_g mode of Sb_2Te_3. The isotropic and anisotropic reflectivity measurement results from Figs. 3-2 and 3-3 indicate that the new laser-induced peak at 3.64 THz is not a coherent phonon mode of Sb_2Te_3.

It is worth pointing out that one of the phases identified in the fs laser-induced nanostructures (see Chapter 4) in Sb_2Te_3 thin films corresponds to the cubic Sb_2O_3 (senarmontite), which has a weak E_g Raman mode close to 3.64 THz [3.20, 3.21]. However, comparison between the inset of Fig. 3-1 and Fig. 3-2 (b) suggests that the 3.64 THz peak is mainly of an A_{1g} symmetry due to its significant suppression in the anisotropic reflectivity configuration. Therefore, the assignment of this new peak still favors Te over cubic Sb_2O_3.

3.2 Micro-Raman Studies

To further confirm the appearance of Te after high-fluence pump laser irradiation on Sb_2Te_3, additional micro-Raman studies were carried out. In these investigations, a Renishaw inVia Raman microscope was used. A continuous wave (cw) laser beam with a wavelength of 514 nm was focused by a 50 × objective to a spot size of 20 μm on the sample surface. The data collection integration time can be varied from 10 seconds to 60 seconds, and the maximum laser power is 1.5 mW. The long-pass color filter for the detector cuts off at around 120 cm^{-1}. However, peaks near this cutoff line, such as the ones at 124 cm^{-1} in Figure 3-4, likely have a lower intensity than their actual value due to the filter.

Micro-Raman spectra on three different areas are shown in Figure 3-4: a fresh region on the Sb_2Te_3 film, without prior irradiation by the fs laser; a region on the same film irradiated by the fs laser; and a region on a polycrystalline tellurium film freshly grown by MBE.

For the fresh region on the Sb_2Te_3 film, a cw laser power of 1.5 mW was used for during the Raman measurement with an integration time of 30 seconds. To exclude any cw laser-induced effects on this fresh spot without any prior irradiation from the fs laser, repeated micro-Raman measurements were done on this location, each with the same cw laser power and integration time. No perceivable change was found in the consecutive Raman spectra in this particular location. This indicates that the Raman spectrum labeled "non-irradiated Sb_2Te_3" in Figure 3-4 is representative of a fresh spot on the Sb_2Te_3 film. For an integration time longer than 60 seconds, however, a considerable variation could be noticed in the spectrum. In this "non-irradiated" Sb_2Te_3 region, a peak at around 166 cm^{-1} could be seen, corresponding to the A_{1g}^2 mode of Sb_2Te_3 [3.10, 3.11]. Moreover, a small shoulder appeared between 140 cm^{-1} and 150 cm^{-1}, coinciding with the E_g mode of Te [3.15]. This small trace of Te could be due to the slight off-stoichiometry in the fresh Sb_2Te_3 thin film sample.

The middle panel in Figure 3-4 shows the Raman spectrum of the fs laser irradiated region on the same film. Three significant peaks could be observed: 124 cm^{-1}, 140 cm^{-1} and 255 cm^{-1}. The first two peaks overlap perfectly with the A_{1g} and E_g modes of Te, both from literature and by comparison with the Te Raman spectrum in the bottom panel of the same figure. Note that the 124 cm^{-1} peak, which corresponds to the coherent optical phonon mode of ~ 3.64 THz in section 3.1 , also overlaps with the E_g mode of the cubic Sb_2O_3 as previously discussed. In this case, since the excitation laser is unpolarized and no analyzer was used for detection, the symmetry of the 124 cm^{-1} peak cannot be determined. Therefore, the cubic Sb_2O_3 E_g mode remains a possible contribution to this Raman peak, in addition to the A_{1g} mode of Te. For the 255 cm^{-1} peak, however, no Te Raman mode can be responsible. The one strong candidate for this peak, taking into account the evidence so far, is the A_{1g} mode of cubic Sb_2O_3 [3.21]. This peak is adjacent to a shoulder coinciding with the second-order Raman peak of Te at ~ 270 cm^{-1} [3.22], also seen in the Te film spectrum in the bottom panel. Another trace of the second-order Te peak can be seen around 223 cm^{-1} [3.22] in both the irradiated Sb_2Te_3 spectrum and the Te film spectrum. On the other hand, the 166 cm^{-1} peak seen in the non-irradiated Sb_2Te_3 region has diminished considerably after irradiation, suggesting a fs laser-induced Sb_2Te_3 decomposition.

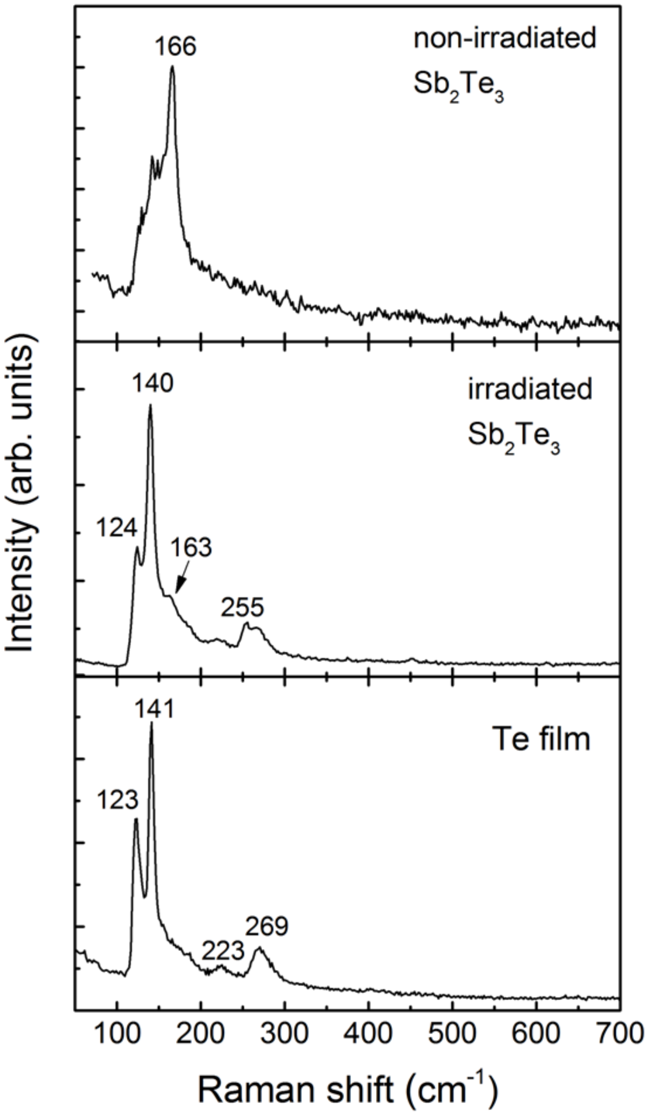

Figure 3-4. Micro-Raman spectrum of a fs laser-irradiated region on the Sb_2Te_3 thin film with a fluence of ~ 4 mJ/cm^2 (middle panel), compared with that of the non-irradiated region on the same film (top panel) and a polycrystalline Te film (bottom panel) as references.

Interestingly, although a Te phase in the crystalline form has been observed with the micro-Raman spectroscopy, the Sb phase, left over from the decomposed Sb_2Te_3, was never seen in either the coherent optical phonon spectra or the micro-Raman spectra. In particular, Sb has a strong A_{1g} mode at 150 cm^{-1} [3.23] that failed to appear in any micro-Raman spectra on all fs laser-irradiated regions in the Sb_2Te_3 film. While some Sb may combine with the oxygen in air to form Sb_2O_3, the clarification of whether there are Sb atoms remaining on the irradiated region and their locations require additional studies besides the spectroscopy performed in this chapter. A related question will be answered for the fs laser-induced nanostructures in Sb_2Te_3 films in Chapter 4, where the spatial distribution of the Sb element is determined through cross-sectional studies.

Finally, since the fs laser irradiation was performed in air, oxide formation is a likely process. In addition to the Sb_2O_3 already observed, another possible consideration is the formation of TeO_2. Similar to Sb_2O_3, TeO_2 has an E_g mode close to the coherent optical phonon peak at 3.64 THz (122 cm^{-1}) [3.24], but is disfavored due to the same argument. Additionally, it has two A_1 modes at 148 cm^{-1} and 393 cm^{-1}, and five E modes between 150 cm^{-1} and 350 cm^{-1} [3.24], none of which were observed in the micro-Raman spectra. The absence of these major Raman modes suggests that there is a negligible amount of TeO_2 present in the fs laser irradiated regions.

These micro-Raman studies have complemented and supported our assignment of the Te A_{1g} mode to the new coherent optical phonon peak at 3.64 THz after fs laser irradiation. The appearance of the Te phonon peak and a decrease of the Sb_2Te_3 peak suggest a fs laser-induced Sb_2Te_3 decomposition and Te segregation. One of the mechanism in play could be a thermal effect due to laser heating. To estimate the temperature rise ΔT, two contributions were considered: the transient temperature increase, ΔT_t, resulting from the energy disposition from each laser pulse, and the background temperature increase, ΔT_b, resulting from the heat accumulation from previous pulses. The transient temperature increase can be calculated from:

$$\Delta T_t = \frac{FAM}{dC_p\rho} \tag{3.5}$$

where F is the pump laser fluence (4.62 mJ/cm^2), A is the optical absorption in the film (0.4), d is the heat penetration depth (~ 80 nm), C_p is the specific heat of Sb_2Te_3 (130 J/mol/K), ρ is its density (6.5 g/cm^3), and M is its molecular weight (626.32 g/mol). ΔT_b was estimated to be ~ $2\Delta T_t$. With these values, the total temperature rise due to the fs laser irradiation on the Sb_2Te_3 film is $\Delta T = 500 \pm 150\ ^{o}C$. The ΔT uncertainty was estimated from the measurement uncertainties for F , d and A. Such a temperature rise is likely to be even higher near the film surface, due to the exponential decay profile of the laser intensity inside the film. The effect of this large transient temperature rise and the exact mechanism that leads to laser-induced phase transformation and subsequent Te segregation are not well understood with the experimental evidence at hand, and further studies are needed to elucidate the details of this process.

It is worth noting that segregation of Te has been observed by cw Raman spectroscopy in Te-containing compounds such as Te-rich Bi-Te thin films [3.25], CdTe thin films [3.26, 3.27], and $Ge_2Sb_2Te_5$ films [3.28]. Laser-induced segregation of Te has also been shown to accompany cw Raman measurements of ZnTe [3.29], $CuInTe_2$ [3.30], $CdIn_2Te_4$, $ZnIn_2Te_4$, $MnIn_2Te_4$ [3.31], and CdZnTe [3.32, 3.33]. These reports serve as evidence for the susceptibility of Te-based chalcogenides to Te phase separation. The study in this chapter indicates that fs laser irradiation of Sb_2Te_3 films can induce a similar Te phase-separation instability.

3.3 Fluence Dependence of the Phonon Amplitudes

In order to investigate the dependence of the laser modifications to the sample on the irradiation fluence, the optical phonon amplitudes of Sb_2Te_3 (I_{ST}) and Te (I_T) were plotted as a function of different laser fluences in Figure 3-5. The laser irradiation time was 1 second. As an example, the inset shows the phonon spectra after irradiation by two pump fluences of 3.59 and 4.26 mJ/cm^2. It can be seen that as the exposure fluence increases, the Sb_2Te_3 phonon amplitude decreases while the Te phonon amplitude increases. This is consistent with our suggestion that the appearance of the Te optical phonon originates from the decomposition of Sb_2Te_3 by high fluence pulses and the subsequent formation of a Te phase.

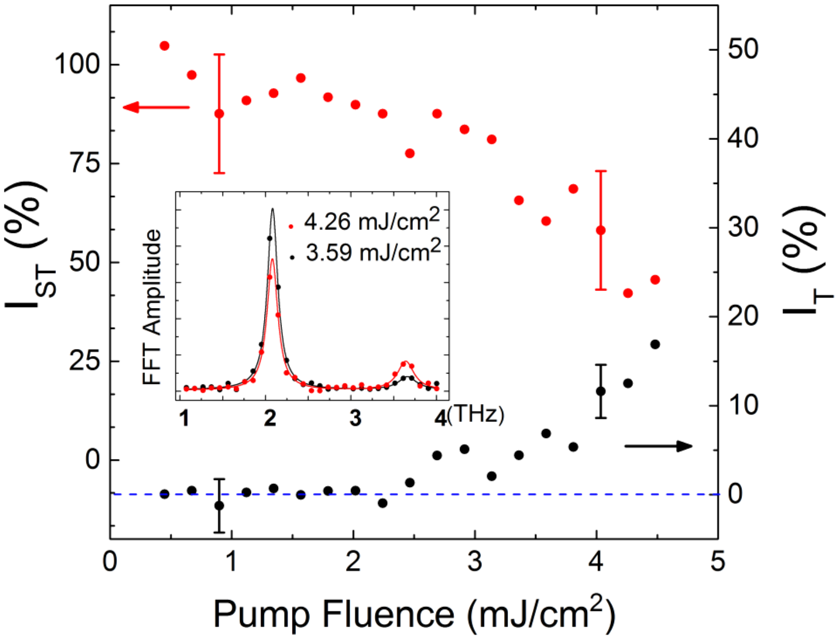

Figure 3-5. The percentage amplitude change of Sb_2Te_3 (I_{ST}) and Te (I_T) A_{1g} optical phonons as a function of the irradiation fluence. I_{ST} and I_T are normalized by the Sb_2Te_3 phonon amplitude before irradiation. The inset shows two phonon spectra after the fs laser irradiation with fluences of 3.59 mJ/cm^2 and 4.26 mJ/cm^2, respectively. The blue dashed line marks the level of 0% tellurium in the spectra to highlight the threshold behavior of the I_{ST} trend.

A further interesting observation from Figure 3-5 is that the threshold behavior exhibited by the increase in Te optical phonon amplitude: irradiation by a laser pulse weaker than 2.47 mJ/cm^2 forms an insignificant amount of Te, while exposure to a laser pulse stronger than this threshold generates Te phonon features that continuously grow with the laser fluences. On the other hand, similar threshold behavior is not as obvious for the Sb_2Te_3 phonon peak. The higher threshold measured for the Te peak may be related to the additional laser energy needed to form the Te phase rather than simply breaking the bonds inside the Sb_2Te_3 crystal.

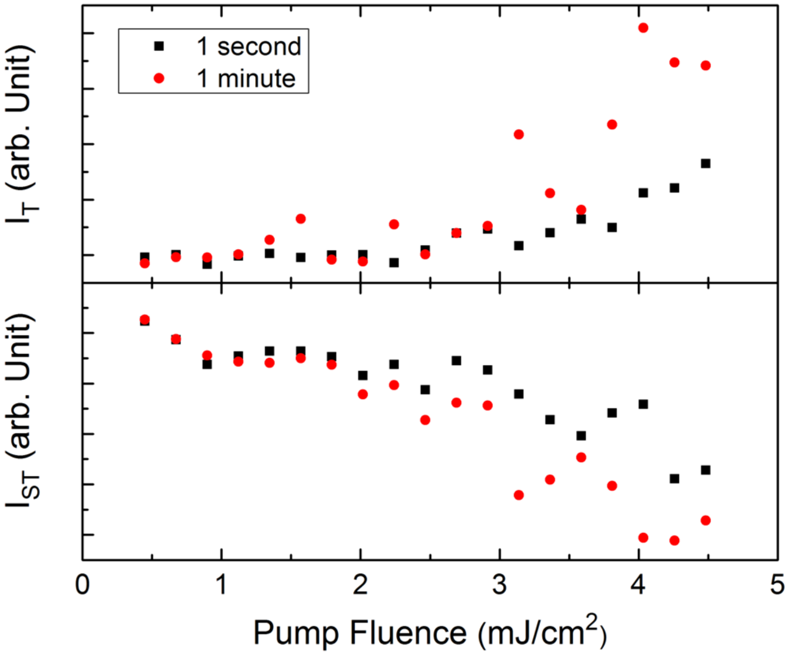

Figure 3-6. Dependence of the Sb_2Te_3 and Te coherent phonon amplitudes on the fs laser fluence after irradiations for 1 second (black squares) and 1 minute (red circles).

A similar relationship of phonon amplitude change vs. laser fluence is shown in Figure 3-6, where the results with laser irradiation times of 1 second and 1 minute were displayed in the same plots. For the phonon amplitude change in the case of Te, the much longer irradiation time of 1 minute does not result in a significantly higher Te amplitude compared to 1 second until the laser fluence is above ~ 3 mJ/cm^2. For the case of Sb_2Te_3 decomposition, on the other hand, the effect of longer irradiation time sets in at a lower fluence, below 2 mJ/cm^2. For the high fluence range (> 3 mJ/cm^2), the significant difference in the phonon amplitudes at short and long irradiation times points to the presence of an incubation effect during the phase decomposition and segregation process. This effect could be the result of the heat accumulation from successive laser pulses, progressive change in surface morphology that may affect the laser coupling to the material at a later time, or some other more complex fs laser-Sb_2Te_3 interactions. These processes, as suggested by Figure 3-6, do not become significant until the laser fluence exceeds a certain threshold.

References

[3.1] M. Först, T. Dekorsy, C. Trappe, M. Laurenzis, and H. Kurz, "Phase change in $Ge_2Sb_2Te_5$ films investigated by coherent phonon spectroscopy", *Appl. Phys. Lett.* **77**, 1964 (2000)

[3.2] J. Hernandez-Rueda, A. Savoia, W. Gawelda, J. Solis, B. Mansart, D. Boschetto, and J. Siegel, "Coherent optical phonons in different phases of $Ge_2Sb_2Te_5$ upon strong laser excitation", *Appl. Phys. Lett.* **98** 251906 (2011)

[3.3] A. Shalini, Y. Liu, U. A. S. Al-Jarah, G. P. Srivastava, C. D. Wright. F. Katmis, W. Braun, and R. J. Hicken, "Observation of T_2-like coherent optical phonons in epitaxial $Ge_2Sb_2Te_5$/GaSb(001) films", *Sci. Rep.* **3**, 2965 (2013)

[3.4] M. Hase, Y. Miyamoto, and J. Tominaga, "Ultrafast dephasing of coherent optical phonons in atomically controlled GeTe/Sb_2Te_3 superlattices", *Phys. Rev. B* **79**, 174112 (2009)

[3.5] A. Q. Wu, X. Xu, and R. Venkatasubramanian, "Ultrafast dynamics of photoexcited coherent phonon in Bi_2Te_3 thin films", *Appl. Phys. Lett.* **92**, 01108 (2008)

[3.6] S. Li, H. Huang, W. Zhu, W. Wang, K. Chen, D. Yao, Y. Wang, T. Lai, Y. Wu, and F. Gan, "Femtosecond laser-induced crystallization of amorphous Sb_2Te_3 film and coherent phonon spectroscopy characterization and optical injection of electron spins", *J. Appl. Phys.* **110**, 053523 (2011)

[3.7] Y. Wang, X. Xu, and R. Venkatasubramanian, "Reduction in coherent phonon lifetime in Bi_2Te_3/Sb_2Te_3 superlattices", *Appl. Phys. Lett.* **93** 113114 (2008)

[3.8] M. Hase, and J. Tominaga, "Thermal conductivity of GeTe/Sb_2Te_3 superlattices measured by coherent phonon spectroscopy", *Appl. Phys. Lett.* **99**, 031902 (2011)

[3.9] Y. Li, V. A. Stoica, L. Endicott, G. Wang, C. Uher, and R. Clarke, "Coherent optical phonon spectroscopy studies of femtosecond-laser modified Sb_2Te_3 films", *Appl. Phys. Lett.* **97**, 171908 (2010)

[3.10] W. Richter, H. Köhler, and C. R. Becker, "A Raman and far-infrared investigation of phonons in the rhombohedral V_2-VI_3 compounds", *Phys. Stat. Sol. (b)* **84**, 619 (1977)

[3.11] G. C. Sosso, S. Caravati, and M. Bernasconi, "Vibrational properties of crystalline Sb_2Te_3 from first principles", *J. Phys.: Condens. Matter* **21**, 095410 (2009)

[3.12] T. Thonhauser, T. J. Scheidemantel, J. O. Sofo, J. V. Badding, and G. D. Mahan, "Thermoelectric properties of Sb_2Te_3 under pressure and uniaxial stress", *Phys. Rev. B* **68**, 085201 (2003)

[3.13] O. Madelung, U. Rössler, and M. Schulz, eds. "Antimony telluride (Sb_2Te_3) band structure, energy gap", *Landolt-Börnstein - Group III Condensed Matter* **41C** (Springer Berlin Heidelberg, 1998)

[3.14] J. M. Khosrofian and B. A. Garetz, "Measurement of a Gaussian laser beam diameter through the direct inversion of knife-edge data", *Appl. Opt.* **22,** 3406 (1983)

[3.15] A. S. Pine and G. Dresselhaus, "Raman spectra and lattice dynamics of tellurium", *Phys. Rev. B* **4**, 356 (1971)

[3.16] T. Dekorsy, H. Auer, C. Waschke, H. J. Bakker, H. G. Roskos, H. Kurz, V. Wagner, and P. Grosse, "Emission of submillimeter electromagnetic waves by coherent phonons", *Phys. Rev. Lett.* **74**, 738 (1995)

[3.17] M. Hase, K. Mizoguchi, H. Harima, S. Nakashima, M. Tani, K. Sakai, and M. Hangyo, "Optical control of coherent optical phonons in bismuth films", *Appl. Phys. Lett.* **69**, 2474 (1996)

[3.18] O. V. Misochko, M. V. Lebedev, and T. Dekorsy, "Observation of longitudinal optical-transverse optical splitting for E-symmetry phonons in Te by coherent phonon spectroscopy", *J. Phys.: Condens. Matter* **17**, 3015 (2005)

[3.19] K. Norimatsu, J. Hu, A. Goto, K. Igarashi, T. Sasagawa, K. G. Nakamura, "Coherent optical phonons in a Bi_2Se_3 single crystal measured via transient anisotropic reflectivity", *Solid State Commun.* **157**, 58 (2013)

[3.20] O. Madelung, U. Rössler, and M. Schulz, eds. "Antimony oxide (Sb_2O_3) Raman frequencies", *Landolt-Börnstein - Group III Condensed Matter* **41C** (Springer Berlin Heidelberg, 1998)

[3.21] A. L. J. Pereira, L. Gracia, D. Santamanría-Pérez, R. Vilaplana, F. J. Manjón, D. Errandonea, M. Nalin, and A. Beltrán, "Structural and vibrational study of cubic Sb_2O_3 under high pressure", *Phys. Rev. B* **85**, 174108 (2012)

[3.22] P. J. Carroll and J. S. Lannin, "Vibrational properties of crystalline group-VI solids: Te, Se, S", *Phys. Rev. B* **27**, 1028 (1983)

[3.23] J. S. Lannin, J. M. Calleja, and M. Cardona, "Second-order Raman scattering in the group-V_b semimetals: Bi, Sb, and As", *Phys. Rev. B* **12**, 585 (1975)

[3.24] A. S. Pine and G. Dresselhaus, "Raman scattering in paratellurite, TeO_2", *Phys. Rev. B* **5**, 4087 (1972)

[3.25] V. Russo, A. Bailini, M. Zamboni, M. Passoni, C. Conti, C. S. Casari, A. Li Bassi, and C. E. Bottani, "Raman spectroscopy of Bi-Te thin films", *J. Raman Spectrosc.* **39**, 205 (2008)

[3.26] D. Drews, J. Sahm, W. Richter, D. R. T. Zahn, "Molecular-beam-epitaxy growth of CdTe on InSb (110) monitored *in situ* by Raman spectroscopy", *J. Appl. Phys.* **78**, 4060 (1995)

[3.27] P. M. Amirtharaj and F. H. Pollak, "Raman scattering study of the properties and removal of excess Te on CdTe surfaces", *Appl. Phys. Lett.* **45**, 789 (1984)

[3.28] L. Krusin-Elbaum, C. Cabral, Jr., K. N. Chen, M. Copel, D. W. Abraham, K. B. Reuter, S. M. Rossnagel, J. Bruley, V. R. Deline, "Evidence for segregation of Te in $Ge_2Sb_2Te_5$ films: effects on the "phase-change" stress", *Appl. Phys. Lett.* **90**, 141902 (2007)

[3.29] E. M. Larramendi, G. Berth, V. Wiedemeier, K-P Hüsch, A. Zrenner, U. Woggon, E. Tschumak, K. Lischka, and D. Schikora, "Intensity enhancement of Te Raman modes by laser damage in ZnTe epilayers", *Semicond. Sci. Technol.* **25**, 075003 (2010)

[3.30] M. R. Ananthan, B. C. Mohanty, and S. Kasiviswanathan, "Micro-Raman spectroscopy studies of bulk and thin films of $CuInTe_2$", *Semicond. Sci. Technol.* **24**, 075019 (2009)

[3.31] J. Lambert, P. V. Huong, J. Limtrakul, and J. Launay, "A mechanism for the photoconduction in $CdIn_2Te_4$, $ZnIn_2Te_4$ and $MnIn_2Te_4$ semiconductors", *J. Mol. Struct*. **294**, 159 (1993)

[3.32] S. A. Hawkins, E. Villa-Aleman, M. C. Duff, D. B. Hunter, A. Burger, M. Groza, V. Buliga, and D. R. Black, "Light-induced tellurium enrichment on CdZnTe crystal surfaces detected by Raman spectroscopy", *J. Electron. Mater.* **37**, 1438 (2008)

[3.33] L. C. Teague, S. A. Hawkins, M. C. Duff, M. Groza, V. Buliga, and A. Burger, "AFM characterization of Raman laser-induced damage on CdZnTe crystal surfaces", *J. Electron. Mater.* **38**, 1522 (2009)

[3.34] Portions of this chapter were reproduced with permission from Y. Li, V. A. Stoica, L. Endicott, G. Wang, C. Uher, and R. Clarke, *Appl. Phys. Lett.* **97**, 171908 (2010). Copyright 2010, AIP Publishing LLC.

Chapter 4

Femtosecond Laser-Induced Nanostructures in Sb_2Te_3

4.1 Overview

One of the most intriguing and valuable aspects of lasers is their ability to modify materials by irradiation. The modifications can be macroscopically distinct, such as surface morphology, or they can be alterations to the materials properties on a more microscopic scale, such as composition or crystal structure changes. In the previous chapter, we demonstrated the possibility that irradiation of Sb_2Te_3 using femtosecond lasers can lead to tellurium segregation. Therefore, pump-probe experiments aimed at studying the properties of the pristine Sb_2Te_3 film need to have their laser fluence below a certain threshold to maintain the film's integrity during the measurements. In this chapter, we study the other end of the laser-film interaction spectrum: the use of a high-fluence fs laser to create ordered nanostructures on Sb_2Te_3 thin films.

Sb_2Te_3 is one of the most widely used materials for thermoelectric applications, as discussed in Chapter 1. In particular, low dimensional structures such as thin films, nanowires, and quantum dots have been predicted [4.1, 4.2] to have a significantly higher energy conversion efficiency compared to the bulk forms of the material, due to energy filtering, quantum confinement, and enhanced phonon scattering on multiple boundaries. Indeed, measurements on Sb_2Te_3 nanowires have demonstrated thermoelectric power enhancement at the smallest wire diameters [4.3]. In addition to its attractive thermoelectric properties, Sb_2Te_3 has been shown to be a promising candidate material for a topological insulator, which is characterized by conductive states at the surface and insulating states in the bulk [4.4]. One-dimensional Sb_2Te_3 nanostructures may be of particular interest in providing a means to tune the surface-to-volume ratio and enhance the contribution of exotic surface states [4.5].

Among a variety of approaches to create microstructures and nanostructures, the laser-induced periodic surface structures (LIPSS) - arrays of "micro- or nano-ripples" formed after laser irradiation, have attracted considerable interest. The first observation was made by Birnbaum on several semiconductor bulk samples using ruby lasers in 1965 [4.6]. Since then, LIPSS have been reported in a wide range of materials after irradiation by cw and nanosecond lasers, with an orientation perpendicular to the laser's linear polarization and a periodicity around $\lambda/(1\pm\sin\theta)$, where λ is the irradiation laser wavelength and θ is the incidence angle [4.7-4.14]. They were termed low-spatial-frequency LIPSS (LSFL) to emphasize their large periodicity compared to another type of LIPSS discussed below. The formation mechanism of LSFL was proposed as an interference effect between the incident and the surface-scattered waves [4.15].

As ultrafast lasers became more widely available in the 1990s, a new type of LIPSS has emerged from ultrafast laser irradiation. These so-called high-spatial-frequency-LIPSS (HSFL) have periodicities many times or even an order of magnitude below the irradiation laser wavelength [4.16-4.24], making them impossible to come from simple interference between laser beams. In particular, the close proximity of the HSFL periodicity to $\lambda/2n$ observed over a wide range of materials and laser wavelengths, where n is the refractive index of the material irradiated, has led to a number of theories on the generation mechanism of HSFL. For example, one of the most actively researched models suggests that the small periodicity of HSFL is a result of a complex interaction between the laser and the laser excited plasmon inside the material [4.17, 4.21]. Other theories include self organization [4.25, 4.26], second harmonic generation [4.27], and the nanoplasma formation from local field enhancement [4.22, 4.28]. These investigations usually involve a careful comparison between the measured HSFL periodicity and the value calculated from the proposed model. Additionally, several other studies have also employed single- and multiple-pulse irradiations to monitor the formation of HSFL as a function of pulse numbers [4.24, 4.29, 4.36]. The absence of LIPSS from any single-pulse irradiation suggests a feedback mechanism at work during the formation process. The explanation for how HSFL is generated is an important and fascinating topic that is currently under intense investigation and active debate by a multitude of research groups.

Interestingly, HSFL were found predominantly in semiconductor and dielectric materials where the material's bandgap is larger than the irradiation photon energy [4.16-4.19, 4.30, 4.31], with few exceptions [4.24, 4.32]. The most convincing report on this bandgap-photon energy relationship is a systematic study performed on InP, GaP and GaAs with three laser wavelengths, where HSFL only shows up when the laser is in the transparency regime of the semiconductor [4.31]. Combined with the widely known observation that HSFL only show up after irradiations from ultrafast lasers but never cw lasers [4.7-4.24], these experimental results have further suggested the importance of a high-intensity laser field in the formation of HSFL, agreeing well with the plasmonic picture of the interaction process. As a result of the challenges associated with HSFL formation in materials opaque to the irradiation laser, fs laser-induced nanostructure formation has remained elusive for certain technologically important narrow-bandgap semiconductors such as Sb_2Te_3, which is highly absorbing in the visible and near-infrared spectral regions [4.3, 4.33].

In this chapter, we will present a detailed investigation of HSFL formation on Sb_2Te_3 thin films using femtosecond lasers. Section 4.2 introduces the procedures involved in the creation of nanostructures, including laser alignment techniques and the scanning process. These well-controlled and consistently-performed procedures are critical for a reliable comparison between HSFL formed in different stages of laser irradiation. Section 4.3 discusses the microscopic characterization techniques employed for close examinations on the nanostructures, the results from which will be shown in the next two sections. Section 4.4 presents a systematic study on how the surface morphologies of HSFL in Sb_2Te_3 films depend on a series of laser irradiation conditions, including fluence, scan speed and laser wavelength. These results will provide valuable experimental support for future endeavors to fabricate low-dimensional nanoscale devices with this important material [4.34]. The HSFL investigations on Sb_2Te_3 are expanded in section 4.5 to a microscopic examination of the cross section of these ordered nanostructures, where the phases present in the nanostructured region are identified and their spatial distribution elucidated. These findings were further supported by a series of X-ray diffraction measurements demonstrated in section 4.6. The clarification of these phases serves a critical role in the fabrication of highly-ordered horizontal Sb_2Te_3 nanowires in potential integrated planar applications. Section 4.7 presents a set of experiments that reveal the sensitivity of the HSFL morphology to the ambient environment in which the laser irradiations are carried out. These results open up potential research directions that may lead to a deeper understanding of the processes involved in the HSFL formation in Sb_2Te_3. Finally, section 4.8 shows some of the preliminary thermal and STM results on HSFL. These measurements represent the beginning of a rich variety of research projects that are currently underway.

4.2 Laser Processing Procedures

The laser nanostructuring experiments were done on two different setups: first with the 1560 nm laser in Clarke's lab and later with the lasers (1560 nm, 1030 nm and 780 nm) in Pipe's lab. The lasers in both labs have the same repetition rate of 100 MHz and very similar pulse durations. In particular, the 1560 nm lasers in both labs have the same configuration parameters except that the one in Clarke's lab provides a laser fluence of up to ~ 6 mJ/cm^2, while the one in Pipe's lab can go up to ~ 15 mJ/cm^2. The early results on fs laser induced nanostructures were obtained with the setup in Clarke's lab on Sb_2Te_3 thin films of 100 nm to 200 nm in thickness deposited directly on the Al_2O_3 substrates. Later, more systematic studies on these nanostructures were performed with the setup in Pipe's lab. The samples used in these newer studies were ~100 nm Sb_2Te_3 thin films on Al_2O_3 substrates with a ~ 10 nm buffer layer of Bi_2Te_3 between the Sb_2Te_3 and the Al_2O_3.

The transition to the new setup in Pipe's lab was made in an effort to explore a wider range of experiment options, thanks to the larger laser power it provides, which goes up to almost four times as much as the maximum power in the original setup. With the larger power, a laser focal spot size 1.5 times that in the original setup can be created along with a maximum laser fluence over twice as much as that of the original. The increased spot size results in a wider irradiated area and consequently, a larger number of nanotracks. The expanded dimensions of the nanotrack region makes it easier to perform lithography processing in preparation for potential transport measurements over these nanostructures. In addition, as was mentioned in the previous section, laser wavelength dependence of the nanostructure morphology has been observed in both HSFL and LSFL. The availability of three different laser wavelengths offers an excellent opportunity to create and investigate nanotracks of various widths.

The choice of adding a buffer layer of Bi_2Te_3 between the Sb_2Te_3 thin film and the Al_2O_3 substrate was made based on the empirical observation that such a sample configuration gives the most continuous and ordered nanotracks, as will be shown later in section 4.4. This is especially prominent in thinner Sb_2Te_3 films of around 100 nm, where samples without the buffer layer have a tendency to form disordered nanorods, with their specific morphology greatly depending on the film quality. The samples with the buffer layer, on the other hand, produced ordered nanotracks with minimum morphology variations sample-to-sample over a fixed range of laser fluence and scan speed. The consistency and predictability of the nanotrack morphology from the samples with the buffer layer could be due to a more consistent quality of the Sb_2Te_3 layer, since Bi_2Te_3 and Sb_2Te_3 share very similar lattice parameters. The addition of the Bi_2Te_3 layer also slows down the heat dissipation into the Al_2O_3 substrate, resulting in a larger heat accumulation and raised temperature during the laser irradiation of the sample. Further studies are necessary to clarify the role of the Bi_2Te_3 layer in nanotrack formation.

The laser irradiation procedures were the same in both setups. The Sb_2Te_3 thin film sample was mounted on an XYZ translation stage. A collimated 1560 nm fs laser beam was focused by a parabolic mirror and incident normally onto the thin film. The film was then moved transversely in a direction perpendicular to the laser propagation. This allows the laser to scan across the surface of the film. A CCD camera connected with a telescope was used to monitor a magnified image of the sample area around the focused beam spot. The irradiation laser polarization was controlled by having the laser go through a quarter waveplate, a half waveplate and then a linear polarizer. The quarter waveplate was used to control the linearity of the polarization, while the combination of the half waveplate and the polarizer were used for linear polarization direction control and laser power control. A flip mirror was used to direct the laser beam to a thermal power meter (Thorlabs S302C) for the laser power measurement.

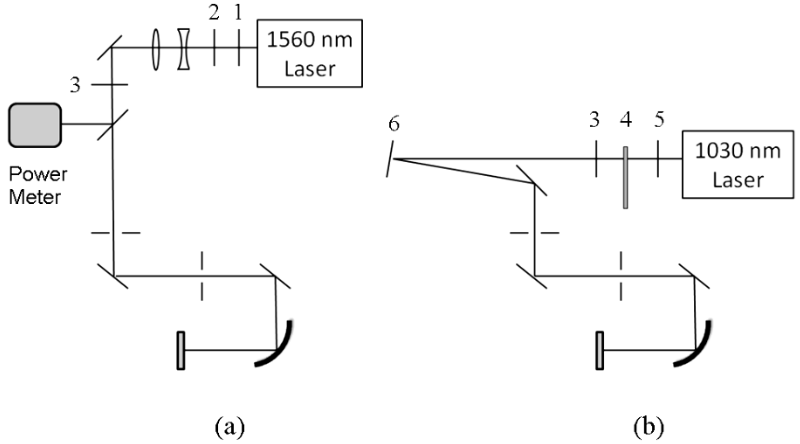

Figure 4-1. The experiment setups for the fs laser nanostructuring on the Sb_2Te_3 thin films by (a) the 1560 nm laser and (b) the 1030 nm laser. Setup (b) was aligned based on the two apertures placed in the setup (a). 1 - quarter-wave plate; 2 - half-wave plate; 3 - linear polarizer; 4 - variable neutral density filter; 5 - long-pass color filter, cutoff at 610 nm; 6 - power meter when calibrating the amplifier output power, mirror when nanostructuring the Sb_2Te_3 thin films.

To ensure an optimized focused laser beam irradiated on the sample surface and to maintain the consistency of the irradiation condition for each laser writing, fine-tuning of the laser beam alignment was performed each time before the laser irradiation experiments started. To align the laser beam, a piece of GaAs was mounted next to the thin film sample. The GaAs piece (bandgap ~ 1.43 eV) was excited by the focused 1560 nm beam (photon energy ~ 0.8 eV) via two-photon absorption and the intensity of the resulting photoluminescence (PL) signal from the GaAs piece was used to evaluate the beam's focusing condition. A higher PL intensity indicates a more tightly focused beam and therefore a superior focusing condition. The GaAs piece was first placed in focus, which is signaled by a sudden brightening of the PL signal from the piece itself. Then the angles of the two mirrors immediately before the parabolic mirror as well as the tilting angles and location of the parabolic mirror itself were fine-tuned to maximize the PL signal from the GaAs piece as seen from the CCD camera. A few iterations of the fine-tunings of the optics elements as well as the focusing position of the GaAs piece would leave the focused laser beam with the least aberration and the most tightly focused beam. An optimized focusing condition also ensures that the laser irradiation condition is the same each time and makes it easier to compare results from different rounds of irradiation experiments.

The Sb_2Te_3 thin film sample for laser-irradiation experiments was mounted right next to the GaAs piece. After the focusing condition of the optics components was optimized, the Sb_2Te_3 film was moved into the focus of the parabolic mirror. The optimal focusing position of the Sb_2Te_3 film was achieved by maximizing the third harmonic generation (THG) signal from the Sb_2Te_3 surface. Like the two-photon absorption in GaAs, THG is a nonlinear process whose intensity is extremely sensitive to the excitation laser intensity. As the film came into the Rayleigh range of the focused laser beam, this was manifested by a sudden appearance of a bright spot on the film surface as detected by the CCD camera and shown on a monitor screen. This THG signal also served as a guide to the exact location of the focused laser beam on the film. After the THG signal was maximized, the tilting angle of the film was fine-tuned until the THG brightness remained the same over a distance of 2 mm along the film surface. Since most of the laser scans in this work covered distances of less than 500 μm, the film was thus ensured to stay in focus during the whole course of scanning.

The movement of the translation stage on which the samples were mounted was realized by a DC servo motorized actuator (Thorlabs Z812B) connected to a T-cube DC servo motor controller (Thorlabs TDC001). With a resolution of less than 29 nm, the actuator ensured a constant and accurate scanning speed for comparison studies and control over the nanostructure morphologies. Moreover, as will be discussed later in this chapter, the gas environment studies would not be possible without the use of the motorized actuators, since moving the translation stage manually in an enclosed space with a controlled gas environment is extremely challenging.

In addition to the 1560 nm laser, the Sb_2Te_3 film was also irradiated by two other fs lasers with wavelengths of 780 nm and 1030 nm, with pulse durations comparable to that of the 1560 nm laser. For the 780 nm laser writing, since its third harmonic signal is out of the detection range of the CCD camera, tuning of the film focusing position was achieved by overlapping the focal spot of the 780 nm laser with that of the 1560 nm laser. The lateral overlap of the two focal spots perpendicular to the laser propagation was done by overlapping the traveling routes of the two laser beams. The depths of focus were overlapped by fine-tuning the collimator of the 780 nm laser and checked with the razor-blade method (see section 3.1). With the two focal spots overlapped, the film was first put into focus with the 1560 nm laser, and then switched to 780 nm for laser irradiation experiments.

To align the 1030 nm laser beam, two iris apertures were placed in the path of the 1560 nm beam after the flip mirror. The 1030 nm beam was then directed through the centers of the two apertures (Fig. 4-1(b)). While no collimator was used for this beam, the beam divergence appeared small over a distance of 1 meter. Since the laser came out of the "residual light port", the output from this port contains a mixture of the 1030 nm beam and its second harmonic beam at 512 nm. This green beam is filtered out by a long-pass filter with a cutoff at 610 nm. The output power of the 1030 nm beam is controlled by varying the laser diode's current in the amplifier, and the percentage output power is displayed on the control panel of the amplifier. Since the power meter for the 1560 nm beam nanostructuring is placed before the location where the 1030 nm beam joins and travels collinearly with the 1560 nm beam, the exact power values of the 1030 nm beam were calibrated by recording the power with a photo-detector ("6" in Fig. 4-1) corresponding to each percent power displayed by the amplifier control panel. The photo-detector was then replaced by a mirror, and the adjustment and determination of laser fluence irradiated on the samples were realized by a combination of the displayed percentage output power and the calibration table. The fine-tuning of the optical elements and focal position of the sample for the 1030 nm beam were done with the help of the CCD camera, similar to those of the 1560 nm beam. However, although the CCD sensitivity for 1030 nm drops significantly compared to 1560 nm, a small trace of scattered 1030 nm beam off the GaAs could still be detected. To eliminate this weak scattering signal, a short-pass filter was placed in front of the CCD camera, allowing only the PL signal from GaAs to be detected.

4.3 Microscopy Characterization Techniques

To investigate the details of the nanostructures formed by the fs lasers on Sb_2Te_3, various microscopy techniques were carried out at the Electron Microbeam Analysis Laboratory (EMAL) at the University of Michigan. The surface morphology of the irradiated regions was inspected under the scanning electron microscope (SEM) and the atomic force microscope (AFM). In SEM (FEI Nova Nanolab Dualbeam Scanning Electron Microscope), secondary electron (SE) detection mode was used. Since the Sb_2Te_3 films are reasonably conductive ($\rho \sim 10^{-5}\Omega$m at room temperature [4.35]), the charge accumulation effect on the thin film samples is minimal. Therefore, a metal coating on top of the sample prior to SEM examination is not needed. Nevertheless, the insulating Al_2O_3 substrate makes it necessary to connect the film surface to the grounding sample holder with a conductive copper sheet. Considering the vulnerability of Sb_2Te_3, an acceleration voltage of 5 kV and a beam current of 98 pA were used for the electron beam to minimize damage during the imaging process.

In the AFM (Veeco Dimension Icon Atomic Force Microscope) characterizations, tapping mode was used to minimize the mechanical damage to the soft Sb_2Te_3 sample by the AFM tip. The super-sharp tip (Bruker TESP-SS) employed for the tapping mode measurements has a tip radius of less than 5 nm and a half-angle of less than 10 degrees for the first 200 nm of the tip apex. The use of the super-sharp tip helped minimize the artifacts from the tip-sample convolution during the height profiling of the Sb_2Te_3 nanostructures.

Transmission electron microscopy (TEM) was employed for the cross-sectional studies of the nanostructures. Dr. Kai Sun from EMAL has played a crucial role in assistance with obtaining the TEM results. In this case, ultra-thin samples with less than 100 nm thicknesses are required for proper imaging by TEM. Considering the special geometry of the sample - nanostructures composed of a soft material lying on top of a hard substrate, an in-situ lift-out method was chosen for TEM cross-sectional specimen preparation. The lift-out procedure was performed with the FEI Helios 650 Dual Beam focused ion beam (FIB) instrument. To preserve the pristine structure of the cross section, a 2 μm-thick layer of platinum (Pt) was deposited, first by e-beam assisted deposition (1 μm) and then by FIB-assisted deposition (1 μm), on top of the region of interest prior to the FIB milling. Then a thin section (~ 1 μm) across the nanostructures was cut out by the FIB and welded onto the FIB lift-out grid with Pt. The specimen was further thinned down to about 100 nm with the FIB. The ion beam voltage and current was minimized during the thinning process to avoid damage to the side of the specimen.

The cross-sectional specimen was inspected by three TEM instruments: JEOL 2010F Analytical Electron Microscope ("2010F"), JEOL 3011 High Resolution Electron Microscope ("3011"), and JEOL 2100F Analytical Electron Microscope ("2100F"). The 2010F was used for low-magnification high-angle annular dark field (HAADF) imaging, nano-beam electron diffraction (NBED) and X-ray energy dispersive spectroscopy (EDS) element mapping. The 3011 was used for high-resolution HAADF imaging and selected-area electron diffraction (SAED) studies. The 2100F was used for high-resolution HAADF imaging operating in the scanning transmission electron microscopy (STEM) mode. With the combined results from these examinations, the various phases present in the nanostructured regions and their crystal structures can be identified and evaluated.

4.4 Surface Morphologies

Figure 4-2 shows the surface morphology of a 200 nm Sb_2Te_3 thin film on an Al_2O_3 substrate irradiated by the 1560 nm fs laser in Clarke's lab with a fluence of 6.3 mJ/cm^2 and a scan speed of 10 μm/s. The surface roughness of the film, defined as the arithmetical average of the surface profile, R_a, is ~ 5 nm. Four highly-aligned nanotracks are clearly visible in the irradiated region (Fig. 4-2 (a)), with widths in the range of 45 - 80 nm and an average spacing, Λ, of 130 ± 10 nm. The observed spacing is consistent with an estimate based on the lateral interference condition $\Lambda = \lambda/2n = 131.7$ nm, discussed previously in section 4.1. The nanotrack orientation is perpendicular to the laser polarization. Figure 4-2 (b) is the SEM image of a similar region at a 45° viewing angle, showing the nanotracks as rounded ridges with numerous nanometer-size particles scattered along the top. Figure 4-2 (c) is the 2D height profile of a similar region measured by AFM, with a section of the profile along the white line (perpendicular to the nanotracks) displayed on the right. This cross sectional height profile reveals two nanotracks of ~ 40 nm top-to-valley sitting near the bottom of a trench.

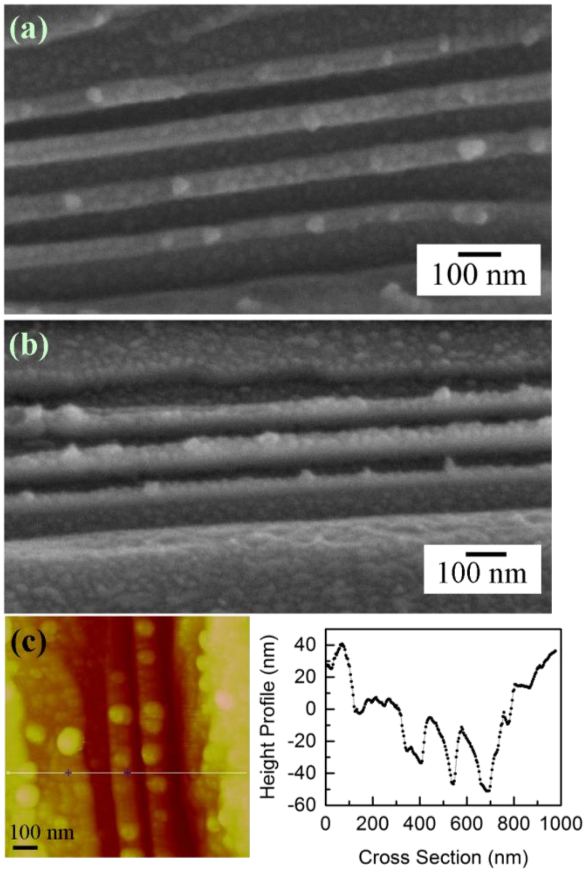

Figure 4-2. Surface morphology of the nanotracks on a 200 nm Sb_2Te_3 thin film with a laser fluence of 6.3 mJ/cm^2 and a scan speed of 10 μm/s. (a) SEM plan-view image; (b) SEM image with a 45° viewing angle. (c) AFM height profile, revealing a nanotrack height of 40 nm - 50 nm.

In order to study the dependence of the nanotrack morphology on the laser fluence, three regions on another 200 nm film were irradiated with a scan speed of 10 μm/s, each with a different fluence: 3.9 mJ/cm^2, 5.2 mJ/cm^2, and 6.3 mJ/cm^2 (Figure 4-3). The laser in Clarke's lab was used. The film used had a much rougher surface of R_a ~ 23 nm, as measured by AFM. For all three regions, groups of nanotracks were observed to develop with a 1.5 ± 0.1 μm periodicity matching that of the laser wavelength. These nanotrack groups were separated by smoother regions which appear to be annealed. As the fluence increased, the areas covered by the nanotracks expanded into the annealed regions and eventually covered the entire irradiated area. However, over the range of fluences tested, which is up to 6.3 mJ/cm^2, no change was observed in the period of the nanotracks themselves (~ 130 nm).

The periodic appearance of the nanotrack groups and their dependence on the laser fluence can be analyzed in terms of the following processes: the interference between the normal-incidence laser beam and the surface-scattered electromagnetic wave creates a periodic variation of laser intensity along the sample's surface with a period close to the laser wavelength [4.15]. Near the nodes of the interference pattern, the low intensity laser irradiation causes a mild annealing of the film surface, while near the antinodes of the interference pattern, the high laser intensity leads to periodic modifications to the material from the surface of the film and the generation of the nanotracks. As the laser fluence grows from 3.9 mJ/cm^2 to 6.3 mJ/cm^2, the amplitude of the interference standing wave increases, thereby expanding the areas around the antinodes in which the laser intensity exceeds the threshold for nanotrack formation. Consequently, the nanostructure region extends outwards into the annealed areas as the laser fluence increases.

In addition to the laser fluence, the nanostructure morphology also depends on the laser irradiation time, which is controlled by the scan speed. Figure 4-4 shows two regions on the same film as Fig. 4-2 irradiated by a laser fluence of 6.3 mJ/cm^2 at two different scan speeds: 1 μm/s and 10 μm/s. With a spot diameter of ~ 3.2 μm, the irradiation time at each location along the scan is about 3.2 seconds for the speed of 1 μm/s and 0.32 seconds for the 10 μm/s. Taking into account the laser repetition rate of 100 MHz, the number of laser pulses irradiated on each location is 320 million for the 1 μm/s and 32 million for the 10 μm/s. At 1 μm/s, the irradiated region is dominated by quasi-ordered nanostructures. As the speed increases to 10 μm/s and the corresponding irradiation time decreases by a factor of 10, the irradiated region becomes covered with highly ordered and continuous nanotracks with spacing comparable to their width.

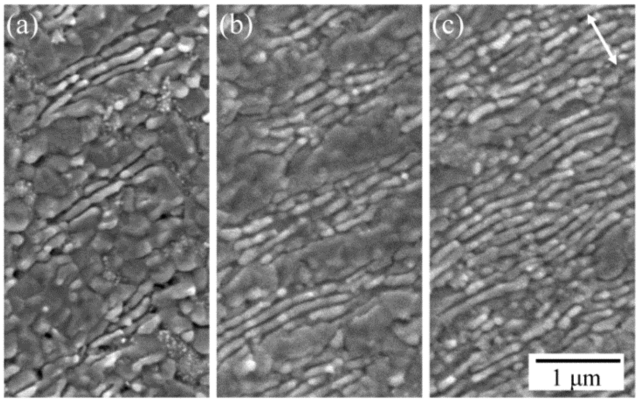

Figure 4-3. Fluence dependence of the nanotracks on a rough 200 nm Sb_2Te_3 film. The scan speed was 10 μm/s for all cases and the laser fluence was (a) 3.9 mJ/cm^2, (b) 5.2 mJ/cm^2, and (c) 6.3 mJ/cm^2. The arrow indicates the plane of laser polarization.

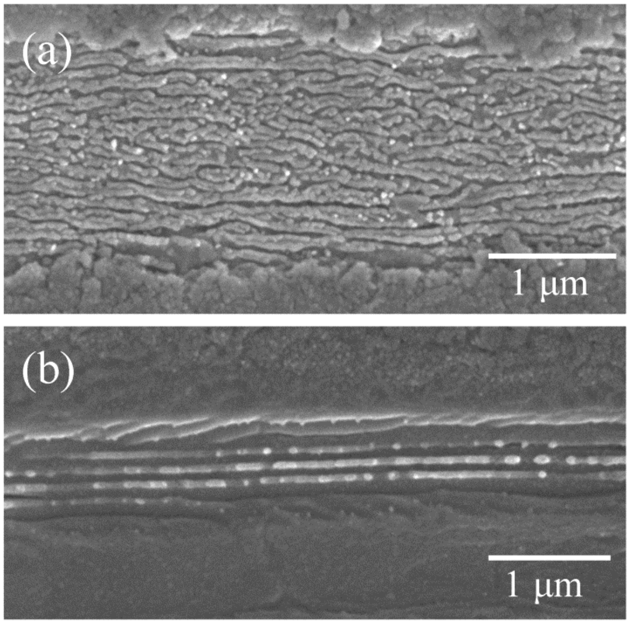

Figure 4-4. SEM images of the nanotracks on the smooth 200 nm Sb_2Te_3 thin film after irradiation by the fs laser with a fluence of 6.3 mJ/cm^2 and scan speeds of (a) 1μm/s and (b) 10 μm/s.

The results in the rest of this section were obtained with the lasers in Pipe's lab on 100 nm - 300 nm Sb_2Te_3 thin films on Al_2O_3 substrates with a 5 nm - 10 nm Bi_2Te_3 buffer layer between the Sb_2Te_3 and the Al_2O_3. Figures 4-5 (a) and (b) show the representative surface morphology of groups of highly-ordered nanotracks formed after irradiation by the 1560 nm fs laser with a scan speed of 5 μm/s and fluence of 8.4 mJ/cm^2 and 10.1 mJ/cm^2. The nanotracks have a periodicity of around 130 nm, close to λ/2n, and a range of widths around 70 nm - 100 nm. Compared to the ones shown earlier in this section, the number of nanotracks generated here is significantly larger and show continuity over a longer distance, making this sample/irradiation configuration appealing for potential applications in fabricating planar nano-devices.

One of the interesting features in Fig. 4-5 (a) and (b) is the abrupt borders for both the nanotrack region and the side-region that seems significantly smoother compared to the rest of the film. These borders suggest the existence of thresholds for initiating the dynamics that result in these two surface morphologies. The fluence ranges for these two dynamics regimes can be understood in terms of the Gaussian spatial profile of the laser focal spot. Near the center of the focal spot, the fluence is higher, corresponding to a fluence range for nanotrack generation. Moving away from the center of the spot, the fluence drops below the threshold for initiating the nanotrack generation, down to the range for surface smoothening. As the laser fluence increases from 8.4 mJ/cm^2 to 10.1 mJ/cm^2, both borders expand outwards. If we consider a laser spatial profile of $F \times \exp\left(-x^2/x_o^2\right)$, where F is the peak of the laser spot, the threshold fluence F_{th} is related to the border position x_{th} by:

$$F_{th} = Fe^{-x_{th}^2/x_o^2} \tag{4.1}$$

In the case of Fig. 4-5, x_{th} is equal to $d/2$ and $D/2$ for the nanotracks region and the smooth surface region, respectively. Let the corresponding thresholds be F_{th_d} and F_{th_D}. The peak fluence is related to d and D by:

$$d^2 = 4x_o^2 \ln F - 4x_o^2 \ln F_{th\_d} \tag{4.2}$$

$$D^2 = 4x_o^2 \ln F - 4x_o^2 \ln F_{th\_D} \tag{4.3}$$

If F_{th} and x_o do not depend on F, d^2 and D^2 will be linearly related to $\ln F$, with a slope of $4x_o^2$ and an intercept of $-4x_o^2 \ln F_{th}$. The linear relationships are confirmed in Fig. 4-5 (c), from which the laser spot size $2x_o$ was determined to be 4.2 μm, and the fluence thresholds were calculated to be 7.7 mJ/cm^2 for the nanotracks and 3.9 mJ/cm^2 for the surface smoothening, in good agreement with the observations in the Sb_2Te_3 thin films with the Bi_2Te_3 buffer layer irradiated by the 1560 nm laser with a scan speed of 5 μm/s.

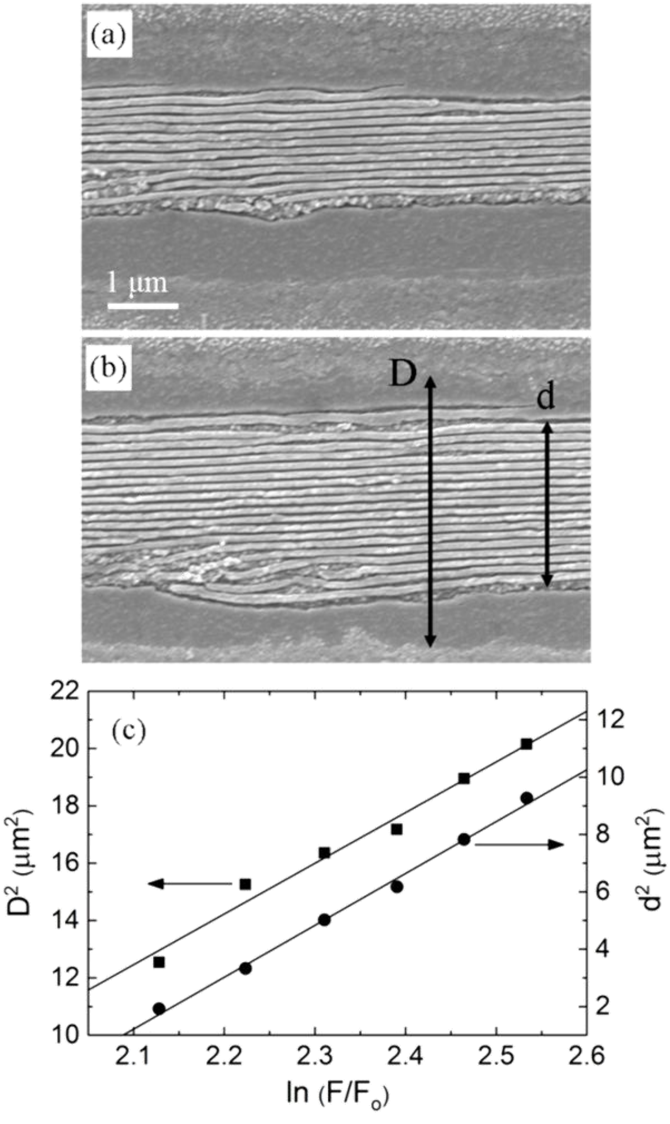

Figure 4-5. Nanotracks on a 100 nm Sb_2Te_3 thin film with a Bi_2Te_3 buffer layer between the film and the Al_2O_3 substrate. The nanotracks were induced by a 1560 nm fs laser with a scan speed of 5 μm/s and a fluence of (a) 8.4 mJ/cm^2 and (b) 10.1 mJ/cm^2. The two black double-arrows in (b) indicate the definitions of d and D - the threshold for nanotrack generation and surface smoothening, respectively. (c) shows that d^2 and D^2 are linearly related to the natural log of the laser fluence, confirming the existence of constant thresholds for the two types of laser-Sb_2Te_3 interactions. F_o is the unit fluence, 1 mJ/cm^2. The square dots and the round dots correspond to the experiment data for d^2 and D^2, respectively. The solid lines are the linear best fits to the data.

Three AFM height profiles of the nanotracks by different laser fluences (8.4 mJ/cm^2, 9.2 mJ/cm^2, and 10.1 mJ/cm^2) are shown in Figure 4-6, each with a cross sectional profile taken perpendicular to the nanotrack orientation. The depth of the valleys between the nanotracks ranges from 15 nm to 40 nm, with no significant average depth difference between the three fluences. Considering a total thickness of the film of 105 nm, the valleys do not extend all the way down to the substrate. This suggests that the nanotracks are interconnected near the bottom of the valleys and that in order to have individual in-plane nanowires as suggested in section 4.1, thinner films are needed to physically separate the nanotracks. However, as we will see later in this chapter, these physically connected nanotracks can still be separated in the sense of different crystal phases. A more detailed study and discussion on this topic will be presented in the next section.

While the laser fluence does not seem to have much observable effect on the height profile of the nanotracks, it does influence the width of the nanotracks. This is manifested as a slight increase in the width as the individual nanotrack is located further away from the center of the nanotrack region, where the laser fluence is the highest. For example, in the case of the fluence of 10.1 mJ/cm^2 shown in Figure 4-7, the nanotrack width increases mildly as the distance between the nanotracks and the center of the nanotrack region increases. Note that even along a single continuous nanotrack, a width variation of more than 5 nm is commonly observed. Nevertheless, the width-distance correlation still exists after an averaging was performed over each individual nanotrack.

Another example of the nanotrack width dependence on the laser fluence is illustrated in Figure 4-8, where the width of the center-most nanotrack in each of the eight nanotrack regions is plotted against the corresponding spatially-averaged irradiation laser fluence as measured by the power meter. Again, the overall trend shows a negative correlation between the two parameters, consistent with the observation on a single nanotrack region in Fig. 4-7. The nanotrack periodicity was also plotted against the same fluence scale, displaying a comparatively constant value of around 125 nm throughout the fluence variation from 8.4 mJ/cm^2 to 14.3 mJ/cm^2. Similar to the nanotrack width case, the periodicity measurement is plagued with variations of several nanometers, mostly due to bifurcations and slightly disordered alignments of the nanotracks.

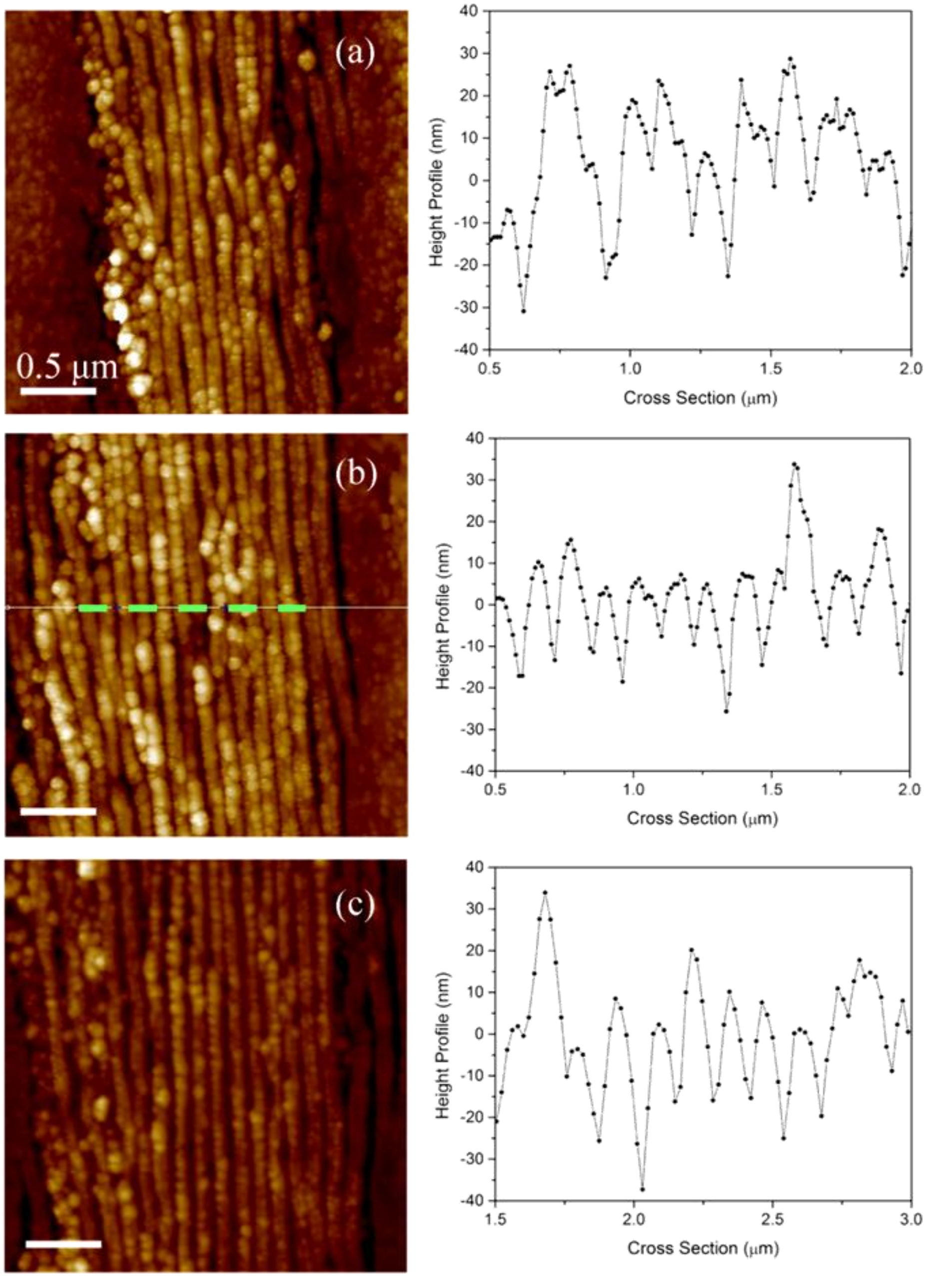

Figure 4-6. Height profiles of the nanotracks irradiated by the 1560 nm fs laser with a scan speed of 5 μm/s and a fluence of (a) 8.4 mJ/cm^2, (b) 9.2 mJ/cm^2, and (c) 10.1 mJ/cm^2. The green dashed line in (b) indicates the direction of the line sections along which the cross sectional height profiles on the right column were measured.

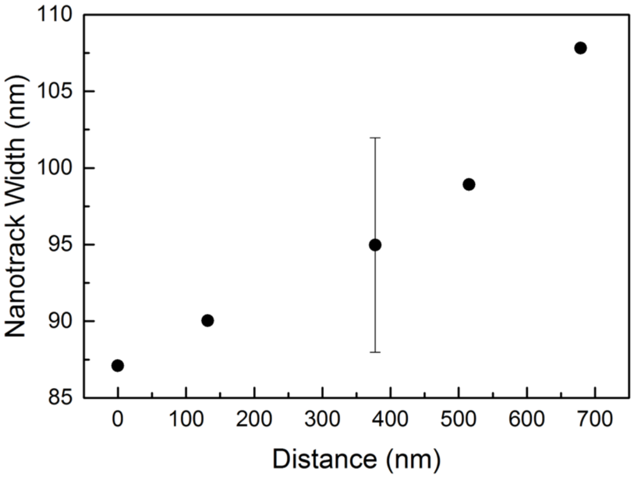

Figure 4-7. Nanotrack width as a function of the distance away from the center of the nanotrack region. The error bar indicates the typical width variation of a nanotrack. The data was obtained on the nanotracks induced by a laser fluence of 9.2 mJ/cm^2.

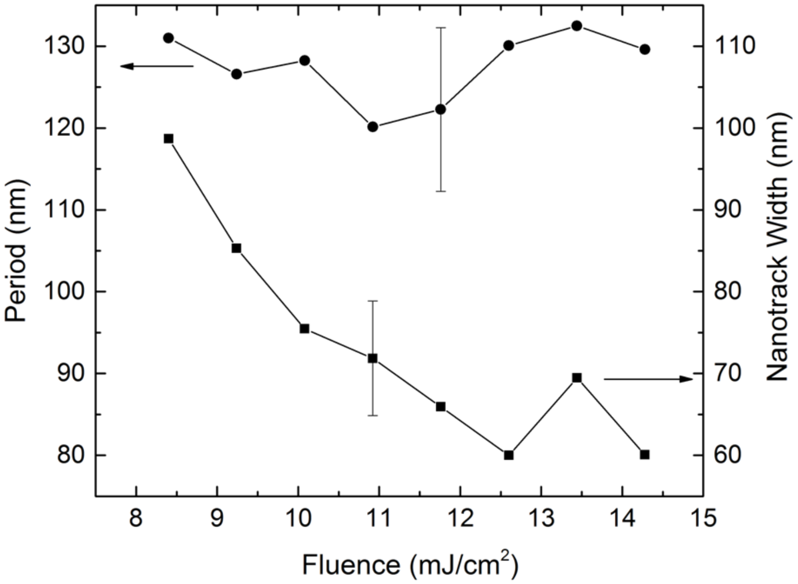

Figure 4-8. The nanotrack period and width in eight nanotrack regions as a function of the corresponding irradiation laser fluence. The width in each region was taken from the center-most nanotrack. The error bars indicate the typical variations in the width and the period.

In addition to laser irradiation by the 1560 nm laser beam, the Sb_2Te_3 thin film samples were also exposed to the 780 nm laser and the 1030 nm laser. For the 780 nm laser irradiation, only limited experiments were performed on a 100 nm Sb_2Te_3 film directly on the Al_2O_3 substrate, with a fluence range of around 10 mJ/cm^2 - 25 mJ/cm^2 and scan speeds ranging from 1 μm/s to 50 μm/s. Examinations of the irradiated regions under SEM revealed only LFSL with a periodicity of about 620 nm, slightly smaller than the laser wavelength, consistent with the previous reports on LFSL. The absence of HFLS in the case of 780 nm laser irradiation could be related to the large photon energy compared to the narrow bandgap of Sb_2Te_3, as was discussed earlier in section 4.1.

Irradiation experiments with the 1030 nm laser were conducted on the same sample as in Fig. 4-5, with a fluence ranging from 4.5 mJ/cm^2 to 13.2 mJ/cm^2 and a scan speed from 5 μm/s to 20 μm/s. The SEM examinations on the irradiated regions not only found ordered nanotracks similar to those produced by the 1560 nm beam (Figure 4-10), but also revealed different regimes of the laser interaction dynamics as the laser fluence varies; one of such examples is shown in Figure 4-9. The area irradiated by the 1030 nm beam (not scanning) displays an oval shape with four regions of different surface morphologies clearly visible. Region 1 corresponds to the center of the Gaussian beam and the highest laser fluence, while region 4 corresponds to the tail of the beam and has the lowest fluence. Similar to the 1560 nm case, the weak fluence at region 4 results in a smoothed surface, likely due to annealing from a slightly raised temperature by the tail of the laser beam. Note the narrow ring of region 3 that constitute only about 10% of the total diameter, demonstrating the limited range of fluence available for generating the ordered nanotracks by the 1030 nm laser.

The effort to observe wide arrays of nanotracks similar to those with the 1560 nm beam is further complicated by the coexistence of LSFL and HSFL. Figure 4-10 shows two laser-irradiated regions with a laser fluence of 6.8 mJ/cm^2 and 7.6 mJ/cm^2, respectively. The nanotracks have an average width of 58 nm and an average period of 90 nm, in good agreement with the empirical relationship of $\lambda/2n \approx 86$ nm for the periodicity ($\lambda = 1030$ nm and $n \approx 6$). These groups of nanotracks are separated by stripes filled with nanoparticles, a characteristic feature of high-fluence irradiation as demonstrated in regions 1 and 2 in Fig. 4-9. This larger periodicity is around 750 nm on average, slightly smaller than the laser wavelength of 1030 nm and indicative of an LSFL nature. The periodic appearance of groups of nanotracks separated by a different surface morphology is reminiscent of a similar LSFL-HSFL mixing in the nanotrack regions irradiated by the 1560 nm laser, where the 45^{o} laser polarization relative to the scan direction revealed an LSFL periodicity of 1.5 μm (Fig. 4-3). In the case of the 1030 nm irradiation, the groups of nanotrack are located near the nodes of the laser intensity modulation, while the nanoparticle regions are located at the antinodes where the fluence is large. Due to the small periodicity of the 1030 nm LSFL (750 nm) compared to the width of the trench (> 2 μm), more than one alternation of these two surface morphologies can appear even with the laser polarization perpendicular to the scan direction.

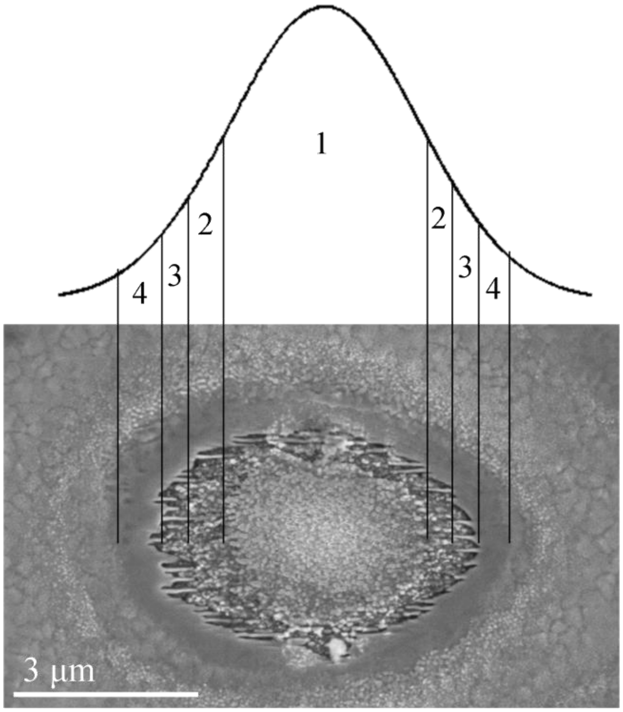

Figure 4-9. An area on the Sb_2Te_3 thin film sample irradiated by the 1030 nm laser beam, showing four regions with different surface morphologies along the beam diameter. The distribution of the morphologies across the laser spot demonstrates a variety of laser interaction regimes linked to different fluence ranges. Only about 10% of the whole range of fluence (region 3) results in nanotrack generation.

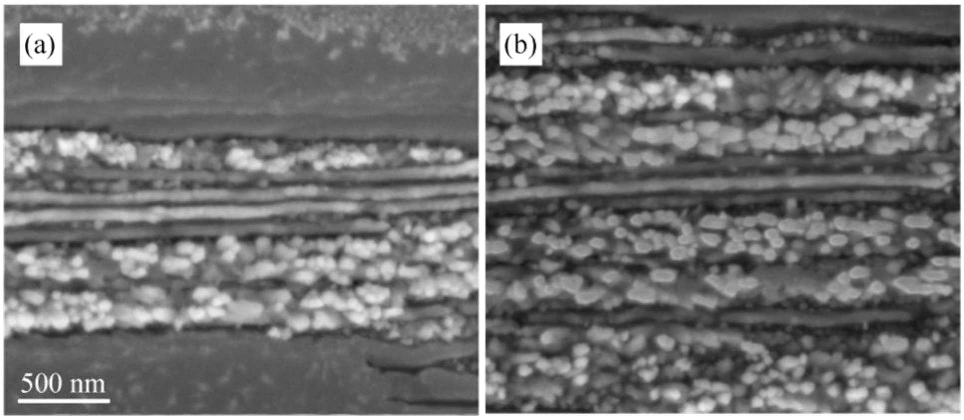

Figure 4-10. Nanotracks induced by the 1030 nm laser with a scan speed of 5 μm/s and a fluence of (a) 6.8 mJ/cm^2 and (b) 7.6 mJ/cm^2. The periodicity of the nanotracks (90 nm) is consistent with an empirical scaling with the wavelength: λ/2n.

4.5 Cross-Sectional Studies

In the previous section, we have characterized the surface morphology of these nanotracks from the plan-view perspective using SEM and AFM. These techniques are commonly employed by researchers in the field of LIPSS, since the statistics from these plan-view studies can be conveniently compared to the available theoretical models and provide a quick confirmation to the matched one. The SEM and AFM studies also require minimal sample preparation before the characterization can be properly performed. This is in sharp contrast to the cross-sectional techniques such as TEM, which entails delicate and time-consuming preparation procedures such as mechanical and ion beam millings and the focused ion beam (FIB) lift-out technique. These advantages enable the SEM and AFM to become the dominant techniques used in LIPSS studies. However, the macroscopic and surface properties obtained from these studies constitute only a fraction of the information contained in the nanostructures. As part of the laser-material interaction, the formation of these nanostructures involves processes inside the bulk that may readily change the crystal structures or the material composition at the nanoscale, properties that may be difficult to probe using surface or macroscopic characterization techniques.

In an effort to reveal these sub-surface properties, a few cross-sectional TEM studies of LIPSS have been performed in a variety of bulk materials, including InP [4.36], diamond [4.18], Si [4.37, 4.38], SiC [4.38, 4.39], quartz [4.40], Ge [4.37], and GaP [4.41]. These investigations have unveiled interesting structural features embedded underneath the surface of LIPSS. In particular, LIPSS in these materials were reported to have an amorphous or polycrystalline layer covering the top of the nanostructures, attributed to the rapid resolidification from a melted phase. However, since these studies were done on bulk samples, the height modulations of the nanostructures were much smaller than the sample thickness. In our case of nanotracks on Sb_2Te_3 thin films, on the other hand, the height modulations of the nanotracks are comparable to the film thickness. The presence of the film/substrate interface near the laser-material interaction region and the specific composition of Sb_2Te_3 can potentially affect the interaction dynamics and result in a cross-sectional structure considerably different from those in the previously reported cases. In addition, an important question still remains from the previous section whether these nanotracks are interconnected near the bottom of the valleys. Although AFM measurements have revealed height modulations smaller than the film thickness, implying a physical connection of the nanotracks near the film/substrate interface, these nanotracks may very well be separated by a different solid phase.

The work in this section aimed to address these questions by examining the cross-sectional structure of the nanotracks with TEM. The general distribution profiles of different phases were elucidated by the HAADF images and EDS element mapping. Identification of specific phases present in the laser-irradiated region was performed with the help of high-resolution HAADF imaging, SAED and NBED. With these combined efforts, a complete and clear picture of these highly-ordered nanostructures was obtained.

The sample used for this study was an Sb_2Te_3 thin film of around 100 nm. A 10 nm buffer layer of Bi_2Te_3 was deposited between the Sb_2Te_3 film and the Al_2O_3 substrate. The presence of the buffer layer resulted in higher quality growth of Sb_2Te_3 and promoted a more continuous generation of Sb_2Te_3 nanotracks, according to empirical experience. The FIB cut was made perpendicular to the orientation of the nanotracks.

Figure 4-11 (a) is an HAADF image showing an overview of the nanotracks region. Figure 4-11 (b) and (c) are the close-up views of (a) at different locations. The bright spots correspond to the locations of the nanotracks while the darker regions between them correspond to the valleys between the tracks. The black region at the bottom is the substrate. The grey region at the top is the protective Pt layer. The layer of about 10 nm in thickness right on top of the substrate corresponds to the Bi_2Te_3 buffer layer. In Figure 4-11 (c), it appears as a brighter band compared to the nanowire on top of it, due to the heavier Bi atoms compared to the Sb atoms.

One striking feature is that the phase of the nanotracks is extending all the way down to the substrate, separated by a completely different phase in between. In this sense, what we have previously called "the nanotracks" and regarded as simply a surface height modulation are in fact individual in-plane *nanowires* of a single phase separated by a different phase. As we will show later, these nanowires have a well-preserved single crystal Sb_2Te_3 structure identical to the one they started with before laser irradiation. The drastic changes in the crystal structure between the nanowires and the excellent preservation of the crystal structure in the nanowire region are a result of the in-plane periodic modulation of the fs laser intensity on a nanoscale. Note the wedge shape near the border of the nanowires and the Bi_2Te_3 layer, which suggests an increased laser intensity near this region compared to that at a different height. While the exact mechanism for the wedge formation still requires additional theory work to elucidate, the laser intensity variations along the height direction (normal to the substrate surface) is closely related to the presence of the Bi_2Te_3/Sb_2Te_3 interface.

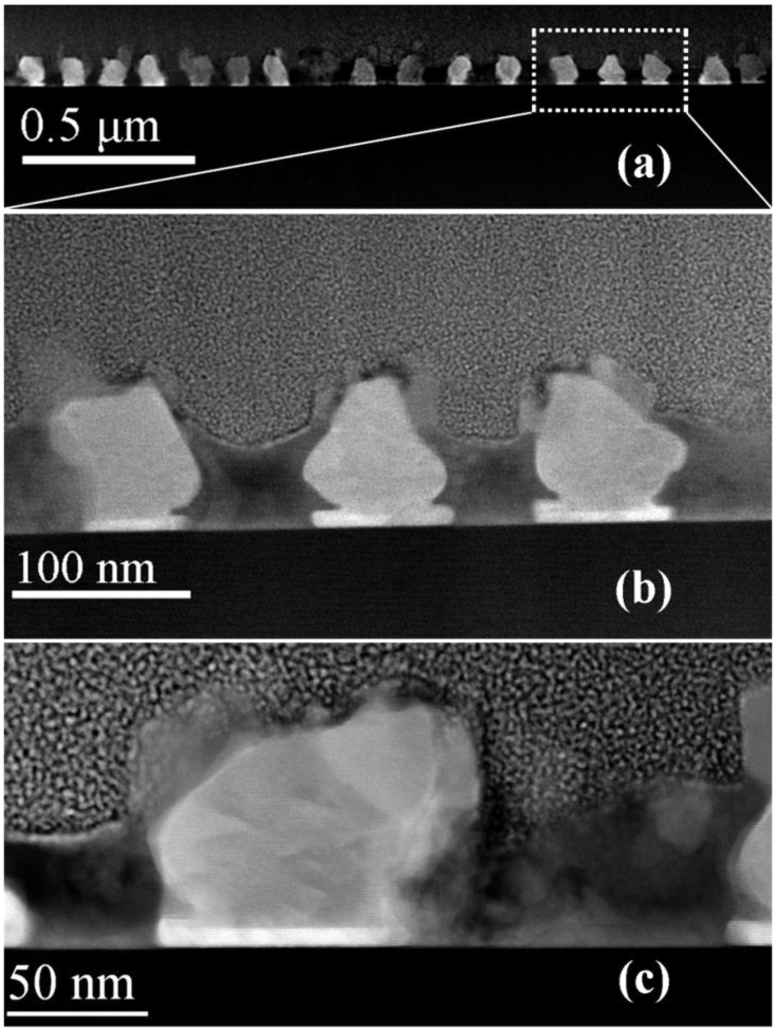

Figure 4-11. HAADF images of the cross section of a nanotrack region. (b) is the zoomed-in view of the region encircled with the dotted rectangle in (a). (c) is the zoomed-in view of another region of the same cross-sectional sample. In (b) and (c), the black region at the bottom is the Al_2O_3 substrate, while the grey region at the top is the Pt protective layer. The white ridges sitting directly on the substrate are the nanotracks, separated by a completely different phase that appear dark grey. Note the thin slabs near the bottom of the nanotracks that seem slightly brighter than the other parts of the nanotrack; these correspond to the Bi_2Te_3 buffer layer. Additionally, (b) and (c) reveal that the top of the nanotracks is covered with a phase different from that of the nanotrack itself.

As a first step to investigate the various phases in the nanowire region, EDS element mapping was carried out over potential candidates originally present in the sample, including Sb, Te, Bi, O, and Al (Figure 4-12). Comparison between the SE image and the Te map shows that

Te is completely missing from the valley regions connecting the nanowires. Meanwhile, the Sb map shows no significant variation in Sb from the nanowires to the valleys. This implies that while the nanowires may still maintain the stoichiometry of the original Sb_2Te_3, the composition of the valley region is considerably altered. The Bi map further reveals that Bi atoms, too, were removed from the valley regions along with Te. The exact process of how the Te and Bi atoms leave the valleys is an interesting topic in itself that warrants further studies with the help of simulations. The Sb in the valley regions, on the other hand, is accompanied by a small trace of O, as indicated in the O map. Therefore, some form of antimony oxide is expected in these regions. Furthermore, as can be seen from both Fig. 4-11 and the SE image in Fig. 4-12, the top of the nanowires are not totally exposed, but instead are covered with a capping layer < 10 nm in thickness. A careful comparison between the shapes of the nanowires in the SE image and element distributions in the Te and Sb maps suggests that part of the capping layer is rich in Te and deficient in Sb.

To further identify the phases present in both the nanowires and the valley regions connecting them, HRTEM (3011) was employed to perform a closer examination at the crystal structures in these regions. Figure 4-13 displays six different regions, including the nanowires, the valleys and their borders, with sub-nanometer resolution. Fig. 4-13 (a) is a small area in the center of the nanowire, with a d-spacing of 1.01 nm, in excellent agreement with that of the Sb_2Te_3 phase along the c-axis [4.42, 4.43]. Fig. 4-13 (b) shows a region near the top of a valley with a d-spacing of 0.64 nm. This matches well with the (111) planes of the Sb_2O_3 cubic phase [4.42, 4.44], one of the candidates in the valley region according to the EDS element maps. Fig. 4-13 (c) and (d) show two borders between the nanowire and the valley, again with a d-spacing of 1.01 nm for the nanowire and 0.64 nm for the valley. Note the presence of several crystal grains in the valley region, in sharp contrast to the single crystalline lattice in the nanowire. Fig. 4-13 (e) displays the capping layer on top of a nanowire that was determined by the EDS maps to be Te-rich and Sb-deficient. Two orthogonal d-spacings, 0.22 nm and 0.59 nm, could be identified in this region, matching perfectly with the (110) and (001) planes of the hexagonal Te phase [4.42, 4.45]. Fig. 4-13 (f) shows a border between a nanowire, a valley and the Pt protective layer. The nanowire has a lattice spacing consistent with that of Sb_2Te_3, as before. The valley started off (lower-right corner of the image) with two orthogonal d-spacings of 0.64 nm and 0.27 nm, in agreement with the (111) and the (400) planes of the Sb_2O_3 cubic phase. Moving towards the top of the nanowire, these two d-spacings are replaced with one visible spacing of 0.59 nm, characteristic of the (001) plane of Te hexagonal phase. These images reveal an interesting distribution of various phases: nanowires composed of Sb_2Te_3, a high concentration of Sb_2O_3 in the valley regions between the nanowires, and a trace of crystalline Te in the capping layer on top of the nanowires.

To acquire a closer view of the crystal structure, STEM was used for a more detailed examination of the atomic arrangements. Figure 4-14 presents the HAADF images of (a) a nanowire and (b) a valley region between the nanowires. Fig. 4-14 (a) reveals a layered single crystal structure with a distinct periodicity of around 1 nm in the vertical direction separated by van der Waals gaps, in good agreement with the lattice parameter of Sb_2Te_3 along the c-axis. A close-up view in Fig. 4-14 (c) reveals a more detailed crystal structure of the nanowire, with each periodicity consisting of five atomic layers (quintuple layers). The distance between the adjacent atoms perpendicular to the c-axis is 2.1 Å, consistent with the (110) planes of Sb_2Te_3. This confirms that the nanowires indeed maintain the same single crystalline Sb_2Te_3 tetradymite structure as before the intense laser irradiation.

Meanwhile, the phases in the valley region between the nanowires appear more chaotic with several crystal grains clearly visible (Fig. 4-14 (b)), an observation similar to that in Fig. 4-13 (c) and (d). As an example, a zoomed-in view on the upper right corner of Fig. 4-14 (b) shows a hexagonal-like and a rectangular arrangement of the atoms in the plane (Fig. 4-14 (d)). These two patches of crystal grains agree well with the (011) and $(1\bar{1}\bar{2})$ planes of cubic Sb_2O_3 [4.42, 4.46].

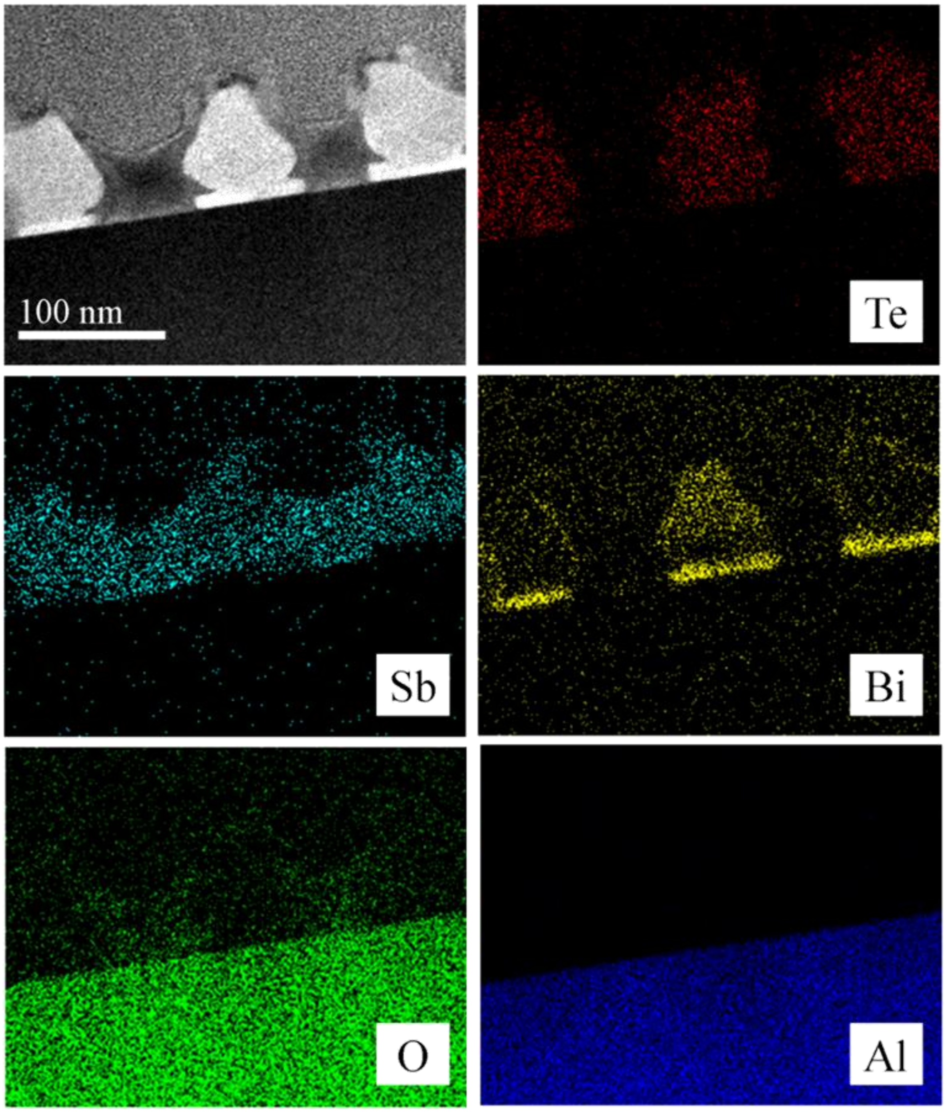

Figure 4-12. EDS element mapping of Te, Sb, Bi, O, and Al. The image at the upper-left corner is the SE image taken at the same location as the maps. Comparison between the SE image and the Te map shows that while there is Te in the nanotracks, Te is completely missing from the regions between the nanotracks (the valleys). Meanwhile, the Sb and O maps point to the existence of Sb and O elements in the valley regions. Note that the apparent abundance of Bi in one of the nanotracks is not representative of the other regions in the same cross-sectional sample.

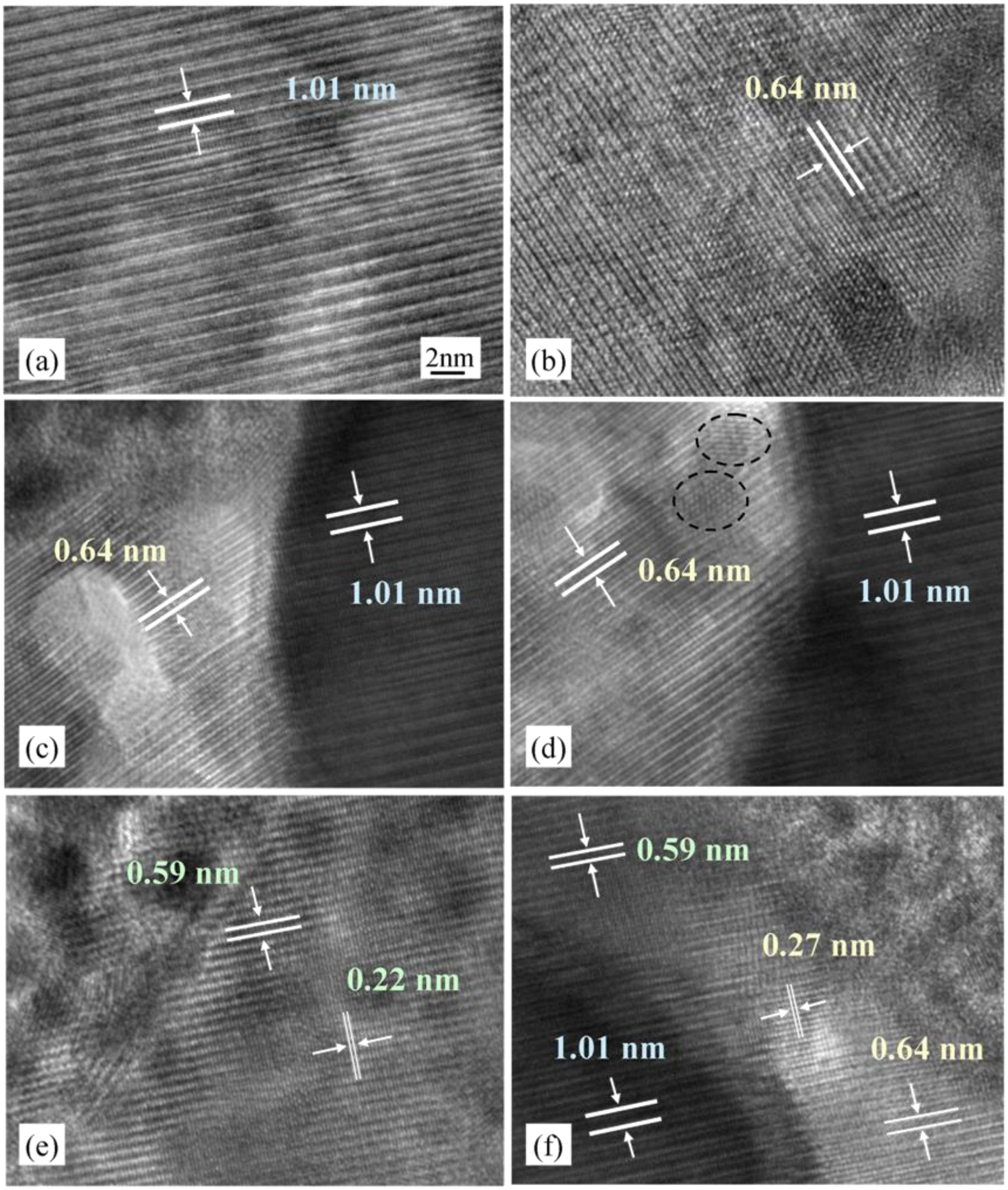

Figure 4-13. HAADF images of the nanotrack and valley regions with the 3011 HRTEM. (a): a nanowire region, (b): a valley region, (c) and (d): a border between a nanowire and a valley, (e): the top of a nanowire, (f): the top-corner of a nanowire. The two dashed ellipses in (d) highlight two visible crystal grains with different orientations. The upper left corner in (e) and the upper right corner in (f) are regions of the Pt protective layer.

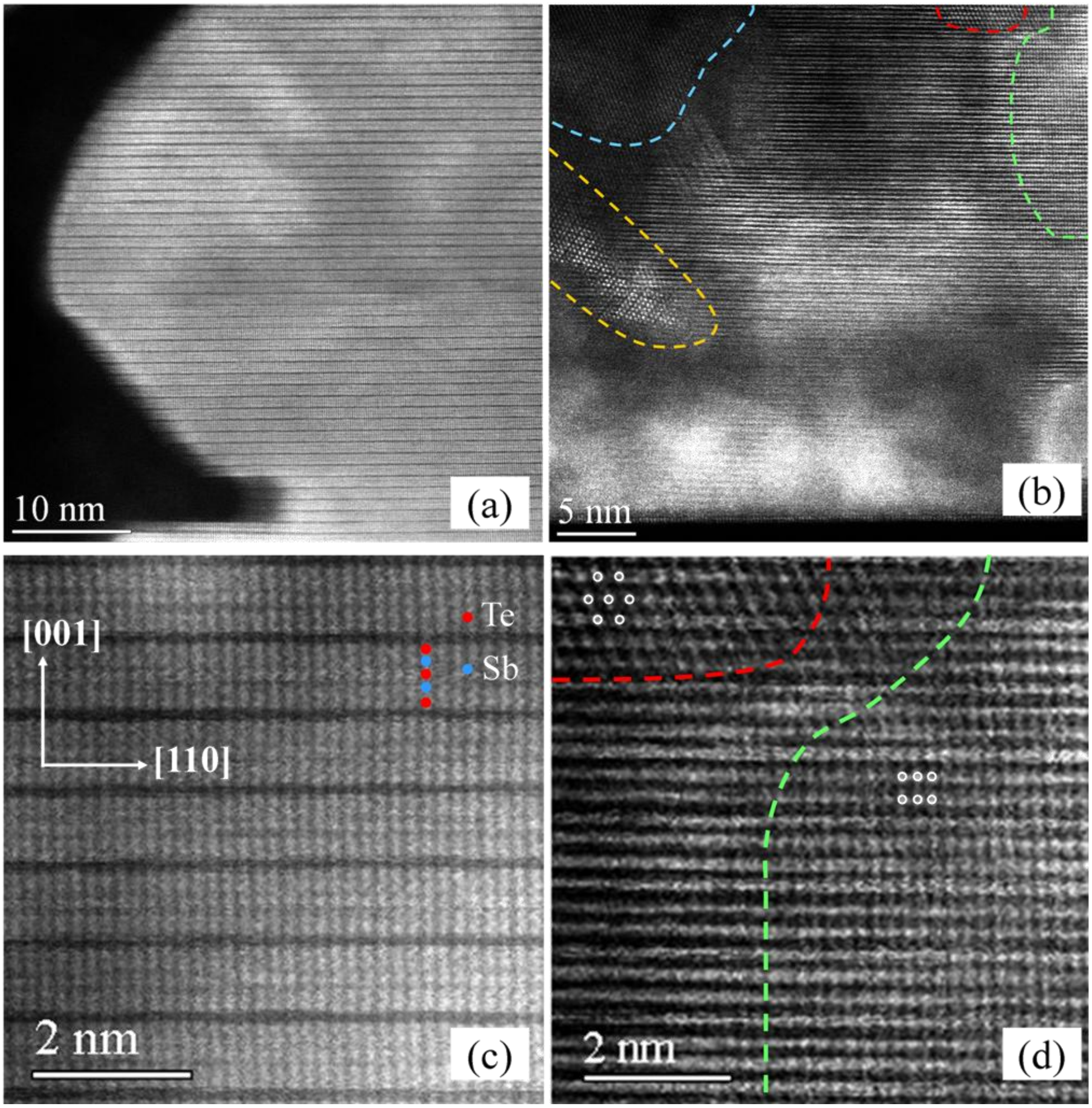

Figure 4-14. HAADF images of a representative nanowire (a) and the region separating the nanowires (b). (c) and (d) are the zoomed-in views of (a) and (b), respectively. Note the dark lines in (a) and (c), corresponding to the van der Waals gaps in Sb_2Te_3 crystal. (a) and (c) demonstrate that the nanowires remain the pristine Sb_2Te_3 single-crystal structure, with the c-axis being normal to the substrate and the a-axis along the nanowire length. The blue and red dots in (c) indicate the locations of the Te and Sb atoms in the nanowire. (b) shows the polycrystalline phase of a valley region between nanowires, where four patches of crystal grains are highlighted with the colored dashed lines. (d) is the zoomed-in view of the upper right corner of (b), showing two Sb_2O_3 crystal grains (encircled with the red and green dashed lines) with their corresponding atomic arrangements outlined by the white open circles.

In addition to analyzing the HAADF image, SAED was performed to identify the phases from a 3D perspective. This was first conducted on the substrate and the smooth film regions (Fig. 4-15) to establish a calibrated relationship between the distance on the detector screen and the actual d-spacing. The (110) and the (003) planes of Al_2O_3 and Sb_2Te_3 were used for the calibration. The SAED measurements were then performed on several nanostructured regions. Figure 4-16 (a) shows the range of area analyzed by the SAED after the narrowest aperture was used for area selection. The small feature size of the nanowires compared to the aperture diameter leads to complications in analyzing the electron diffraction pattern, with diffraction peaks from the nanowires, valleys, Pt and the substrate all mixed together in the same pattern (Fig. 4-16 (b)). The polycrystalline Pt layer produces diffraction rings (Fig. 4-16 (b)) with d-spacings of 2.29 Å, 1.93 Å, 1.41 Å, and 1.19 Å, corresponding to its (111), (200), (220) and (311) planes [4.42]. The d-spacings of the new diffraction peaks that appear only in the nanostructured regions were measured. Figure 4-16 (b) shows an example of six new bright dots (encircled) all with a d-spacing of 3.2 Å, suggesting the presence of several Sb_2O_3 crystal grains with different orientations. After the new peaks were identified and their d-spacings measured in each diffraction pattern, candidate phases were assigned to each value. Table 4-1 lists the four phases I was able to determine from the measured d-spacings: cubic Sb_2O_3, rhombohedral Sb, cubic Sb, and hexagonal Te. Out of these four, only Sb_2O_3 and Te show up consistently in all the patterns, and multiple planes corresponding to either of these two phases were observed in good agreement with the known values. In contrast, only two diffraction peaks match the cubic Sb [4.42, 4.47] and one for the rhombohedral Sb [4.42]. For the cubic Sb, its small cell size may account for the scarcity of matching peaks in Table 4-1, since interpretations of smaller d-spacing values can become increasingly ambiguous as more phase candidates have planes near the experimental values. The rhombohedral Sb, however, has prominent d-spacings above 2.15 Å [4.42]. Their absence in all the electron diffraction patterns could be an indication that this particular phase is in a negligibly small amount in the whole nanostructured region.

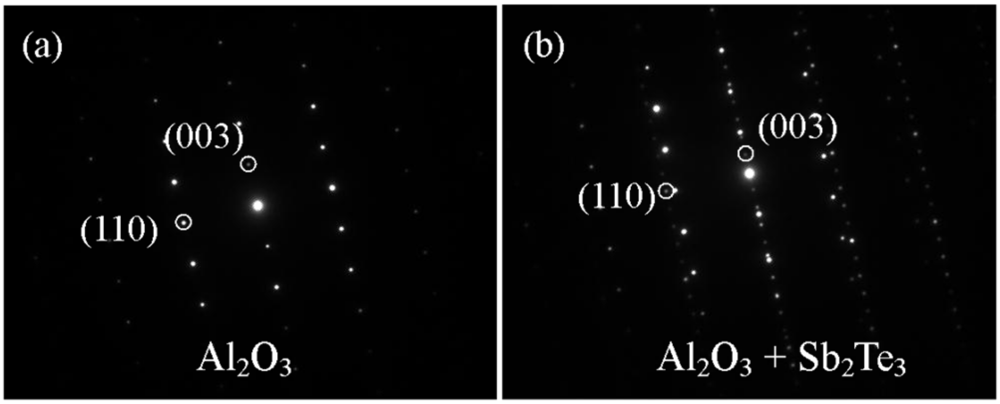

Figure 4-15. SAED patterns on (a) the Al_2O_3 substrate and (b) the smooth film region. The circles highlight the diffraction peaks of the (110) and (003) planes of Al_2O_3 and Sb_2Te_3. These peaks can be used as a calibration gauge for measuring the d-spacings of the additional diffraction peaks that show up in the nanostructured region.

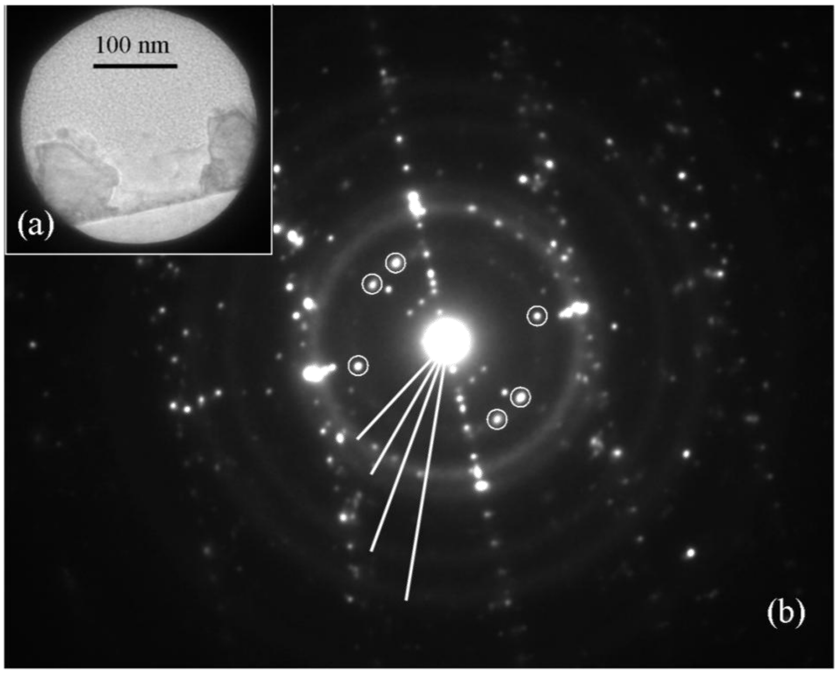

Figure 4-16. SAED performed on the nanostructured region. (a) shows the range of area analyzed by electron diffraction after the aperture for area selection was applied. (b) is the electron diffraction pattern in a selected area, which, based on the size of the aperture, contained both the nanowires and the valleys. The four lines in (b) indicate the d-spacings of the characteristic rings from the polycrystalline Pt layer. The six circles in (b) highlight three different orientations (grains) of an additional diffraction peak that appears in the nanostructured region. This peak corresponds to a d-spacing of 3.2 Å.

Table 4-1. A list of the additional d-spacings from the SAED patterns in the nanostructured regions and the corresponding attributed phases.

Phase / d-spacing (Å)	Sb_2O_3 Cubic	Sb Rhombohedral	Sb Cubic	Te Hexagonal
6.452	6.418 (111)			
5.925				5.927 (001)
3.843				3.856 (100)
3.217	3.209 (222)			
2.973			2.986 (100)	
2.785	2.779 (400)			
2.334				2.35 (102)
2.225				2.228 (110)
2.157		2.152 (110)		
2.111			2.111 (110)	
1.971	1.965 (440)			1.975 (003)

Due to the much larger aperture diameter compared to the nanostructure feature size and the chaotic nature of the phases present in the valley region between the nanowires, nanobeam electron diffraction (NBED) study was conducted on the valleys to separate the mixed signals from the various smaller domains in the global nanostructured region; we examined only the local crystal structures instead. NBED uses a convergent electron beam that focuses into a spot size of around 1 nm, enabling the selective studies of individual crystal grains. With the diffraction pattern from a single phase, the symmetry displayed by the diffraction peaks can be combined with the d-spacing values for a more accurate phase identification. Similar to the SAED, the NBED measurement was first performed on the Al_2O_3 substrate for calibration purpose (Fig. 4-17 (a)). Different spots in the regions connecting the nanowires were then randomly selected for examination. Figure 4-17 (b) - (d) present some of the NBED patterns recorded in the experiments. Among all the recorded patterns, a hexagonal-like arrangement of the diffraction peaks, such as the ones shown in Fig. 4-17 (b) and (c), is the most commonly encountered pattern, accounting for 6 out of 10 patterns with a recognizable symmetry. An evaluation of the corresponding d-spacings of the peaks and the pattern symmetry suggests the cubic Sb_2O_3 phase, with the shorter and longer d-spacings of the hexagonal-like pattern matching the (222) and (400) planes. This is in excellent agreement with Fig. 4-13, where extended areas of crystal grains with a d-spacing consistent with the (111) planes of cubic Sb_2O_3 were observed in the valley regions. With the experimental observations presented so far, we have confirmed the presence of cubic Sb_2O_3 and revealed its prevalence in the regions between the nanowires.

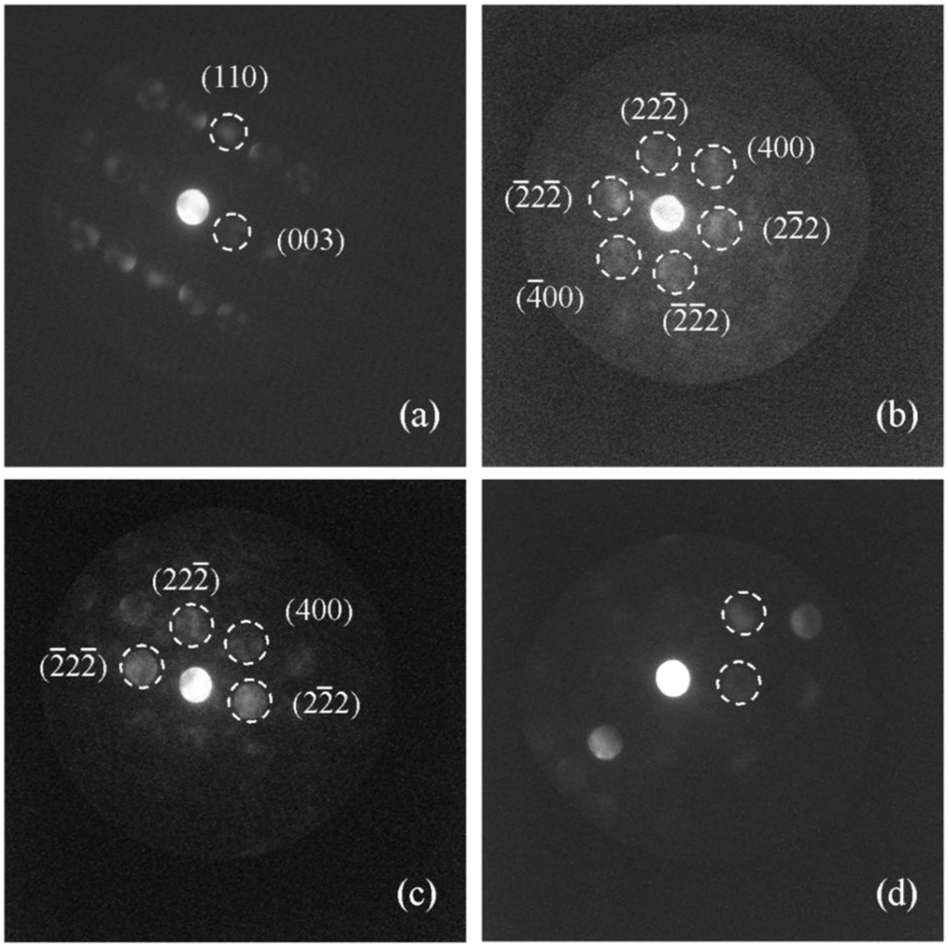

Figure 4-17. NBED patterns on (a) the substrate and (b) - (d) the valley regions. The positions of the diffraction peaks are highlighted with the dashed circles.

While the diffraction patterns with the hexagonal-like symmetry provide an unambiguous identification of the Sb_2O_3 cubic phase due to the unique diffraction pattern of a face-centered cubic crystal in the [011] beam direction compared to that of a simple cubic crystal, the patterns with a square symmetry, appearing in 2 out of the 10 patterns with recognizable symmetry, pose a greater challenge for a conclusive phase assignment. One such example is shown in Fig. 4-17 (d), where the encircled peaks can be assigned to the (400) and (440) planes of cubic Sb_2O_3 or the (100) and (110) planes of cubic Sb. The difficulty comes from the close d-spacing values of the (400) planes of the cubic Sb_2O_3, at around 2.8 Å, and the (100) planes of the cubic Sb, at around 3 Å. The effort to distinguish these two phases in the [001] beam direction is further impeded by the uncertainties associated with measuring the exact distance between the centers of the two adjacent peaks and possible lattice distortion near the grain boundaries. Additional analysis techniques for the NBED patterns are needed in order to gain a more definitive understanding of these two patterns. Finally, the remaining two symmetric NBED patterns point to the hexagonal Te phase, likely inside one of the Te crystal grains near the top of the valley close to the nanowires.

4.6 X-Ray Diffraction Studies

Initially designed to clarify the phases in the laser-nanostructured regions in Sb_2Te_3, the X-ray diffraction (XRD) studies were carried out as an additional characterization technique after the surface morphology examinations. These XRD results will be presented in this section and compared with those in the cross-sectional studies.

The instrument used in these studies was a Bruker D8 Discover X-ray diffractometer with a General Area Detector Diffraction System using a Cu kα source. This diffractometer is equipped with a capillary that provides a small X-ray spot diameter of 500 μm, making it possible to prepare a nanostructured region for XRD examination with minimal signal contribution from the smooth film region. Both the X-ray source beam and the area detector rotated in the θ direction while the sample remained still. The angle of the source beam (θ_1) and the angle of the area detector (θ_2) with respect to the sample surface were set to be approximately the same, each with a movement range of 20^o to 40^o. The solid receiving angle of the area detector is 30^o. The diffraction intensity integrated along the χ direction was recorded as a function of $2\theta = \theta_1+\theta_2$. A 2 mm by 2 mm area covered with nanowires was prepared by scanning the femtosecond laser on an Sb_2Te_3 thin film in a raster style. For comparison, XRD spectra on the non-irradiated regions of the same film were also taken to verify that the new peaks appeared only after nanowires were formed.

The search for the new XRD peaks began with a 2θ scan on both the smooth film and the nanostructured regions with a step size of 0.3^o for θ_1 and θ_2, respectively, across their whole range of movement. The two series of scans were then compared, and the 2θ positions of the peaks that emerge only in the nanostructured region were recorded. A closer examination of these peaks was performed by moving the detector and the source angles to these 2θ positions for data collection with an integration time of 180 seconds.

Figure 4-18 shows three sets of example spectra where new peaks have developed in the nanowire region compared to the smooth film region. The peaks at $2\theta = 26.3^o$, 44.6^o, and 54.2^o that show up in both regions were assigned to the (009), (0015), and (0018) planes of Sb_2Te_3, according to known literature values [4.42]. The new peaks at $2\theta = 27.7^o$, 46.1^o, and 57.6^o were attributed to the (222), (440), and (444) planes of the cubic Sb_2O_3 [4.42]. Note that the hexagonal Te phase also has two XRD peaks in close proximity to 27.7^o and 46.1^o, namely, the (101) planes at 27.56^o and the (200) planes at 47.04^o. However, the cubic Sb_2O_3 was favored in this case due to its better match between the observed and the known peak positions. Fig. 4-18 (b) also reveals a small bump at around 32.1^o, coinciding with the (400) plane of the cubic Sb_2O_3. These XRD results are in superb agreement with the electron diffraction patterns in the previous section, and corroborate the existence of the cubic Sb_2O_3 phase in the laser-irradiated nanostructured area.

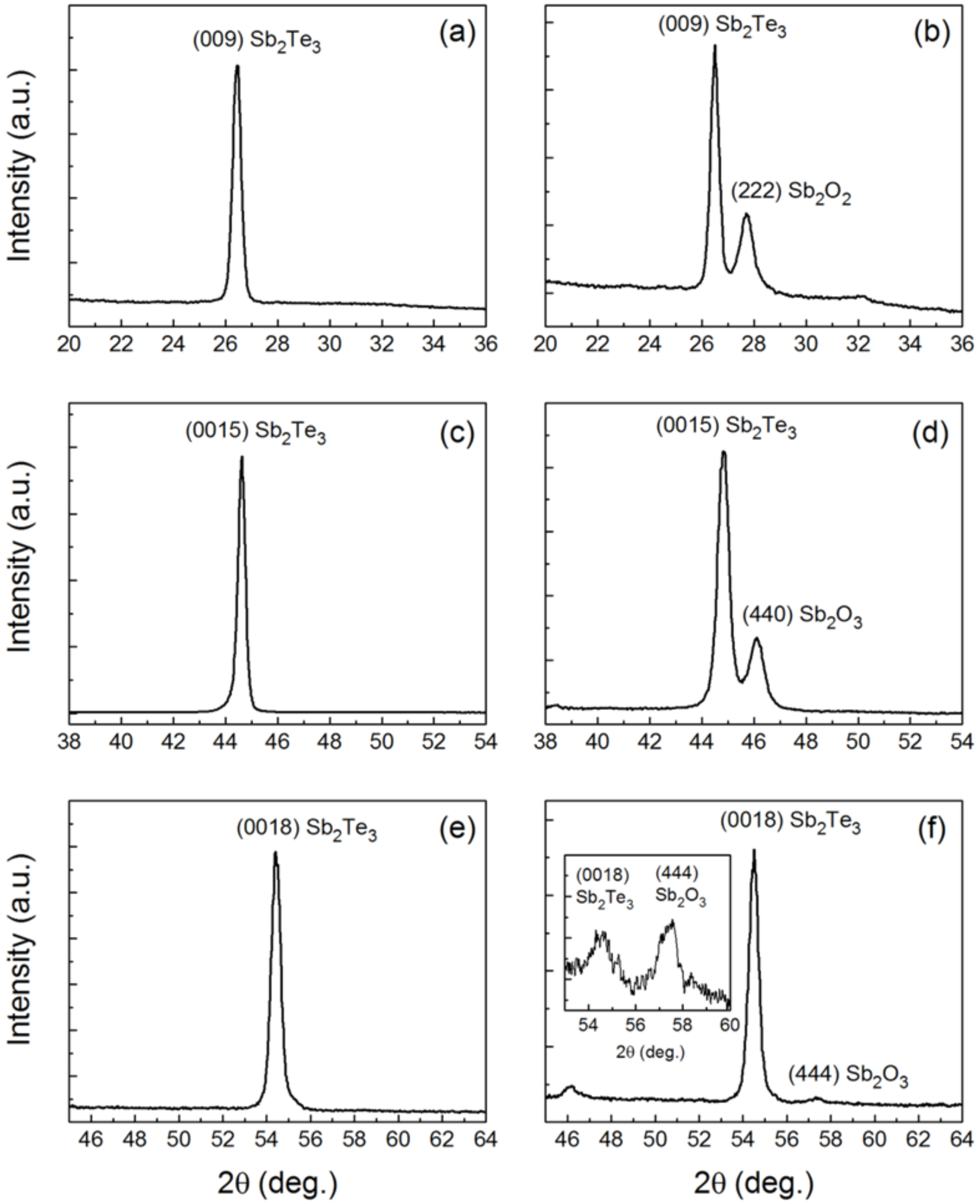

Figure 4-18. XRD scans in the smooth film region ((a), (c), and (e)) and the nanowire region ((b), (d), and (f)), revealing three additional peaks in the nanowire region assigned to the planes of the cubic Sb_2O_3. The center of the area detector was located at: (a) and (b) 27.7^o, (c) 44.2^o, (d) 46.0^o, (e) and (f) 54.5^o, and the inset in (f) 57.4^o. The inset in (f), with $\theta_1 + \theta_2$ coinciding with the location of the new peak, established the bump in (f) around 57^o as a real peak as opposed to background noise.

Table 4-2. 2θ values of additional major XRD peaks in the nanowire region compared to the smooth film.

2θ (deg.)	27.7	38.4	46.1	57.6
Phase	Sb_2O_3	Te	Sb_2O_3	Sb_2O_3
Plane	(222)	(102)	(440)	(444)

While not shown in Fig. 4-18, a fifth new peak at 38.4^o was also detected with an intensity comparable to that of the 57.6^o peak. This peak overlaps with the (102) planes of the hexagonal Te phase. While other weaker peaks of the phases suggested by the electron diffraction measurements may have also shown up in the XRD spectra here, the limited intensity and resolution of the diffractometer used in this work may have swamped them in the background noise. Nevertheless, the complementary results from the XRD studies have greatly strengthened our claim for the ubiquitous presence of the cubic Sb_2O_3 phase and the existence of the hexagonal Te phase in the laser-induced nanostructure area in Sb_2Te_3.

4.7 Influence of the Gas Environment

The previous two sections have provided interesting and important experimental evidence towards answering the following questions: what are the phases in the nanostructured area after intense laser irradiation and how are they distributed spatially? While certain unknowns still remain to be clarified in the above quest, the laser irradiation experiment in different gas environments, presented in this section, represents an ongoing effort to answer another question: what are the processes involved during the fs laser interaction with Sb_2Te_3? It is worth pointing out that due to the complex nature of this subject, the results presented in this section only constitute a small fraction of what is needed to obtain a complete picture of the interaction process. However, these pieces of evidence did provide important insights as to the role of the gas species in terms of the laser-induced nanowire formation in Sb_2Te_3.

In this series of experiments, fs laser irradiations in air, nitrogen and argon were performed with the 1560 nm beam on a ~100 nm Sb_2Te_3 thin film sample with a Bi_2Te_3 buffer layer. A box made of robust poster boards was assembled to create an enclosed space around the laser irradiation site, and the gas was supplied through an opening at the top of the box. Although not strictly air-tight, various measures were taken to ensure a well-controlled gas environment. Edges and corners on the box and between the box and the table were sealed with thick tapes. The optical port for laser entrance was sealed by sticking the linear polarizer against the side wall of the box. Additionally, the openings for the two motorized actuators were taped off to reduce the air pathway. Tapes were also applied on the optics table to cover up the tapped holes. A small flow of the intended gas was applied continuously to create a positive pressure inside the box and minimize the contamination from the outside air.

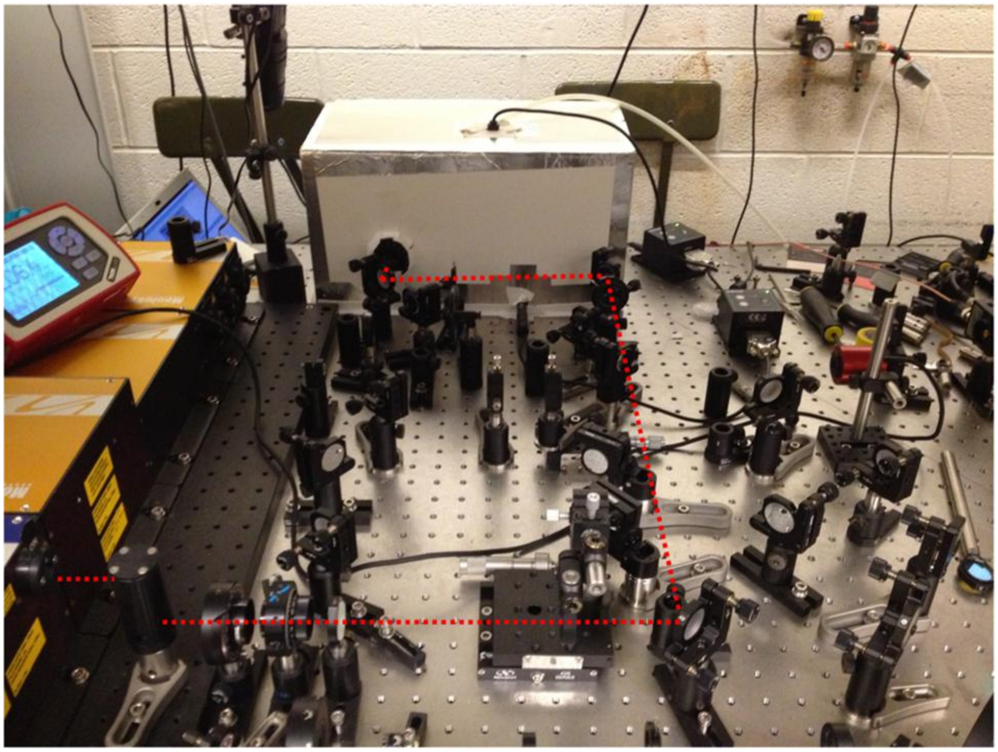

Figure 4-19. Experimental setup for the gas environment studies. The red dotted line highlights the irradiation laser path. The white homemade box serves as a reasonably good confinement to maintain a single type of gas supplied through a tube from the top of the box. The movements of the XYZ translation stage were achieved by the two T-cube motor controllers connected to the two motorized actuators on the stage.

With the linear polarizer on the box during the gas experiments, the real-time laser fluence irradiated on the sample cannot be determined once the box is in place. This poses a challenge for adjusting the laser fluence in the middle of a gas experiment. Therefore, prior to fixing the polarizer on the box, a calibration is necessary to establish the relationship between the half-wave plate reading and the corresponding laser fluence. In this calibration process, the polarizer was in the same position as in Fig. 4-1 (a), and three positions of the half-wave plate corresponding to 12.6 mJ/cm^2, 13.4 mJ/cm^2 and 14.3 mJ/cm^2 were recorded. These three fluences will be used in the gas experiment. The calibration for fluences below 12.6 mJ/cm^2 grew unacceptably imprecise due to the $F \propto \cos^2\alpha$ relationship between the fluence F and the polarization angle coming out of the waveplate, α, relative to the polarizer.

After the fluence calibration was done, the Sb_2Te_3 sample was brought into the focus of the parabolic mirror according to the procedure described in section 4.2. A set of three laser scans was first performed with the above fluences in open air. The polarizer was then mounted onto the laser port on the box in the same polarization angle as in the calibration (vertical to the optical plane), and the box was put into place enclosing the region around the sample. Proper sealing was then performed around the box. The laser irradiation experiments were first done in the air environment inside the box, with no gas feeding necessary. Argon gas was then introduced into the box. A mild gas flow was applied continuously for 15 minutes to flush out the ambient air inside the box, and the laser scanning was subsequently performed. During the laser irradiations, the gas flow was maintained at a minimal level. Additional scanning was done with the gas flow off as a comparison to rule out any effect from possible turbulence created by the flow. The same procedure was followed for the irradiation in the nitrogen environment.

Figure 4-20 shows the results in the three different gas environments, with a laser fluence of 12.6 mJ/cm^2, 13.4 mJ/cm^2,and 14.3 mJ/cm^2 in each case. For the in-air case, parallel nanowires were produced perpendicular to the laser polarization, consistent with the previous observations in this chapter. The slight deviation of their surface morphology from Fig. 4-5 was due to the difference in film quality and thickness in separate rounds of the MBE growth. The morphologies of the nanowires generated in air with and without the box enclosure appeared the same, thus confirming that the presence of the box caused no effect on the surface morphology of the laser irradiated region.

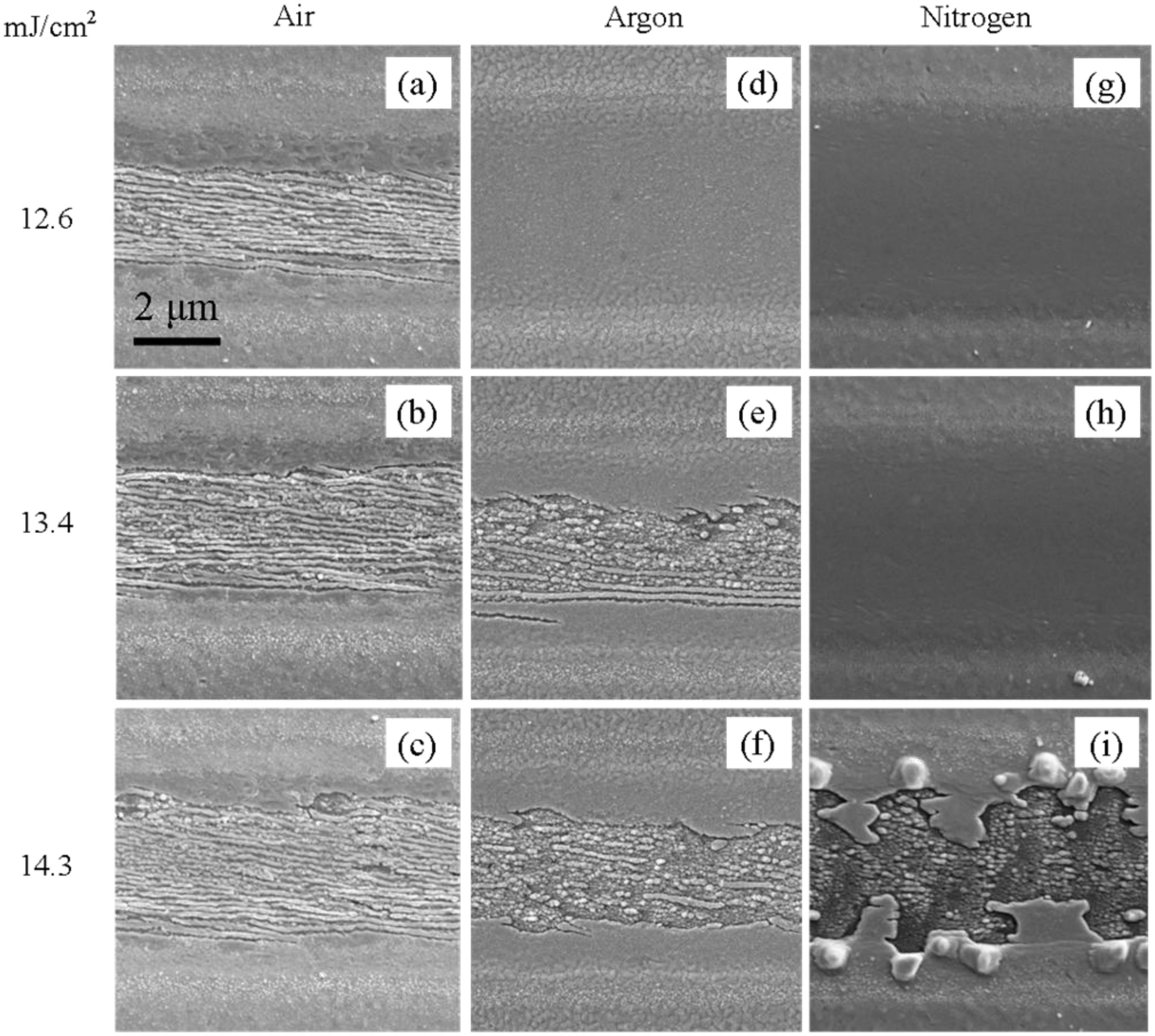

Figure 4-20. Laser irradiations done in (a) - (c): air, (d) - (f): argon, (g) - (i): nitrogen. The laser fluence was 12.6 mJ/cm^2 for (a), (d) and (g); 13.4 mJ/cm^2 for (b), (e) and (h); 14.3 mJ/cm^2 for (c), (f) and (i). The scale bar is 2 μm for all nine images.

The outstanding feature in Fig. 4-20 is the much narrower fluence range of nanowire generation for argon and nitrogen compared to air. While a relatively homogeneous distribution of nanowires can be observed across the scan line for all three fluences for the air case, only a small band of nanowire in the 13.4 mJ/cm^2 case can be observed in laser irradiation in argon. A slightly lower fluence of 12.6 mJ/cm^2 places the sample in the "annealing" interaction regime in Fig. 4-5, signaling an increased threshold for nanowire generation in the argon environment. A similar observation was made in the nitrogen case, where the annealing regime is further pushed to somewhere above 13.4 mJ/cm^2. A closer examination of Fig. 4-20 (i) reveals a direct transition from the complete absence of the Sb_2Te_3 film to the "annealing" regime across the scan line, suggesting that the fluence range corresponding to the nanowire generation may either be extremely narrow, or not exist at all for the nitrogen environment. It is evident, from the comparison between the three gas environments, that the oxygen in the air is playing a critical role in promoting the nanowire formation under a wide range of laser irradiation conditions. The significant involvement of oxygen in the laser-induced nanowire generation process can be inferred from the formation of Sb_2O_3 grains in the laser nanostructure region. On the other hand, the brief appearance of nanowires in Fig. 4-20 (e) and the multitude of reports on HSFL formed in liquids [4.48, 4.49] indicate that the presence of oxygen is not a necessary general condition for nanowire formation. Investigations on how the laser irradiation gas environment plays into the laser-material interaction may shed light on the detailed processes involved in the nanowire formation, not only in Sb_2Te_3, but also other in materials where HSFL were observed.

4.8 Preliminary Measurements

Transient Thermoreflectance Measurements

As an important thermoelectric material, the nanostructured Sb_2Te_3 holds promises for an enhanced thermoelectric performance, evaluated by the dimensionless thermoelectric figure of merit, ZT:

$$ZT = \frac{S^2 \rho}{\kappa} \tag{4.4}$$

where S is the Seebeck coefficient, ρ is the electric conductivity and κ is the thermal conductivity contributed by both the charge carriers and the lattice. Due to the small feature size of these nanowires, a thorough assessment of their thermoelectric performance requires delicate nanoscale measurements involving sophisticated lithography procedures. This is an ongoing research effort and will be discussed in greater detail in the next chapter. Here, we present a brief laser pump-probe study on the cross-plane thermal diffusivity comparison between the nanostructured and the smooth regions on an Sb_2Te_3 film, using the transient thermoreflectance technique introduced in Chapter 2.

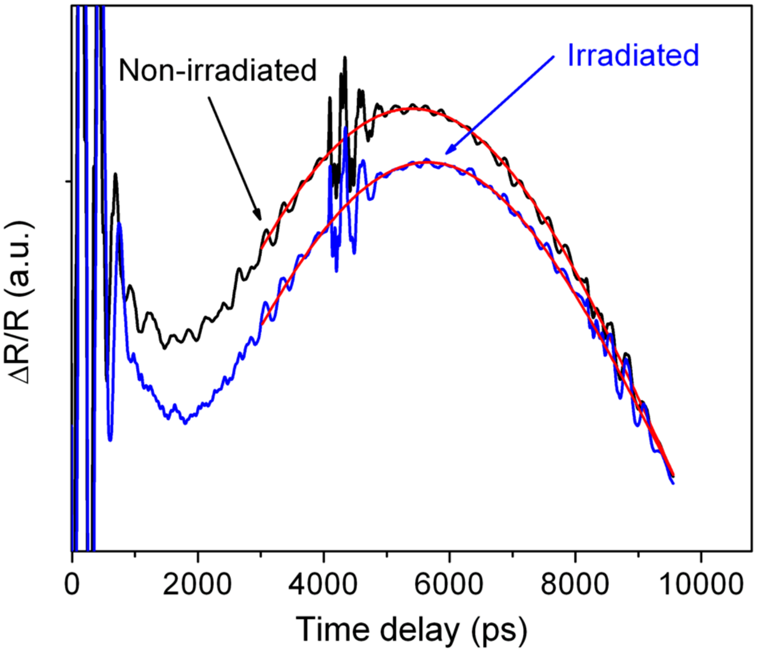

Figure 4-21. Reflectivity curves from the thermoreflectance measurements on a laser-irradiated region (blue) and a non-irradiated region (black) in the Sb_2Te_3 film. The smooth curves are guides to the eye. The thermal diffusion in the laser-irradiated region is noticeably slower than that in the non-irradiated region.

The sample used was a 94 nm Sb_2Te_3 film on a double-side polished Al_2O_3 substrate. First, several regions of the film were irradiated with the 1560 nm fs laser with a fluence of ~ 7.8 mJ/cm^2 and a scan speed of 3 μm/s, within the range of irradiation conditions that results in ordered nanostructures. Then, a 120 nm Al layer was deposited on the film surface to probe the thermal transport in the buried Sb_2Te_3 film. Three laser irradiated regions and three non-irradiated regions were chosen for the measurements.

Figure 4-21 shows the transient thermoreflectance results on the nanostructured (irradiated) and the smooth (non-irradiated) region of the sample. The thermal peak for the irradiated region arrives at a slightly later time compared to that in the smooth film region, suggesting a smaller thermal diffusivity. The thermal diffusivity values for the two cases were calculated according to Eqn. (2.43), and the thermal conductivities were estimated according to:

$$\kappa = D\rho C_p \tag{4.5}$$

where D is the thermal diffusivity, ρ is the density and C_p is the specific heat capacity. The thermal conductivity estimation relies on the assumption that ρ and C_p remain the same after the laser irradiation. From Eqn. (4.5), the thermal conductivity was estimated to be about 0.59 W/m/K for the irradiated region and about 0.62 W/m/K for the non-irradiated region. This corresponds to a difference of 4.5%, which is larger than the statistical variations (3%) within both regions. Note that the thermal conductivity value includes contributions from the transducer-film interface thermal conductivity, charge carrier thermal conductivity and lattice thermal conductivity. In addition, these values may contain influence from the transducer and the probe's penetration depth as discussed in Chapter 2. Data fitting with a thermal transport model is needed to obtain more accurate values of thermal conductivity. Furthermore, while the thermal conductivity estimated from this experiment is in the cross-plane direction, the in-plane thermal conductivity value would be more appropriate considering the orientation of the nanowires. A carefully designed measurement is needed to acquire the in-plane value of κ.

Scanning Tunneling Spectroscopy (STS)

Another experiment on the laser-induced nanowires in Sb_2Te_3 is underway in Prof. Goldman's lab using scanning tunneling spectroscopy along the top surface of the sample. The measurements were performed by Walrath and Lin in Goldman research group, with an instrument uncertainty of 0.1 eV. The STS collected in the smooth film region and the nanowire region is shown in Figure 4-22, where a significantly larger bandgap was observed in the nanowire region. The result is consistent with the cross-sectional observation that a variety of phases other than Sb_2Te_3 are present in the nanostructured region. In particular, the capping layer covering the nanowires may be composed of a mixture of Te and Sb_2O_3, contributing to an increased bandgap. This same capping layer may also be responsible for the absence of the expected periodic modulation of the bandgap as the scanning tip (atomic sharpness) moved across the nanostructured region with alternating Sb_2Te_3 nanowires and Sb_2O_3 valleys. This challenge can be overcome by an additional etching procedure by a mild ion beam or chemicals to remove the topmost 10 nm from the nanostructured region prior to the STS scans. Once the nanowires are exposed, STS will be able to reveal a more accurate band structure in the nanowires and the valleys connecting them.

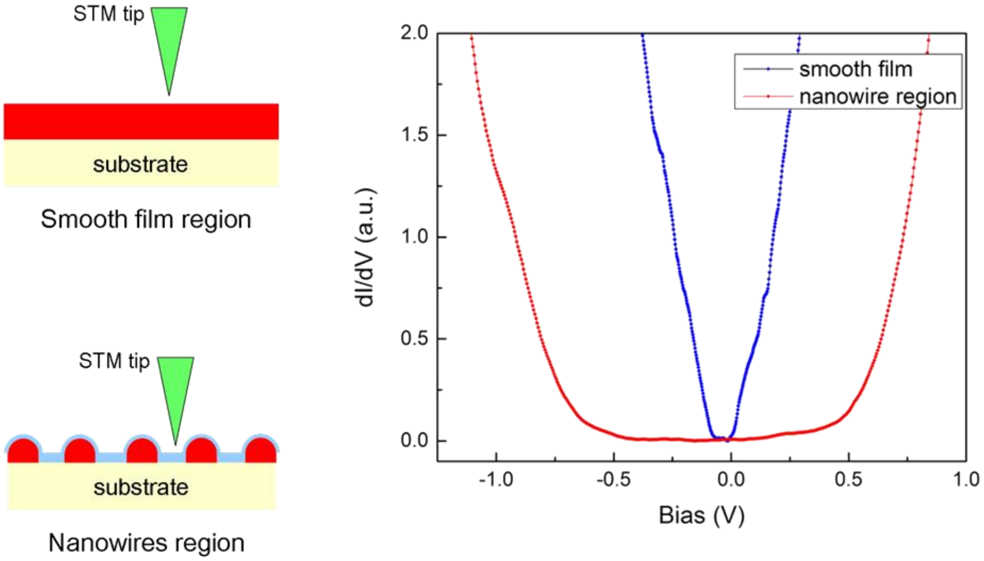

Figure 4-22. Schematic and results of the STS measurements on the nanowire region as compared to the smooth film region. Note the much wider bandgap (>1 eV) in the laser exposed region compared to the unexposed smooth film region. Data courtesy of J. Walrath and Y. Lin from the Goldman research group.

References

[4.1] L. D. Hicks and M. S. Dresselhaus, "Effect of quantum-well structures on the thermoelectric figure of merit", *Phys. Rev. B* **47**, 12727 (1993)

[4.2] L. D. Hicks and M. S. Dresselhaus, "Thermoelectric figure of merit of a one-dimensional conductor", *Phys. Rev. B* **47**, 16631 (1993)

[4.3] Y. M. Zuev, J. S. Lee, C. Galloy, H. Park, and P. Kim, "Diameter dependence of the transport properties of antimony telluride nanowires", *Nano Lett.* **10**, 3037 (2010)

[4.4] H. Zhang, C. Liu, X. Qi, X. Dai, Z. Fang, and S. Zhang, "Topological insulators in Bi_2Se_3, Bi_2Te_3 and Sb_2Te_3 with a single Dirac cone on the surface", *Nature Phys*. **5**, 438 (2009)

[4.5] D. Kong, J. C. Randel, H. Peng, J. J. Cha, S. Meister, K. Lai, Y. Chen, Z. Shen, H. C. Manoharan, and Y. Cui, "Topological insulator nanowires and nanoribbons", *Nano Lett.* **10**, 329 (2010)

[4.6] M. Birnbaum, "Semiconductor surface damage produced by ruby lasers", *J. Appl. Phys.* **36**, 3688 (1965)

[4.7] D. C. Emmony, R. P. Howson, and L. J. Willis, "Laser mirror damage in germanium at 10.6 μm", *Appl. Phys. Lett.* **23**, 598 (1973)

[4.8] N. R. Isenor, "CO_2 laser-produced ripple patterns on Ni_xP_{1-x} surfaces", *Appl. Phys. Lett*. **31**, 148 (1977)

[4.9] G. Zhou, P. M. Fauchet, and A. E. Siegman, "Growth of spontaneous periodic surface structures on solids during laser illumination", *Phys. Rev. B* **26**, 5366 (1982)

[4.10] J. F. Young, J. E. Sipe, J. S. Preston, and H. M. van Driel, "Laser-induced periodic surface damage and radiation remnants", *Appl. Phys. Lett.* **41**, 261 (1982)

[4.11] M. Oron and G. Sørensen, "New experimental evidence of the periodic surface structure in laser annealing", *Appl. Phys. Lett.* **35**, 782 (1979)

[4.12] F. Keilmann and Y. H. Bai, "Periodic surface structures frozen into CO_2 laser-melted quartz", *Appl. Phys. A* **29**, 9 (1982)

[4.13] J. Bonse and J. Krüger, "Pulse number dependence of laser-induced periodic surface structures for femtosecond laser irradiation of silicon", *J. Appl. Phys.* **108**, 034903 (2010)

[4.14] J. F. Young, J. E. Sipe, and H. M. van Driel, "Laser-induced periodic surface structure. III. fluence regimes, the role of feedback, and details of the induced topography in germanium", *Phys. Rev. B* **30**, 2001 (1984)

[4.15] J. E. Sipe, J. F. Young, J. S. Preston, and H. M. van Driel, "Laser-induced periodic surface structure. I. Theory", *Phys. Rev. B* **27**, 1141 (1983)

[4.16] N. Yasumaru, K. Miyazaki, and J. Kiuchi, "Femtosecond-laser-induced nanostructure formed on hard thin films of TiN and DLC", *Appl. Phys. A* **76**, 983 (2003)

[4.17] Y. Shimotsuma, P. G. Kazansky, J. Qiu, and K. Hirao, "Self-organized nanogratings in glass irradiated by ultrashort light pulses", *Phys. Rev. Lett.* **91**, 247405 (2003)

[4.18] E. M. Hsu, N. A. Mailman, G. A. Botton, H. K. Haugen, "Microscopic investigation of single-crystal diamond following ultrafast laser irradiation", *Appl. Phys. A* **103**, 185 (2011)

[4.19] M. Shinoda, R. R. Gattass, and E. Mazur, "Femtosecond laser-induced formation of nanometer-width grooves on synthetic single-crystal diamond surfaces", *J. Appl. Phys.* **105**, 053102 (2009)

[4.20] M. Shen, J. E. Carey, C. H. Crouch, M. Kandyla, H. A. Stone, and E. Mazur, "High-density regular arrays of nanometer-scale rods formed on silicon surfaces via femtosecond laser irradiation in water", *Nano Lett.* **8**, 2087 (2008)

[4.21] G. Miyaji and K. Miyazaki, "Origin of periodicity in nanostructuring on thin film surfaces ablated with femtosecond laser pulses", *Opt. Express* **16**, 16265 (2008)

[4.22] R. Buividas, L. Rosa, R. Šliupas, T. Kudrius, G. Šlekys, V. Datsyuk, and S. Juodkazis, "Mechanism of fine ripple formation on surfaces of (semi)transparent materials via a half-wavelength cavity feedback", *Nanotechnology* **22**, 055304 (2011)

[4.23] X. Jia, T. Q. Jia, Y. Zhang, P. X. Xiong, D. H. Feng, Z. R. Sun, J. R. Qiu, and Z. Z. Xu, "Periodic nanoripples in the surface and subsurface layers in ZnO irradiated by femtosecond laser pulses", *Opt. Lett.* **35**, 1248 (2010)

[4.24] J. Bonse, M. Munz, and H. Sturm, "Structure formation on the surface of indium phosphide irradiated by femtosecond laser pulses", *J. Appl. Phys.* **97**, 013538 (2005)

[4.25] W. Kautek, P. Rudolph, G. Daminelli, J. Krüger, "Physico-chemical aspects of femtosecond-pulse-laser-induced surface nanostructures", *Appl. Phys. A* **81**, 65 (2005)

[4.26] F. Costache, M. Henyk, and J. Reif, "Surface patterning on insulators upon femtosecond laser ablation", *Appl. Surf. Sci.* **208-209**, 486 (2003)

[4.27] D. Dufft, A. Rosenfeld, S. K. Das, R. Grunwald, and J. Bonse, "Femtosecond laser-induced periodic surface structures revisited: a comparative study on ZnO", *J. Appl. Phys.* **105**, 034908 (2009)

[4.28] V. R. Bhardwaj, E. Simova, P. P. Rajeev, C. Hnatovsky, R. S. Taylor, D. M. Rayner, and P. B. Corkum, "Optically produced arrays of planar nanostructures inside fused silica", *Phys. Rev. Lett*. **96**, 057404 (2006)

[4.29] S. K. Das, D. Dufft, A. Rosenfeld, J. Bonse, M. Bock, and R. Grunwald, "Femtosecond-laser-induced quasiperiodic nanostructures on TiO_2 surfaces", *J. Appl. Phys.* **105**, 084912 (2009)

[4.30] R. A. Ganeev, M. Baba, T. Ozaki, and H. Kuroda, "Long- and short-period nanostructure formation on semiconductor surfaces at different ambient conditions", *J. Opt. Soc. Am. B* **27**, 1077 (2010)

[4.31] A. Borowiec and H. K. Haugen, "Subwavelength ripple formation on the surfaces of compound semiconductors irradiated with femtosecond laser pulses", *Appl. Phys. Lett.* **82**, 4462 (2003)

[4.32] R. Le Harzic, D. Dörr, D. Sauer, F. Stracke, and H. Zimmermann, "Generation of high spatial frequency ripples on silicon under ultrashort laser pulses irradiation", *Appl. Phys. Lett.* **98**, 211905 (2011)

[4.33] W. Richter, A. Krost, U. Nowak, and E. Anastassakis, "Anisotropy and dispersion of coupled plasmon-LO-phonon modes in Sb_2Te_3", *Z. Phys. B: Condens. Matter* **49**, 191 (1982)

[4.34] Y. Li, V. A. Stoica, L. Endicott, G. Wang, H. Sun, K. P. Pipe, C. Uher, and R. Clarke, "Femtosecond laser-induced nanostructure formation in Sb_2Te_3", *Appl. Phys. Lett.* **99**, 121903 (2011)

[4.35] The properties of the Sb_2Te_3 thin film samples were provided by the Uher research group.

[4.36] M. Couillard, A. Borowiec, H. K. Haugen, J. S. Preston, E. M. Griswold, and G. A. Botton, "Subsurface modifications in indium phosphide induced by single and multiple femtosecond laser pulses: A study on the formation of periodic ripples", *J. Appl. Phys.* **101**, 033519 (2007)

[4.37] T. H. R. Crawford, G. A. Botton, and H. K. Haugen, "Crystalline orientation effects on conical structure formation in femtosecond laser irradiation of silicon and germanium", *Appl. Surf. Sci.* **256**, 1749 (2010)

[4.38] T. Tomita, R. Kumai, S. Matsuo, S. Hashimoto, and M. Yamaguchi, "Cross-sectional morphological profiles of ripples on Si, SiC, and HOPG", *Appl. Phys. A* **97**, 271 (2009)

[4.39] T. Tomita, T. Okada, H. Kawahara, R. Kumai, S. Matsuo, S. Hashimoto, M. Kawamoto, M. Yamaguchi, S. Ueno, E. Shindou, A. Yoshida, "Microscopic analysis of carbon phases induced by femtosecond laser irradiation on single-crystal SiC", *Appl. Phys. A* **100**, 113 (2010)

[4.40] M. Budiman, E. M. Hsu, H. K. Haugen, and G. A. Botton, "Cross-sectional study of femtosecond laser bulk modification of crystalline α-quartz", *Appl. Phys. A* **98**, 849 (2010)

[4.41] E. M. Hsu, T. H. R. Crawford, C. Maunders, G. A. Botton, and H. K. Haugen, "Cross-sectional study of periodic surface structures on gallium phosphide induced by ultrashort laser pulse irradiation", *Appl. Phys. Lett.* **92**, 221112 (2008)

[4.42] International Center for Diffraction Data: *PDF data base* (2013)

[4.43] O. Madelung, U. Rössler, and M. Schulz, eds. "Antimony telluride (Sb_2Te_3) band structure, energy gap", *Landolt-Börnstein - Group III Condensed Matter* **41C**, 1-6 (Springer Berlin Heidelberg, 1998)

[4.44] C. Svensson, "Refinement of the crystal structure of cubic antimony trioxide, Sb_2O_3", *Acta Cryst.* **B31**, 2016 (1975)

[4.45] O. Madelung, U. Rössler, and M. Schulz, eds. "Tellurium (Te) crystal structure, cell parameters", *Landolt-Börnstein - Non-Tetrahedrally Bonded Elements and Binary Compounds I* **41C**, 1-6 (Springer Berlin Heidelberg, 1998)

[4.46] D. B. Williams and C. B. Carter, *Transmission Electron Microscopy*. Springer US, 2009

[4.47] D. Akhtar, V. D. Vankar, T. C. Goel, and K. L. Chopra, "Metastable structures of liquid-quenched and vapour-quenched antimony films", *J. Mat. Sci.* **14**, 988 (1979)

[4.48] C. Wang, H. Huo, M. Johnson, M. Shen, and E. Mazur, "The thresholds of surface nano-/micro-morphology modifications with femtosecond laser pulse irradiations", *Nanotechnology* **21**, 075304 (2010)

[4.49] G. Miyaji, K. Miyazaki, K. Zhang, T. Yoshifuji, and J. Fujita, "Mechanism of femtosecond-laser-induced periodic nanostructure formation on crystalline silicon surface immersed in water", *Opt. Express* **20**, 14848 (2012)

[4.50] Portions of this chapter were reproduced with permission from Y. Li, V. A. Stoica, L. Endicott, G. Wang, H. Sun, K. P. Pipe, C. Uher, and R. Clarke, *Appl. Phys. Lett.* **99**, 121903 (2011). Copyright 2011, AIP Publishing LLC.

Chapter 5

Conclusions and Future Work

5.1 Conclusions

In this dissertation, we have conducted time-resolved pump-probe spectroscopy studies on epitaxial Sb_2Te_3 thin films using fs lasers and shown element segregation induced by the high-fluence pump laser. Moreover, we showed that the same pump laser could also be used to induce highly-aligned in-plane Sb_2Te_3 nanowires by irradiation of the Sb_2Te_3 thin films, offering a novel "fs laser-scanning" route for convenient fabrication of low-dimensional Sb_2Te_3 nanostructures in a planar geometry. These investigations demonstrate the versatility and effectiveness of fs laser pulses for spectroscopic characterizations in the time domain, and for material modification in the spatial domain. The results also provide experimental evidence and insights for fs laser-induced nanostructural engineering of Sb_2Te_3 films, a technologically important material with a substantial range of current and future applications. The first-time demonstration of highly-ordered Sb_2Te_3 nanowire formation using fs lasers is the most preeminent result, which opens many new pathways for future studies. These include nanostructured thermoelectric materials and low-dimensional topological insulators.

The laser pump-probe setup in this work employed the ASOPS technique, which has a number of distinctive advantages compared to the traditional mechanically-delayed pump-probe approach. These include superior beam alignment stability during the scan, the ability to monitor a much wider range of time scales (100 fs - 10 ns), and the drastically decreased data acquisition time with exceptional signal-to-noise ratio. With ASOPS, three types of dynamics can be studied sequentially, spanning time scales from femtoseconds to nanoseconds: coherent optical phonon, acoustic echoes, and thermal transport. Examples of such studies were presented, along with related experiments and models for the Sb_2Te_3 thin film samples. These time-resolved results have demonstrated the capability and reliability of ASOPS for future pump-probe investigations on dynamics of other materials with similar time scales. These studies are especially significant for investigating the basic mechanisms of energy conversion, in particular the effects of electron-phonon interactions.

One example of dynamics on very short time scales, the coherent optical phonon, was closely investigated in the Sb_2Te_3 thin films to study the high-fluence fs laser-induced phase segregation resulting from intense pump laser irradiation. A series of complementary experiments, including isotropic and anisotropic reflectivity measurement as well as micro-Raman spectroscopy, were employed to study a new coherent phonon peak at ~3.64 THz, appearing after fs laser irradiation, which was identified as a tellurium A_{1g} mode. Comparison of the coherent phonon spectra before and after the high-fluence fs laser irradiation suggests a laser-induced Sb_2Te_3 decomposition and Te segregation. The observed relationship between the A_{1g} phonon amplitude and the laser fluence uncovered a threshold behavior in the growth of the Te oscillator strength as the fluence is increased, and established a fluence value of 2.47 mJ/cm^2 as the start of the Te segregation for our 100 MHz fs laser. These results underline the importance of careful interpretations of the coherent optical phonon spectra obtained on Te-based chalcogenides which are susceptible to both ultrafast and cw laser induced damage.

Near the higher end of our lasers' fluence range (6 - 15 mJ/cm^2), another type of interesting laser-Sb_2Te_3 interaction was investigated: fs laser-induced nanostructure formation. These nanostructures consist of highly-ordered tracks (termed nanotracks/nanowires/HSFL in Chapter 4) with a periodicity an order of magnitude below the laser wavelength. While similar fs laser-induced periodic surface nanostructures have been observed before, those were predominantly reported in dielectrics and wide-bandgap semiconductors that are weakly absorbing and have bandgaps that exceed the irradiation photon energy. Our work reported here in the fs laser-induced periodic nanostructures, represents the first effort to extend such studies to the narrow bandgap Sb_2Te_3, which is strongly absorbing at the laser irradiation wavelength. Due to the important role of Sb_2Te_3 in thermoelectrics, nonvolatile memory storage and topological insulator studies, these ordered nanotracks make an attractive candidate for low-dimensional nanostructure research and applications.

A closer examination of the surface morphologies of these nanotracks revealed a slight decrease in the track width as the laser fluence increases (98 nm for 8.4 mJ/cm^2 and 60 nm for 14.3 mJ/cm^2). Combined with the observation that the nanotrack orientation is always perpendicular to the laser polarization, these results have suggested control over the morphology of these nanotracks by the laser field. AFM measurements on these nanotracks demonstrated a height modulation of less than 40 nm. Taking into account the total film thickness of ~ 100 nm, this implies that the valleys between the nanotracks do not extend physically all the way to the substrate. Moreover, a careful measurement of the width of the nanotrack region formed by six different laser fluences shows a constant formation threshold for the nanotrack morphology, below which a smoothened surface is formed instead.

Laser nanostructuring experiments were also performed with 780 nm and 1030 nm fs laser wavelengths, with the same repetition rate and comparable irradiation conditions, in an effort to establish the nanotrack dependence on the laser wavelength. No nanotracks were observed after irradiation by a 780 nm fs laser, likely due to the much higher photon energy compared to the bandgap of Sb_2Te_3. The 1030 nm laser, on the other hand, produced nanotracks with a periodicity consistent with a $\lambda/2n$ empirical relationship. Similar to the case of 1560 nm laser irradiation, a variety of surface morphologies following the spatial profile of the laser beam could be observed on the Sb_2Te_3 film. These correspond to different laser-Sb_2Te_3 interaction processes under various fluence regimes. Among these fluence regimes, a narrow range (6.8 mJ/cm^2 to 7.6 mJ/cm^2 with a scan speed of 5 μm/s) corresponding to the nanotrack formation was identified.

The impending questions of which phases are present and how they are distributed in the laser-nanostructured regions were addressed by cross-sectional transmission electron microscopy (TEM) and X-ray diffraction (XRD) studies. A variety of TEM techniques was employed for the investigations, including high-angle annular dark field imaging, selected area electron diffraction and nano-beam electron diffraction. These careful examinations and evaluations have revealed single-crystalline Sb_2Te_3 nanotracks extending all the way to the substrate, separated by valley regions filled with a mixture of largely insulating polycrystalline phases connecting the nanotrack ridges. Thus, the nanotracks reported earlier by us could be identified as individual horizontal nanowires in the present experiments. Electron diffraction identified a major part of the polycrystalline phase between the nanowires as cubic Sb_2O_3, traces of which have also been detected in our earlier coherent phonon and micro-Raman studies. The presence of both cubic Sb_2O_3 and Te was further corroborated by the XRD data. Our results have revealed for the first time an alternating pattern of a conductive single-crystalline nanostructures separated by a more insulating polycrystalline mixed phases following fs laser irradiation of thin films. These observations not only provide new experimental evidence for the laser nanostructuring research community interested in fs laser interactions with narrow-bandgap semiconductors, but they also suggest a new method for producing horizontal Sb_2Te_3 nanowires via fs laser scanning in air.

The exploration of the fs-induced nanostructures grew more compelling as the strong dependence of their surface morphology on the gas environment was unfolded. The ambient oxygen was found to play a critical role in promoting a consistent formation of ordered nanowires under a broad range of laser fluences. This is in stark contrast with laser irradiation performed in argon and nitrogen, which showed limited or no observable fluence range that corresponds to nanowire formation within our laser power limit. This highlights the role of nanoscale chemical reactions in forming the observed laser-induced structures. This was not previously reported to our knowledge and is significant because it shows that chemical processes are involved in the nanowire formation, stimulated by the ultrafast laser irradiation.

5.2 Future Work

The femtosecond laser interaction with the Sb_2Te_3 films involves a mixture of complex processes on different time scales that possibly vary under different irradiation conditions, as suggested by the experimental evidence presented in this work. Following our observations in both fs laser-induced element segregation and ordered nanostructure formation, perhaps the most fascinating question is: what is the formation mechanism? To provide an answer would require a collaborative effort combing both theoretical and experimental aspects. For the former, simulations that can incorporate both the short and long time-scale dynamics, such as plasmonic excitations, chemical interactions, and thermal processes, would be illuminating. For the latter, the experimental results presented in this work have offered some possible directions for gaining more insights on the nanostructure formation mechanism.

The gas environment laser-nanostructuring experiments have already suggested that it is the oxygen in the ambient air, instead of the nitrogen, that promotes the nanowire formation. Note that pulsed laser irradiations on Ti, Al, and stainless steel performed in air, nitrogen, argon, oxygen and vacuum have been reported [5.1-5.6]. While no nanowires or high-spatial-frequency periodic nanostructures were formed on these metals, more extensive reactions with the gas species were observed in an oxygen environment compared to other gases or vacuum, and surface roughening was more prominent in the reactive environments than in the inert ones. Thus, periodic nanostructure formation could be related to the appearance of oxides in the material. Femtosecond laser irradiation on Sb_2Te_3 and other tellurides in pure oxygen may yield novel morphologies and facilitate continuous nanowire formations under laser irradiation conditions or on materials where nanowires were not able to form otherwise.

Another noteworthy clue for the formation mechanism of these ordered nanowires is the consistent observation that the presence of defects promotes the formation of these nanostructures. Figure 5-1 shows three examples of ordered nanowires formed near a scratch or a surface impurity. The smoothened surface surrounding the defects indicates that the laser irradiation condition is below the threshold for nanowire formation, thus suggesting that these scratches or impurities either lower the formation threshold, or serve as the formation trigger mechanism themselves. A related observation was made in SiC where a rougher sample surface lowers the formation threshold for the periodic nanostructures [5.7]. In addition, ordered nanostructures have been reported to form preferentially inside the cracks in SiC, and this was attributed to Mie scattering from the surface defects with the electron density remaining low [5.8]. In our case, the irradiation laser photon energy is considerably above the bandgap of Sb_2Te_3, and therefore the analysis from [5.8] does not quite apply. Nevertheless, Fig. 5-1 suggests that the presence of defect boundaries in Sb_2Te_3 may enhance the laser field and lead to nanowire formation. A more systematic study combined with simulations that incorporate the particular geometries of the surface imperfections would likely shed light on the mechanism at work.

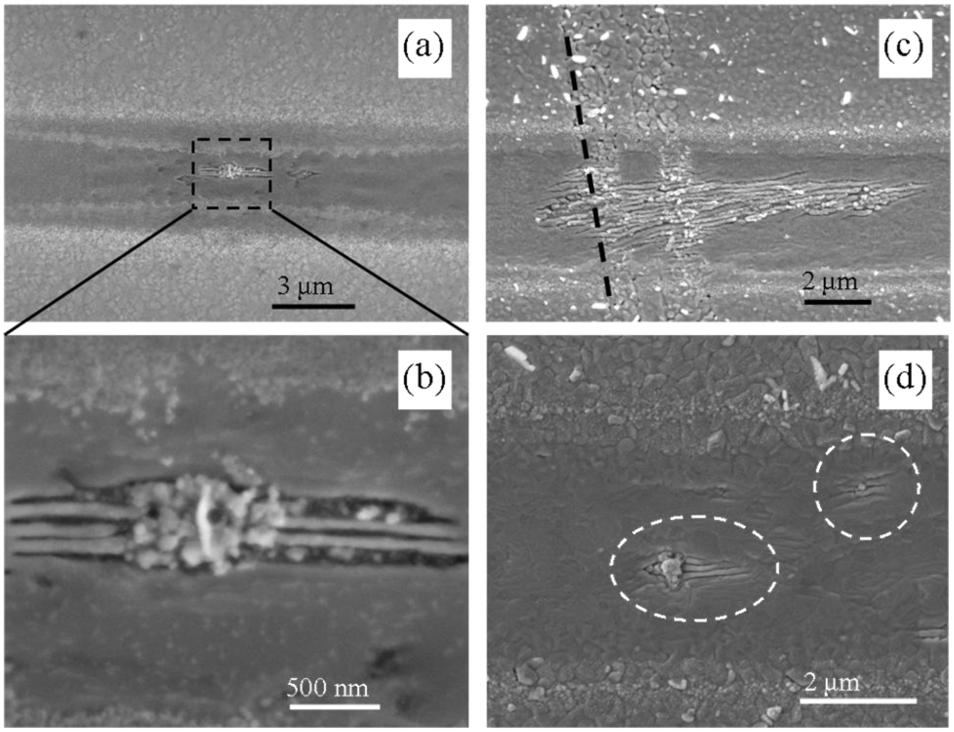

Figure 5-1. Ordered nanowires near defects irradiated by fs lasers below the fluence threshold on Sb_2Te_3 thin films. (a) and (b) show nanowires near a surface particle irradiated by the 1030 nm fs laser. (c) shows nanowires forming near two surface scratches; the black dashed line indicates the direction of the scratches. (d) shows two groups of nano-ripples (highlighted by the two white dashed circles) near two small specks of dust. (c) and (d) were irradiated by the 1560 nm laser. The laser-scanned lines in (c) and (d) show a smoothed surface characteristic of those just below the nanostructure formation threshold.

Besides the more fundamental aspect of nanowire formation, their potential applications in a vast range of areas, including thermoelectrics [5.9, 5.10], nano-spintronics [5.11, 5.12], nano-sensors [5.13, 5.14] and optoelectronics [5.15, 5.16], also provide a variety of opportunities for further exploration. In particular, horizontal nanowires lying directly on top of a substrate are highly desirable for convenient integration within planar nano-devices and optical components [5.17, 5.18]. The fs laser-induced highly-ordered nanowires presented in this work offer a potentially promising alternative to the frequently employed solid-vapor-liquid synthesis method [5.19], which requires an additional delicate process to lay down the nanowires; also, the top-down high-resolution lithography approach, which again involves intricate and cost-intensive procedures, may be conveniently supplanted by these scalable ultrafast laser modification techniques.

The Sb_2Te_3 nanowire array's transport properties such as electrical conductivity and Seebeck coefficient can be measured via the four-terminal configuration, where the outer pair of terminals supplies a current and the inner pair of terminals measures the voltage difference. For Seebeck coefficient measurements, a temperature gradient can be applied on the substrate of the thin film sample. Due to the much larger thermal conductivity of the Al_2O_3 substrate compared to the Sb_2Te_3 thin film, the temperature gradient along the Sb_2Te_3 nanowires will be primarily determined by that along the substrate underneath. For nanowires located far away from the heater and the heat sink, the temperature gradient will be approximately constant, and the temperature difference between a specified pair of points with a known distance along the nanowire can be calculated using the proportionality relation. Such thermoelectric measurements can be carried out using the specially-designed probe station in air for convenient assessments [5.20], or inside a Dewar container for temperature dependence measurements [5.21].

The challenge associated with these measurements lies in the small feature size of the nanowire arrays and with the large thermal conductivity of the substrate. With the current irradiation condition, which has yet to be optimized, a width between 1 μm and 2 μm (5-20 nanowires) and an average length of less than 15 μm is common for continuous bunches of aligned nanowire arrays. To perform the transport measurements on such a small scale would require processes such as electron beam lithography for the precise isolation of the nanowire array region from the rest of the conductive film and the deposition of metal contacts at pre-defined locations. Moreover, it may be necessary to deposit a micron-size heater near the region of interest in order to create a large enough temperature gradient over an extremely short distance for a detectable thermal voltage. Such efforts are currently underway as part of the collaboration with Prof. Pipe's group. Another ongoing endeavor involves the scanning tunneling microscopy (STM) and spectroscopy (STS) studies that investigate the local band structure and thermoelectric properties of these nanowires, currently taking place in Prof. Goldman's lab. In addition to these electric and thermoelectric characterizations, experiments involving magnetic and optical properties of these Sb_2Te_3 nanowire arrays can also be explored, due to their potential in spintronics and as polarization components as mentioned previously. These suggested experiments form a rich set of potential studies for future investigators interested in the fundamentals of nanowire formations.

References

[5.1] U. Kalsoom, S. Bashir, and N. Ali, "SEM, AFM, EDX and XRD analysis of laser ablated Ti in nonreactive and reactive ambient environments", *Surf. Coat. Technol.* **235**, 297 (2013)

[5.2] E. György, A. Pérez del Pino, P. Serra, J. L. Morenza, "Influence of the ambient gas in laser structuring of the titanium surface", *Surf. Coat. Technol.* **187**, 245 (2004)

[5.3] E. C. Landis, K. C. Phillips, E. Mazur, and C. M. Friend, "Formation of nanostructured TiO_2 by femtosecond laser irradiation of titanium in O_2", *J. Appl. Phys.* **112**, 063108 (2012)

[5.4] N. Ohtsu, K. Kodama, K. Kitagawa, and K. Wagatsuma, "X-ray photoelectron spectroscopic study on surface reaction on titanium by laser irradiation in nitrogen atmosphere", *Appl. Surf. Sci.* **255**, 7351 (2009)

[5.5] A. Y. Vorobyev and C. Guo, "Nanochemical effects in femtosecond laser ablation of metals", *Appl. Phys. Lett.* **102**, 074107 (2013)

[5.6] U. Kalsoom, S. Bashir, N. Ali, M. Akram, K. Mahmood, R. Ahmad, "Effect of ambient environment on excimer laser induced micro and nano-structuring of stainless steel", *Appl. Surf. Sci.* **261**, 101 (2012)

[5.7] T. Tomita, K. Kinoshita, S. Matsuo, and S. Hashimoto, "Effect of surface roughening on femtosecond laser-induced ripple structures", *Appl. Phys. Lett.* **90**, 153115 (2007)

[5.8] G. Obara, H. Shimizu, T. Enami, E. Mazur, M. Terakawa, and M. Obara, "Growth of high spatial frequency periodic ripple structures on SiC crystal surfaces irradiated with successive femtosecond laser pulses", *Opt. Express* **21**, 26323 (2013)

[5.9] A. I. Hochbaum, R. Chen, R. D. Delgado, W. Liang, E. C. Garnett, M. Najarian, A. Majumdar, and P. Yang, "Enhanced thermoelectric performance of rough silicon nanowires", *Nature* **451**, 163 (2008)

[5.10] Y. M. Zuev, J. S. Lee, C. Galloy, H. Park, and P. Kim, "Diameter dependence of the transport properties of antimony telluride nanowires", *Nano Lett.* **10**, 3037 (2010)

[5.11] C. Tannous, A. Ghaddar, and J. Gieraltowski, "Nanowire arrays, surface anisotropy, magnetoelastic effects and spintronics", *Appl. Phys. Lett.* **100**, 182401 (2012)

[5.12] J. Tang, C. Wang, M. Hung, X. Jiang, L. Chang, L. He, P. Liu, H. Yang, H. Tuan, L. Chen, and K. L. Wang, "Ferromagnetic germanide in Ge nanowire transistors for spintronics application", *ACS Nano* **6**, 5710 (2012)

[5.13] Y. Cui, Q. Wei, H. Park, and C. M. Lieber, "Nanowire nanosensors for highly sensitive and selective detection of biological and chemical species", *Science* **293**, 1289 (2001)

[5.14] F. Patolsky and C. M. Lieber, "Nanowire nanosensors", *Mater. Today* **8**, 20 (2005)

[5.15] X. Duan, Y. Huang, Y. Cui, J. Wang, and C. M. Lieber, "Indium phosphide nanowires as building blocks for nanoscale electronic and optoelectronic devices", *Nature* **409**, 66 (2001)

[5.16] M. H. Huang, S. Mao, H. Feick, H. Yan, Y. Wu, H. Kind, E. Weber, R. Russo, and P. Yang, "Room-temperature ultraviolet nanowire nanolasers", *Science* **292**, 1897 (2001)

[5.17] T. Ayvazian, W. E. van der Veer, W. Xing, W. Yan, and R. M. Penner, "Electroluminescent, polycrystalline cadmium selenide nanowire arrays", *ACS Nano* **7**, 9469 (2013)

[5.18] J. Yeon, Y. J. Lee, D. E. Yoo, K. J. Yoo, J. S. Kim, J. Lee, J. O. Lee, S. J. Choi, G. W. Yoon, D. W. Lee, G. S. Lee, H. C. Hwang, and J. B. Yoon, "High throughput ultralong (20 cm) nanowire fabrication using a wafer-scale nanograting template", *Nano Lett.* **13**, 3978 (2013)

[5.19] Y. Cui, L. J. Lauhon, M. S. Gudiksen, J. Wang, and C. M. Lieber, "Diameter-controlled synthesis of single-crystal silicon nanowires", *Appl. Phys. Lett.* **78**, 2214 (2001)

[5.20] G. Kim, M. Shtein, and K. P. Pipe, "Thermoelectric and bulk mobility measurements in pentacene thin films", *Appl. Phys. Lett.* **98**, 093303 (2011)

[5.21] G. Wang, L. Endicott, H. Chi, P. Lošťák, and C. Uher, "Tuning the temperature domain of phonon drag in thin films by the choice of substrate", *Phys. Rev. Lett.* **111**, 046803 (2013)